Sea ice and upper ocean variability in the Southern Ocean

Earle Wilson

A dissertation
submitted in partial fulfillment of the
requirements for the degree of

Doctor of Philosophy

University of Washington

2019

Reading Committee:

Stephen Riser, Chair

Eric A. D'Asaro

Kyle C. Armour

Program Authorized to Offer Degree:
School of Oceanography

University of Washington

Abstract

Sea ice and upper ocean variability in the Southern Ocean

Earle Wilson

Chair of the Supervisory Committee:
Professor Stephen Riser
Oceanography

This dissertation explores key physical mechanisms that control upper ocean and sea ice variability in the Southern Ocean. The first portion of this work presents an observational analysis of wintertime upper ocean stability and pycnocline heat availability in the Antarctic sea ice zone. This analysis reveals that the southern Weddell Sea region, which features a weak upper ocean stratification and relatively strong thermocline, is preconditioned for exceptionally high rates of winter ventilation. In other open-ocean regions, such as the northern Ross Sea, the stronger winter stratification greatly limits the efficiency with which heat may be extracted from the pycnocline. The coupling between winter ice growth and upper ocean ventilation is further explored using an idealized 1D sea ice-ocean model. This model is used to simulate winter ice growth in different regions under identical surface forcing. Consistent with the observational analysis, these simulations show that the unique thermohaline structure of the Weddell Sea, specifically that near Maud Rise, facilitates a strong negative feedback to winter sea ice growth. For this region, the entrainment of heat into the mixed layer can maintain a near-constant ice thickness over much of winter. However, these simulations also reveal that this quasi-equilibrium is attained when the pycnocline is thin and supports a large vertical temperature gradient. Further experimentation demonstrates that the surface stress imparted by a powerful storm may upset this balance and lead to substantial ice melt. In simulations initialized with profiles from more strongly stratified

regions, such as near the sea ice edge of the major polar gyres, the entrainment of heat into the mixed layer had weak impact on winter ice growth—even during periods of strong wind forcing. Thus, a key takeaway is that the thermodynamic coupling between winter sea ice growth and ocean ventilation has significant regional variability. This regionality must be considered when evaluating the response of the Antarctic ice-ocean system to future changes in ocean stratification and surface forcing.

In the final portion of this dissertation, focus is shifted to variations in Southern Ocean sea surface temperature (SST) and sea ice extent (SIE) on seasonal timescales. This work is motivated by the abrupt reversal of Southern Ocean SST and SIE trends that occurred in 2016 and 2017. The first half of this chapter examines the role of surface winds in the initiation of the anomalous sea ice retreat that occurred in late 2016. This is done via a simple regression analysis that quantifies the linear relationship between seasonal SIC anomalies and near-instantaneous local wind anomalies, using observations and reanalysis. With this empirical relationship, we demonstrate that surface wind anomalies can largely explain the SIC anomalies observed in the winter and spring of 2016. In the Weddell Sea, some of this preconditioning was associated with the winter polynyas that appeared that year. These events are linked to strong upwelling in the Weddell Sea and the passage of powerful winter storms. Lastly, we construct an updated seasonal mixed layer heat budget for the Southern Ocean, which is then used to explain the near-record Southern Ocean SSTs that occurred in the summer of 2016–2017. This analysis reveals that the warming maximum was the combined effect of enhanced air-sea heating, reduced northward Ekman transport, and shallower than normal mixed layer depths. From these results, we conclude that the 2016–2017 Southern Ocean SST and SIE anomalies were primarily caused by a serendipitous sequence of anomalous atmospheric and oceanic conditions. These anomalies coincided with an unusual synchronization of tropical and extratropical modes of climate variability.

TABLE OF CONTENTS

LIST OF FIGURES

ACKNOWLEDGMENTS

I extend my sincerest gratitude to my advisor Steve Riser for his guidance, encouragement, and mentorship throughout my time at UW. I also thank my other committee members, Eric D'Asaro, Kyle Armour, Mark Warner, Cecilia Bitz, and Peter Rhines, for providing constructive feedback and keeping me on track to graduate in a timely manner. I thank all my current and former "lab" mates, Jesse, Tyler, Ethan, Rosalind, Katy, and Jade, for thoughtful discussions, words of encouragement, and delicious pastries. I express deep appreciation for my cohort for being great colleagues and even better friends—special thanks to Anna and Sarah being there with me till the very end and keeping me sane during the writing of this dissertation. Similarly, I thank the entire UW oceanography community for making my time in graduate school an overall fun and fulfilling experience. Lastly, I thank my family for cheering me on every step of the way.

DEDICATION

To my parents, Earle and Terese, for their steadfast love and support throughout my life and for inspiring me to pursue my dreams, even when those dreams took me thousands of miles away from home.

Chapter 1
INTRODUCTION

The Southern Ocean has far-reaching impacts on the global climate. The importance of this region is largely due to its unique geographical configuration and high latitude location. The former permits the existence of the Antarctic Circumpolar Current (ACC)—a powerful eastward flow that encircles Antarctica and separates the relatively cold Antarctic waters from the much warmer subtropical ocean (Rintoul et al., 2001). By linking the Atlantic, Pacific, and Indian Oceans, the ACC mediates the inter-basin exchange of ocean properties, such as heat, carbon, and dissolved nutrients. Additionally, the mixing that occurs within the current facilitates the synthesis of new water masses, which are subsequently exported to lower latitudes. Accompanying this horizontal circulation is a much weaker but arguably more important overturning circulation. Under the influence of Earth's rotation, westerly winds drive the near-surface layers of the Southern Ocean northwards, away from Antarctica. This surface divergence is simultaneously compensated by an upward flow that extends deep into the ocean interior. The upwelling that occurs within the Southern Ocean counterbalances the formation of deep water in the North Atlantic and thus closes the upper cell of the global overturning circulation of the ocean (Marshall and Speer, 2012). The Southern Ocean is also the source of Antarctic Bottom Water (AABW)—the water mass that covers most of the abyssal ocean (Johnson, 2008). AABW formation occurs along the Antarctic coastline, in regions that feature intense sea ice production. The dense, salty brine that results from this ice formation process triggers deep mixing that leads to modification of abyssal waters (Gill, 1973). Such deep-reaching vertical processes are limited to a small number of locations in the global ocean. Thus, by supporting the upwelling of deep water and the formation of bottom water, the Southern Ocean plays a critical role in the exchange

of heat and carbon between the atmosphere and the ocean interior. The significance of these interactions is difficult to overstate. As anthropogenic CO_2 emissions continue to rise, the overturning circulation of the Southern Ocean will modulate the rate at which the entire climate system warms. The manner in which this will occur will depend on a myriad of interconnected physical and biogeochemical process, most of which are not well-understood.

Despite its profound significance, the Southern Ocean has been one of the least-sampled regions of the world ocean. This in large part due to the region's remote location and harsh climate, which together create a daunting challenge for sustained in situ observations. Because of this, much of our current understanding of the Southern Ocean has been inferred from a limited number of ship-based measurements. Though immensely valuable, these data were mainly collected during summer months, in ice free regions, along narrow transects (Roemmich and Gilson, 2009). Thus, historical shipboard data only provide a tiny glimpse of the variability that exists within the Southern Ocean. However, since the early 2000s, two advances in observational oceanography have drastically altered the way we study the region. The first is the development of Argo profiling floats that can safely sample under sea ice, for months on end, without surfacing. The second is the proliferation of instrumented marine mammals, in particular elephant seals, which record profiles of temperature and salinity as they forage for food. Together, these "ice-enabled" Argo floats and instrumented seals have supplanted traditional ship-based measurements as the primary source of in situ ocean data for the region. Though there are still gaps in the spatial coverage, these platforms now provide year-round observations of both the ice-free and seasonally ice-covered Southern Ocean.

This dissertation explores upper ocean and sea ice variability in the Southern Ocean through the lens of these modern oceanographic observations. The first two chapters of this thesis are dedicated to the most poorly observed region of the Southern Ocean: the winter sea ice zone. Specifically, these chapters investigate the thermodynamic coupling between winter sea ice growth and deep ocean ventilation, a process that modulates the thickness of winter sea ice and the transport of deep ocean heat towards the Antarctic

shelf. Exploiting recently collected under-ice ocean data, we are able to contrast the weakly stratified Weddell Sea region, which features strong suppression of winter sea ice growth, with the strongly stratified Ross Sea region that features opposite conditions. Since past studies of this process have focused primarily on the Weddell Sea, these results present a broader and more nuanced understanding of ice-ocean feedbacks in around Antarctica. The final chapter of this dissertation examines recent trends in surface temperatures and sea ice areal extent across the Southern Ocean. Of key interest are the abrupt changes that began in late 2016, which involved record surface warming and loss in sea ice cover across the entire Southern Ocean. As in the previous chapters, this analysis is anchored by recent in situ ocean observations. These observations are further supplemented by satellite-based sea ice concentration data and atmospheric reanalysis. Using these data, we investigate the proximate causes for these extreme anomalies and assess the relative contributions of long-term climate change and shorter term climate variability. In pursuit of this end, this chapter also presents an updated seasonal mixed layer heat budget for the Southern Ocean—extending the mixed layer heat budget analysis presented by Dong et al. (2007).

The overarching goal of this dissertation is to expand and refine our understanding of the Southern Ocean ice-ocean system. The hope is that the results presented herein will provide a road map for future research endeavors that will further unravel the mysteries of the Southern Ocean.

Chapter 2

OBSERVATIONS OF WINTERTIME UPPER OCEAN STABILITY AND HEAT AVAILABILITY IN SEA ICE-COVERED SOUTHERN OCEAN

(Contents of this chapter have been previously published in Wilson, E. A., S. C. Riser, A. Wong and E. C. Campbell (2019), Winter upper ocean stability and ice-ocean feedbacks in the sea ice-covered Southern Ocean, Journal of Physical Oceanography, 49, 1099–1117, doi: 10.1175/JPO-D-18-0184.1.)

2.1 Introduction

In the sea ice-covered Southern Ocean, a relatively thin halocline separates the cold winter mixed layer from the significantly warmer ocean interior (Gordon and Huber, 1984). Over the course of winter, this halocline is gradually eroded by convective instabilities, triggered by the brine released from sea ice growth (Gordon et al., 1984). In some regions, such as the weakly stratified Weddell Sea, the halocline is typically eroded to the point where a relatively small addition of brine would completely eliminate the main pycnocline and permit uninhibited convection into the ocean interior (Martinson and Iannuzzi, 1998). However, the pycnocline in these regions generally remains intact throughout winter and limits convection to the upper 200 m of the water column (Gordon and Huber, 1990; Pellichero et al., 2017). The somewhat surprising resilience of this weak winter stratification is largely due to the upper ocean's negative feedback to ice growth (Martinson, 1990). As the mixed layer deepens, the entrained heat provides a basal heat flux to the sea ice that suppresses further ice growth and, in some cases, causes melt that restratifies the upper ocean (McPhee et al., 1999). Thus, the winter temperature profile, despite featuring a cold-over-warm water configuration, helps

to maintain the stability of the water column by limiting the destabilizing effect of sea ice growth. On the rare occasions that sustained deep convection does occur, the ventilated heat creates vast areas of open water within the sea ice zone. The most dramatic examples of such an event are the Weddell Sea polynyas that occurred during the winters of 1974–1976. At their peak, these polynyas occupied a large portion of the Weddell Sea and featured convection down to at least 4000 m (Gordon, 1978). Since then, no winter polynya of a similar magnitude or duration has occurred in the Southern Ocean.

The main source of deep ocean heat in this region is Circumpolar Deep Water (CDW) (Foster and Carmack, 1976). This water mass is progressively cooled as it is upwelled and circulated within the polar gyres of the Southern Ocean (Fahrbach et al., 1994). The modified CDW that results from this ventilation is a major source of heat for the shelf waters of Antarctica and, by extension, the marine terminating glaciers of the Antarctic Ice Sheet (Jacobs et al., 1985; Pritchard et al., 2012). This water mass is also a key end-member in the formation of Antarctic Bottom Water (AABW), which is exported to most of the global abyssal ocean (Gill, 1973; Johnson, 2008). Thus, the wintertime ventilation of deep ocean in the sea ice zone directly modulates the flow of heat to the Antarctic continental margin and helps set the properties of AABW.

Though the ventilation of heat in the Antarctic sea ice zone has been the focus of many studies, our understanding of its spatial and temporal variability has been limited by the historical lack of in situ winter ocean data. Prior to the early 2000s, winter ocean data were mainly collected during sporadic research cruises conducted on icebreakers. Since then, two recent advances in observational oceanography have led to a dramatic increase in wintertime under-ice ocean data. The first is the introduction of Argo floats equipped with ice-avoidance algorithms that allow them to safely profile in the presence of sea ice (Klatt et al., 2007; Wong and Riser, 2011). The second is the advent of animal-borne sensor programs that have equipped hundreds of seals with satellite-linked conductivity-temperature-depth (CTD) sensors (Roquet et al., 2013). Together, under-ice Argo floats and instrumented seals have provided unprecedented year-round coverage of the oceans around Antarctica.

The primary goal of this study is to better understand the relationship between wintertime upper ocean stability, deep ocean ventilation, and sea ice growth in the Southern Ocean. Our analysis borrows heavily from the conceptual framework laid out by Martinson (1990) and Martinson and Iannuzzi (1998). In particular, we use modified versions of their bulk stability metrics to diagnose the stability of the upper ocean stability and the availability of deep ocean heat in the winter sea ice zone. By using more recent winter CTD data, we are able to expand on these previous studies, which have focused on the Weddell region. This work is complementary to the recent mixed layer analysis presented by Pellichero et al. (2017), who use a similar set of CTD observations. While they focus on the seasonal evolution of mixed layer properties in the Southern Ocean, we focus exclusively on the winter season and investigate the thermodynamic coupling between ice growth and ocean ventilation in more detail.

In the next section, we describe our data and analysis techniques. This is followed by a presentation of our observational analysis and a discussion of our key findings.

2.2 Data acquisition and processing

2.2.1 CTD profiles

The primary observations used in this study are CTD profiles collected by Argo floats, instrumented seals, and ship-based casts. Argo float data were acquired from the March 2018 snapshot of the Argo Global Data Assembly Centre (GDAC) database (Argo, 2018). We used the "adjusted" CTD profiles, which have been modified to eliminate known biases, and retained profiles for which each measurement was flagged as data of "good" quality (QC-flag = 1). The seal-based data were obtained from the November 2017 release of the Marine Mammal Exploring the Oceans Pole-to-Pole (MEOP) CTD database (Roquet et al., 2017). These data were provided in the format as the GDAC database. As before, we retained adjusted profiles that passed all quality control checks (QC-flag = 1). The ship-based data were acquired from the NOAA World Ocean Database (`https://www.nodc.noaa.gov/OC5/`

SELECT/dbsearch/dbsearch.html), which was accessed on February 1, 2018. We selected profiles collected by high resolution CTD casts and ocean station bottle data, saving only the profiles flagged as good (QC-flag = 0).

Winter profiles from ships and instrumented seals are transmitted with relatively precise geographical coordinates. However, since Argo floats generally do not surface in the presence of sea ice, their exact coordinates are unknown during the winter (Wong and Riser, 2011). The under-ice locations of these profiles are estimated using linear interpolation. This captures the mean trajectory of the float over the course of winter, but neglects any deviations caused by eddies or topographical effects. We assume that these positional errors are smaller than the basin-wide scales that are of interest in this study.

To ensure that each profile accurately resolves the key features of the upper ocean, specifically the mixed layer and the pycnocline, we filtered for profiles that extend deeper than 300 m and have more than 5 data points above that depth level. Additionally, we only retained profiles that have data points above 25 m, which ensures that the properties of the mixed layer are captured. Applying the first filter mainly affects the seal-based data, which have the coarsest vertical resolution. These profiles are transmitted via satellite in a compressed form that contains only 10–25 data points (Roquet et al., 2014). Since seals regularly dive beyond 500 m, the apparent vertical resolution of these profiles is on the order of tens of meters. However, the transmitted data points are chosen using an algorithm that identifies the major inflection points of the CTD profile (Boehme et al., 2009). We therefore make the assumption that the seal-based profiles, though relatively coarse, still capture the key features of the upper ocean. The chosen profiles, from all sources, were then linearly interpolated to a common vertical coordinate that has a resolution of 0.5 m in the upper 500 m and progressively coarser spacing at deeper levels. Missing near-surface values were filled using nearest neighbor extrapolation.

For the winter season, which is defined here as June through September, Argo floats and instrumented seals are the largest contributors of CTD data (Figure 2.1). Almost all of these data were collected within the past 15 years (Figure 2.2). CTD profiles from Argo

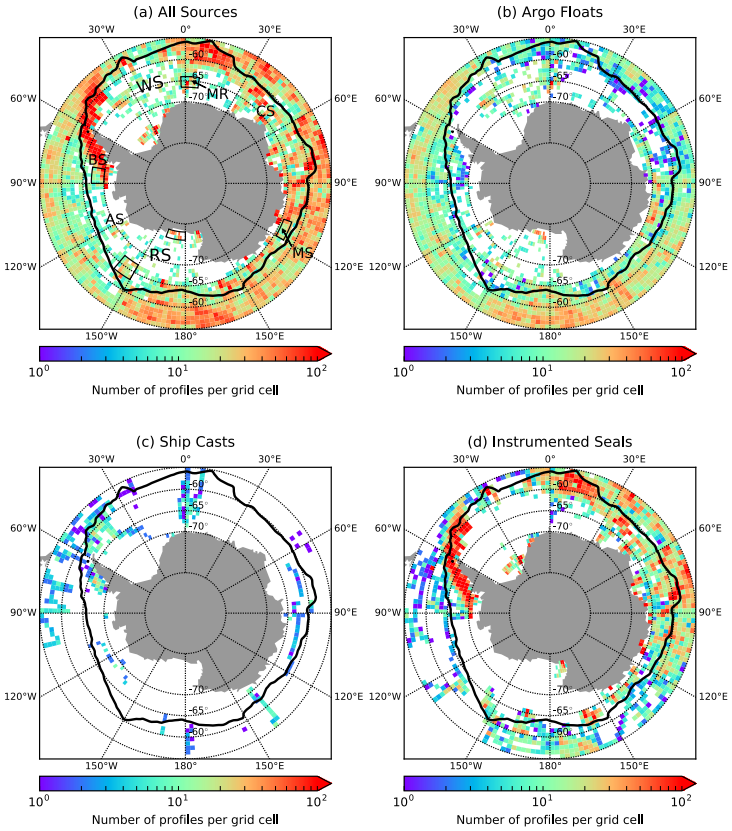

Figure 2.1: The spatial distribution of winter CTD profiles binned on a 2° longitude by 1° latitude grid. (a) Total number of profiles in each grid box. (b-d) Total number of profiles in each grid box from Argo floats, ship casts, and instrumented seals, respectively. Areas of interest are annotated in (a): Weddell Sea (WS), Ross Sea (RS), Maud Rise (MR), Bellingshausen Sea (BS), Amundsen Sea (AS), Cosmonauts Sea (CS), and Mawson Sea (MS). The boxes outline five subregions that are referenced in Figures 2.3, 2.4, 2.8, and 3.2. In the Ross Sea region, the northern and southern boxes outline the northern Ross Sea and eastern Ross Shelf subregions, respectively.

floats are broadly distributed across the sea ice zone. Profiles from seals are mostly found in the eastern Atlantic and Indian Ocean sectors, and along the western coast of the Antarctic Peninsula. The relatively few ship-based profiles are mainly from the Weddell region and near the Antarctic Peninsula. When composited in time, these three sources of data provide near-complete coverage of the sea ice zone during the winter season.

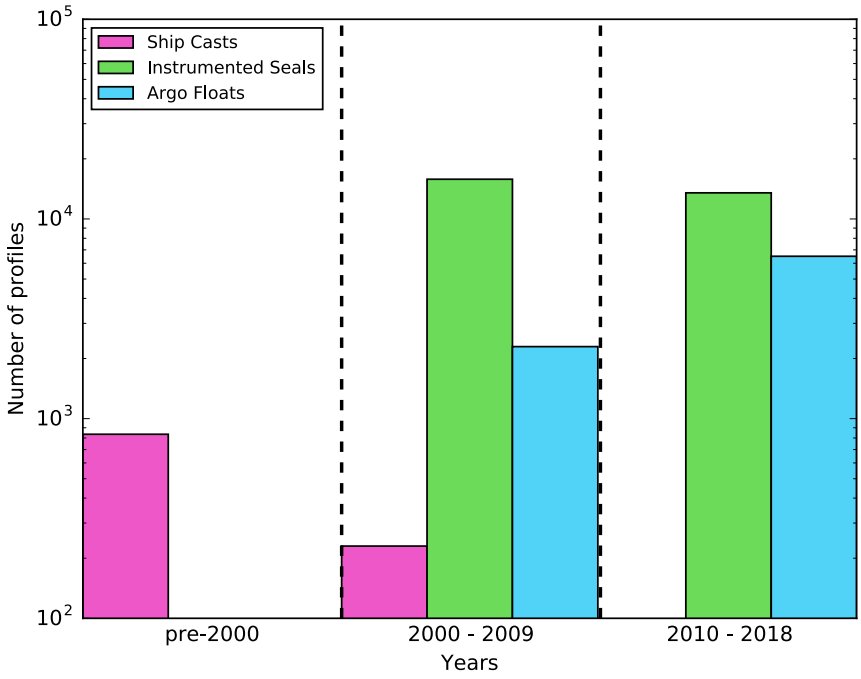

Figure 2.2: Bar graph showing the temporal distribution of June–September CTD profiles collected within the winter sea ice zone. Profiles are separated by source (Argo floats, ship casts, and instrumented seals) and time period (pre-2000, 2000-2009, and 2010-2018). The winter sea ice zone is defined by a solid dark line in Figure 2.1.

Unless otherwise stated, all calculations (for example, computing the mixed layer depth) are first applied to individual profiles and then spatially averaged over a given region. Spatial averages were computed for large regional domains of key interest and more localized 2° longitude by 1° latitude grid boxes. No form of horizontal interpolation or smoothing was applied to these data.

2.2.2 Sea ice concentration

To define the winter sea ice zone, we used version 3 of the NOAA/NSIDC Climate Data Record (CDR) sea ice concentration product (Peng et al., 2013; Meier et al., 2017). With this data, which is provided on a 25 km by 25 km spatial grid as monthly averages from

August 1987 to February 2017, we constructed a climatology and defined the winter sea ice zone as the area within which the mean June–September sea ice concentration is greater than 15%.

2.3 Quantifying upper ocean stability

In his seminal work, Martinson (1990) (hereafter M90) introduced the salt deficit (SD) and thermal barrier (TB) diagnostics as measures of upper ocean stability. SD represents the integrated freshwater anomaly of the mixed layer and the halocline (see Figure 2.3 for example winter profiles) and is defined as the sea ice growth that would cause the mixed layer to entrain the entire halocline. TB is the integrated heat content of the halocline and thus quantifies the halocline's capacity to provide a negative feedback to ice growth. Martinson and Iannuzzi (1998) (hereafter M98) used all winter ship-based CTD data that were available at the time to quantify these metrics in the Weddell region. This analysis showed that, in most cases, roughly 1 m of additional winter sea ice growth would be enough to eliminate the local halocline and permit thermally-driven convection in the ocean interior.

Here, we introduce slightly modified versions of SD and TB that account for the destabilizing effect of the winter temperature profile. These metrics provide an upper bound on the sea ice growth needed to erode the *pycnocline* rather than the halocline. To obtain these metrics, we exploit the fact that winter mixed layer temperature (MLT) in the sea ice zone generally stays near the freezing point of seawater T_f (Gordon and Huber, 1990). Mixed layer salinity (MLS), on the other hand, tends to increase throughout winter. If we take the winter MLT to be exactly T_f, we can find a critical MLS, S_c, that would allow the density of the mixed layer to be equal to the density at some depth below the pycnocline. That is, we can determine S_c such that

$$\sigma_{ML}(S_c,\, T_f,\, z = 0) = \sigma_d(S_d,\, T_d,\, z_d), \tag{2.1}$$

where σ is potential density referenced to the surface and subscript d indicates deep ocean values, below the pycnocline. S_c can be determined numerically using a function for potential

density, such as that provided in the Thermodynamic Equation of Seawater–2010 (TEOS-10) toolbox (McDougall and Barker, 2011). In the northern Ross Sea and Maud Rise profiles, σ varies very little below 300 m (Figure 2.3). This is true across the entire winter sea ice zone. This means the solution to (2.1) is insensitive to the choice of z_d provided it is below this depth. Since most profiles from instrumented seals have a maximum depth of 500 m, we use $z_d = 500$ m as our reference deep ocean level.

The equality expressed in (2.1) is attained when the freshwater anomaly above the depth where $S(z) = S_c$ is removed from the upper ocean. Taking this critical depth to be z_c, we define the pycnocline salt deficit SD* as

$$SD^* = \frac{1}{\Delta S_i} \int_0^{z_c} [S(z_c) - S(z)]\, dz. \tag{2.2}$$

where $S(z)$ is the upper ocean salinity profile, and $\Delta\, S_i$ is the salinity difference between the ocean surface and sea ice. Following M98, we take $\Delta\, S_i$ to be 30 PSU, assuming a typical sea ice salinity and MLS of 4 PSU and 34 PSU, respectively. SD* has units of ice thickness (i.e. meters of required ice growth) and is analogous to the halocline SD metric introduced by M90. The corresponing pycnocline thermal barrier TB* is defined as the total heat content between the base of the mixed layer and the depth z_c. This is given by

$$TB^* = \rho_w\, c_w \int_0^{z_c} [T(z) - MLT]\, dz, \tag{2.3}$$

where ρ_w is the density of seawater, c_w is the specific heat capacity of seawater, and $T(z)$ is the upper ocean temperature profile. Unlike M98, we express TB* in units of heat (J m^{-2}) rather than meters of potential ice melt. Lastly, since z_c approximately coincides with the base of the pycnocline (Figure 2.3), we compute the thickness of the pycnocline, L_p, as

$$L_p = |z_c - MLD|, \tag{2.4}$$

where MLD refers to the mixed layer depth. Since the base of the pycnocline is not always well-defined and the transition into the ocean interior can be relatively smooth, we treat L_p as a rough vertical length scale for the pycnocline.

To arrive at (2.2) and (2.3), we neglect many non-ice-related processes that could alter upper ocean stratification over the course of winter. Following M98, we assume that changes in MLS due to precipitation are small compared to those due sea ice growth. This is a reasonable assumption for much of the winter sea ice zone, where the open-water fraction is generally less than 5% in the winter. The remaining processes that can modify upper ocean salinity are horizontal stirring and vertical mixing across the base of the mixed layer. On basin-wide scales, the MLS tendency due to horizontal advection is small relative to the MLS changes associated with vertical mixing and ice-ocean freshwater fluxes (Pellichero et al., 2017). This may not be the case on smaller scales but, given the coarse spatial resolution of our CTD data, we do not attempt to quantify the effects of small-scale horizontal mixing. Vertical mixing across the base of the mixed layer will tend to increase MLS. This vertical exchange may result from shear-induced mixing from wind and ice-ocean stresses, double diffusion, thermobaric instabilities, and internal wave breaking (Muench et al., 1990; McPhee and Martinson, 1994; Robertson et al., 1995; Akitomo, 1999). We do not attempt to quantify the impact of these vertical processes, which are poorly constrained across the winter sea ice zone. Nevertheless, observations suggest that sea ice growth is the primary driver of wintertime MLS variability underneath sea ice (Charrassin et al., 2008; Wong and Riser, 2011). We therefore focus on salt fluxes from brine rejection and treat SD^* as an upper bound on the ice growth needed to permit thermally driven convection into the ocean interior. Furthermore, heat fluxes from the deep ocean may partially replenish the heat content of the pycnocline over the course of winter. TB^* is therefore a lower bound on the amount of heat that could be ventilated from the pycnocline.

As an example, we compute SD^* and TB^* for representative early winter profiles from the northern Ross Sea and Maud Rise regions (Figure 2.3). These regions represent opposite extremes in off-shelf, upper ocean stratification in the winter sea ice zone. Assuming a deep ocean reference level of 500 m, we find that $SD^* = 2.7$ m and $TB^* = 0.4$ GJ/m^2 for the northern Ross Sea. This means 2.7 m of additional winter sea ice growth would weaken the haline stratification to the point where surface cooling, on its own, could drive convection

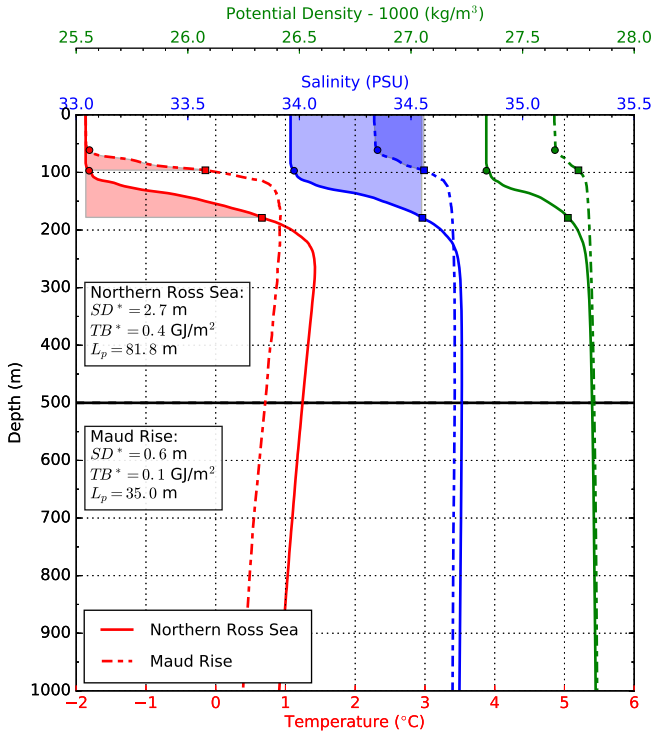

Figure 2.3: Example early winter (June) profiles of temperature (red) and salinity (blue) from Maud Rise (solid lines) and the northern Ross Sea (broken lines). The blue and red shadings show the area integrals used to compute the pycnocline salt deficit (SD*) and thermal barrier (TD*), respectively. Circle markers indicate the MLD, which is defined using a 0.02 kg/m^3 density threshold. Square markers indicate z_c, the depth where salinity is equal to the critical MLS that would allow the potential density of the ML to be equal to that at 500 m (see equation 2.1 and the ensuing discussion). L_p is pycnocline thickness, which we define as the difference between MLD and z_c.

down to 500 m. However, the production of 2.7 m of additional sea ice would ventilate (at minimum) 0.4 GJ/m^2 of heat, which could melt approximately 1.3 meters of sea ice. Over the more weakly stratified Maud Rise, these values are much lower, with SD* = 0.6 m and TB* = 0.1 GJ/m^2.

Going a step further, if we divide TB* by SD* we obtain a measure for the *total* availability of heat in the pycnocline:

$$\gamma_p = \frac{TB^*}{SD^*}. \tag{2.5}$$

The quantity γ_p gives the average heat released per unit ice growth, in the event the entire pycnocline is entrained into the mixed layer. However, in most regions, only a fraction of the pycnocline is eroded each winter. More importantly, the efficiency of heat ventilation (i.e. the heat released per unit ice growth) increases with the depth of entrainment. To demonstrate this, we introduce slightly more general definitions of the salt deficit and thermal barrier metrics that are functions of entrainment depth:

$$\eta(z') = \frac{1}{\Delta S_i} \int_0^{z'} [S(z') - S(z)] \, dz, \tag{2.6}$$

$$\nu(z') = \rho_w \, c_w \int_0^{z'} [T(z) - MLT] \, dz. \tag{2.7}$$

In the above equations, η is the sea ice growth needed to deepen the mixed layer to some arbitrary depth z' while ν is the amount of heat that would be ventilated if the mixed layer deepens to that level. When $z' = z_c$, η and ν are equivalent to SD* and TB*, respectively. Given the geometry of upper ocean winter profiles of temperature and salinity, we find that $\frac{\mathrm{d}\nu}{\mathrm{d}z'} > \frac{\mathrm{d}\eta}{\mathrm{d}z'}$. This is because η represents the integrated salinity anomaly of the mixed layer and some fraction of the pycnocline, while ν depends only on the heat stored in the pycnocline (Figure 2.3). We note that below the pycnocline, $\frac{\mathrm{d}\eta}{\mathrm{d}z'}$ approaches zero while $\frac{\mathrm{d}\nu}{\mathrm{d}z'}$ tends toward some nonzero finite value. Furthermore, the quantity

$$\gamma(z') = \frac{\nu(z')}{\eta(z')}, \tag{2.8}$$

provides a depth-dependent metric that estimates the efficiency with which incremental sea ice growth can ventilate heat from the pycnocline.

2.4 Upper ocean properties in the winter sea ice zone

Between June and September, the mixed layer in off-shelf regions of the sea ice zone has direct access to the main thermocline (Figure 2.4). Here, MLD is defined as the depth where potential density is 0.02 kg m^{-3} greater than that at the surface. This relatively stringent density criterion is motivated by the need to accurately resolve the base of the winter mixed

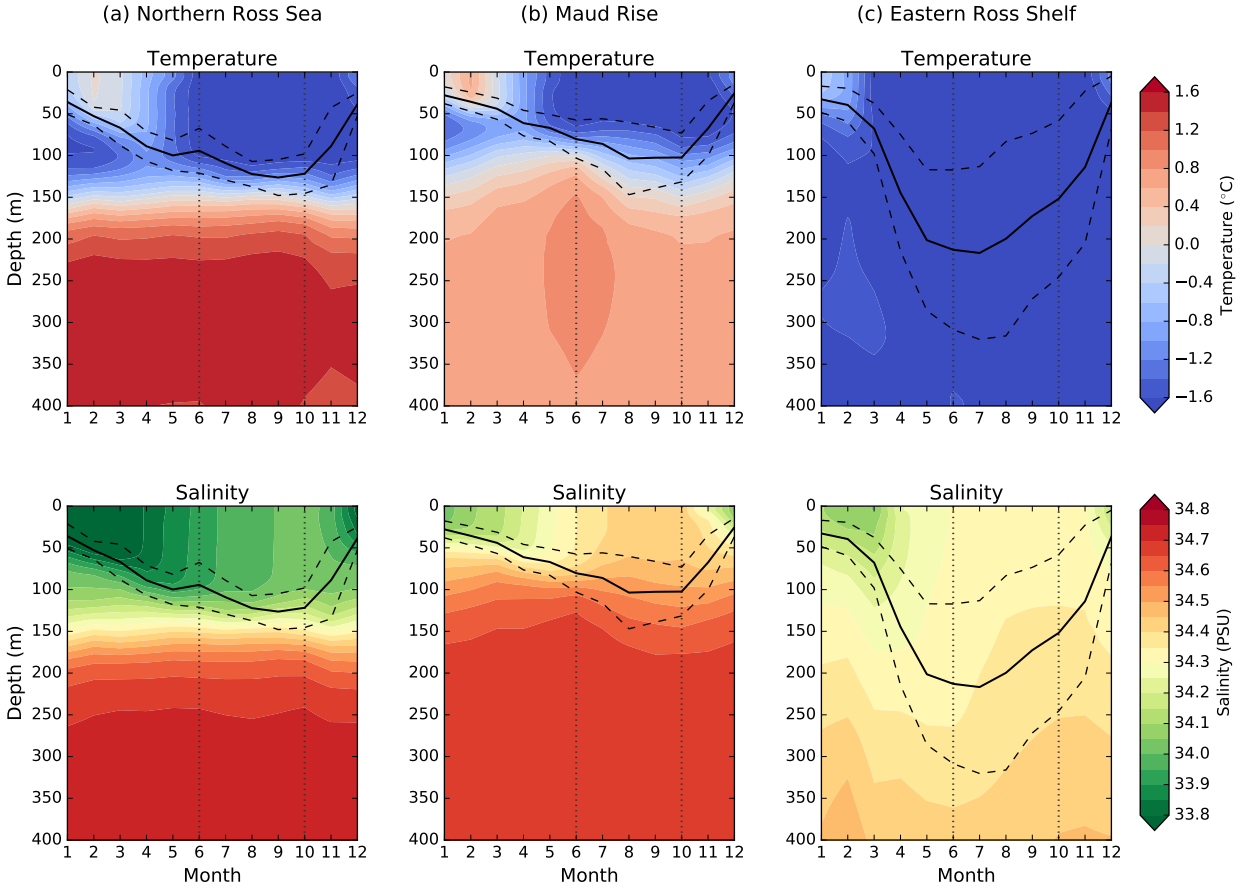

Figure 2.4: Monthly mean upper ocean temperature and salinity for the northern Ross Sea, Maud Rise, and the eastern Ross Shelf (see Figure 2.1 for region boundaries). The solid black lines represent the monthly mean MLD, which is defined as the depth where potential density is 0.02 kg m^{-3} greater than that at the surface. The vertical distance between the solid and dashed lines represent one standard deviation of the monthly MLD for each region. The dotted vertical lines demarcate the winter season, which we define as June through September.

layer in weakly stratified regions, such as near Maud Rise. After September, the mixed layer begins to shoal as it transitions back to its summer state. This seasonality motivates our choice to limit the winter season to June through September. Along the continental shelf, the water column typically lacks a well-defined thermocline and is usually uniformly near its freezing point during the winter (Figure 2.4c). For this reason, we focus on off-shelf regions,

where there is a distinct reservoir of deep ocean heat that can potentially modulate sea ice growth.

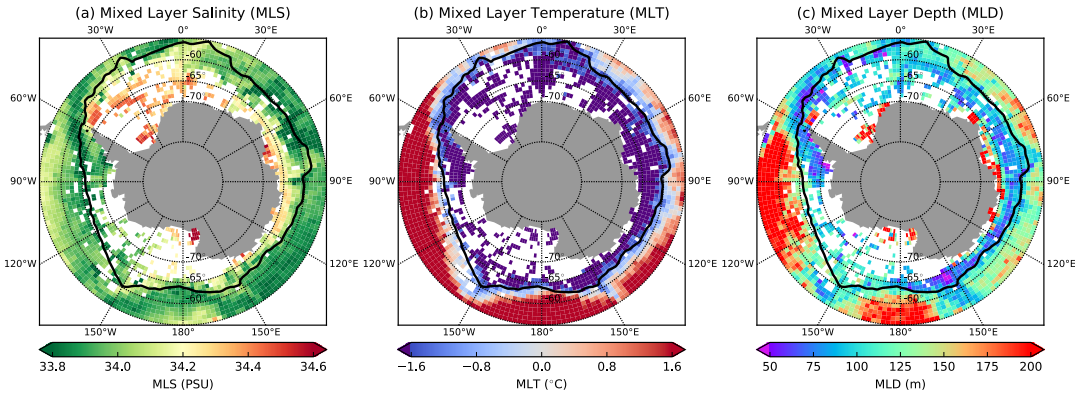

Figure 2.5: Properties of the winter mixed layer south of 55°S: (a) salinity, (b) temperature and (c) depth. The solid black line represents the mean winter sea ice edge.

Winter MLS in the Atlantic sector, the region east of the Antarctic Peninsula that roughly extends from 60°W to 30°E, is 0.3–0.4 PSU higher than in the Pacific sector, west of the Peninsula (Figure 2.5a). MLS in the Indian sector, along East Antarctica, is similar to that within the Atlantic sector, but has a stronger meridional gradient. This salinity gradient reflects the well-documented coastal production and northward export of sea ice around Antarctica (Drucker et al., 2011; Haumann et al., 2016). MLT is uniformly near the freezing point within the sea ice zone, but is several degrees warmer just beyond the ice edge. MLD varies between 75–125 m across off-shelf regions, but is significantly deeper along the continental shelf. These results are consistent with the mixed layer analysis presented by Pellichero et al. (2017).

We quantify the strength of the halocline as the difference between the subsurface salinity maximum, S_{max}, and MLS. The spatial pattern of halocline strength mirrors that of MLS within the sea ice zone (Figure 2.6a). In the Atlantic sector, the difference between S_{max} and MLS is generally less than 0.5 PSU. In contrast, this salinity difference is generally greater than 0.6 PSU in the Pacific sector. The spatial pattern of $T_{\max}$ is similar to that of

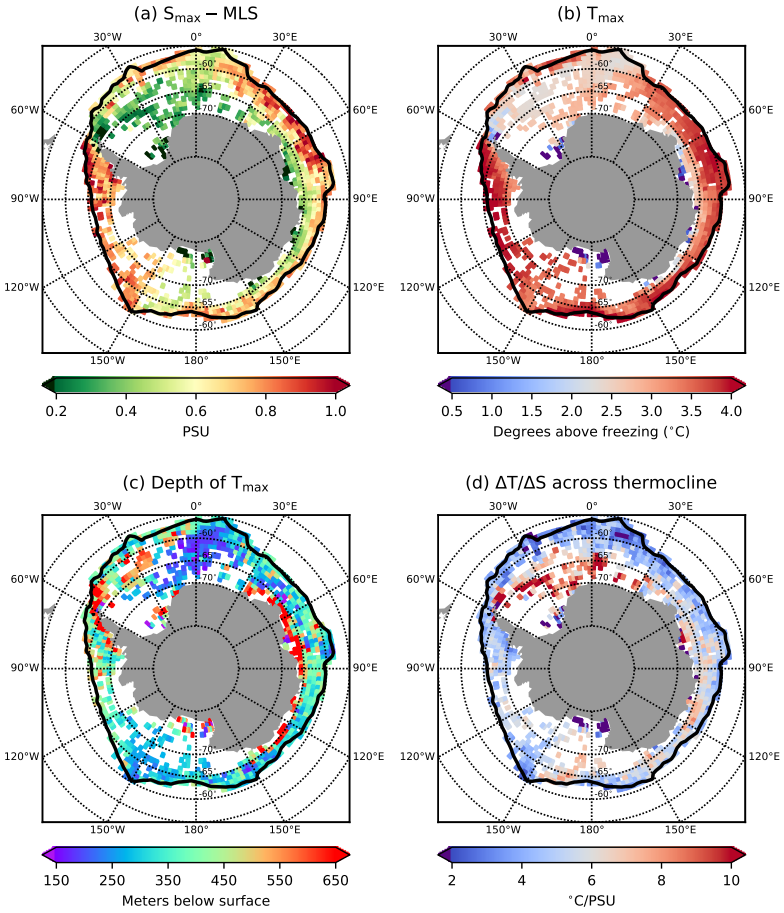

Figure 2.6: Maps showing subsurface ocean properties within the winter sea ice zone: (a) difference between MLS and the subsurface salinity maximum S_{max}, (b) subsurface temperature maximum $T_{\max}$, given in units of degrees above freezing, (c) depth of $T_{\max}$, and (d) the ratio of thermocline strength (ΔT) to halocline strength (ΔS) between the base of the mixed layer and $T_{\max}$. The solid black line represents the mean winter sea ice edge.

halocline strength, but with notably weaker contrasts (Figure 2.6b). In the Atlantic sector, near the Prime Meridian, the depth of T_{max} is generally shallower than 250 m (Figure 2.6c). In extreme cases, $T_{\max}$ lies just tens of meters below the winter mixed layer. These findings are consistent with previous studies that have mapped T_{max} across the Weddell region (e.g. Reeve et al., 2015). In other regions of the sea ice zone, T_{max} is generally deeper than 250 m.

Finally, we compare the temperature difference, ΔT, across the thermocline (i.e. between the base of the mixed layer and the depth of T_{max}) with the salinity difference, ΔS, across that layer. This highlights the southern Weddell as the region where the thermocline is strongest relative to the halocline (Figure 2.6d). In this region, $\Delta T/\Delta S$ across the thermocline is generally between 8–10 °C/PSU. Slightly lower values of $\Delta T/\Delta S$ are observed along the shelf break of East Antarctica and in the Ross Sea. $\Delta T/\Delta S$ is smallest in the eastern Pacific sector, where it mostly ranges between 4–6 °C/PSU.

In summary, upper ocean stratification is exceptionally weak within the Atlantic sector and along the continental shelf. The off-shelf region within the Atlantic sector is particularly interesting because it features a weak halocline and a relatively shallow reservoir of deep ocean heat. This suggests that this region is preconditioned for the highest rates of wintertime heat ventilation.

2.5 Winter upper ocean stability and heat availability

The regional pattern of SD* (defined here using a reference deep ocean level of 500 m) is similar to that of MLS and halocline strength (Figure 2.7a). In the Pacific sector, between 60°W and 180°W, SD* is generally greater than 2 m. This means the pycnocline in this region can support more than 2 m of additional winter ice growth before being completely eroded. In the Ross Sea and along East Antarctica, SD* is slightly lower and varies between 1–2 m of additional winter sea ice growth. As expected, SD* is relatively low across the interior of the Weddell, where it is generally less than 1.5 m. In particular, SD* is less than 0.5 m in the vicinity of Maud Rise. However, SD* exceeds 2 m along the winter ice edge of the Atlantic sector. The spatial pattern of SD* in the Atlantic sector closely resembles that of SD, as presented by M98.

Except for areas with perennial sea ice, ice thickness in the late winter and early spring typically ranges between 0.4–0.8 m in the Southern Ocean (Worby et al., 2008; Kurtz and Markus, 2012). As will be discussed later, this observed range of ice thickness is in part due to the ventilation of heat from the thermocline. Outside the Weddell region, offshore

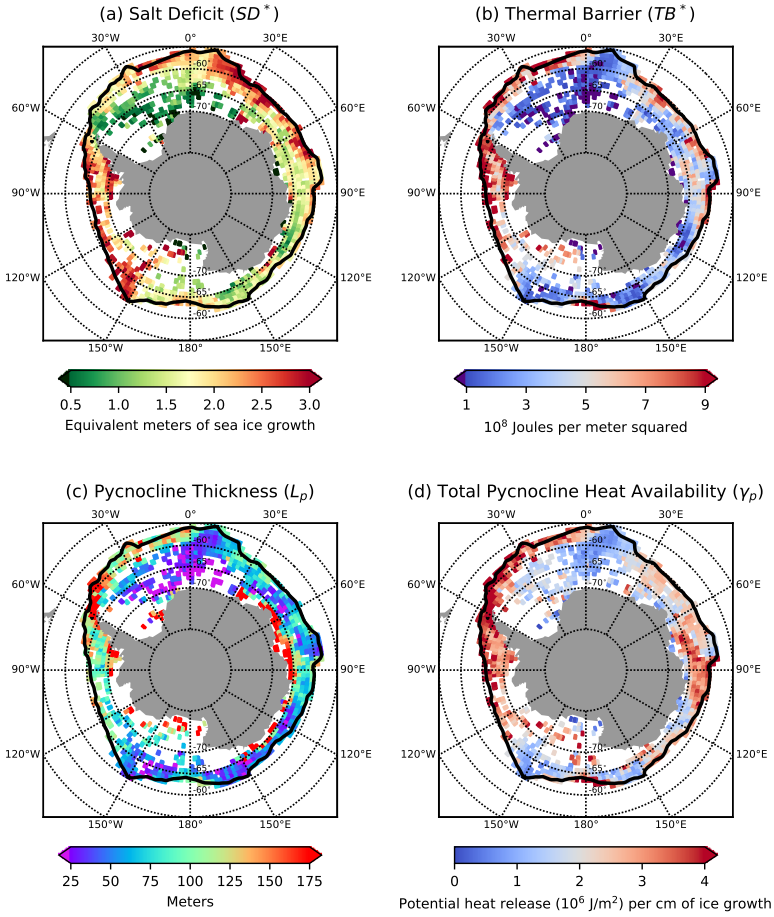

Figure 2.7: Maps showing winter upper ocean stability and heat availability within the winter sea ice zone: (a) pycnocline salt deficit SD*, (b) thermal barrier TB*, (c) pycnocline thickness L_p, and (d) total pycnocline heat availability $\gamma_p = TB^*/SD^*$. The solid black line represents the mean winter sea ice edge.

values of SD* far exceed the amount of in situ ice growth that normally occurs in a single year. Thus, we can conclude that full pycnocline erosion is highly unlikely to occur across most of the winter sea ice zone. However, in the Weddell region where SD* is often less than the total winter ice growth, it is conceivable that variations in the annual surface freshwater budget could leave the region susceptible to full pycnocline erosion. This also suggests that the ventilation of sub-mixed-layer heat in this region, which limits ice growth, plays a crucial role in preventing the full erosion of the pycnocline.

Total pycnocline heat content, as quantified by TB*, is relatively large in the eastern Pacific sector (Figure 2.7b). In the Bellingshausen Sea, growing an amount of sea ice equivalent to the local value of SD* would ventilate roughly 1 GJ/m^2 (10^9 joules per meter squared), which would be sufficient to melt approximately 3 m of ice. TB* is much smaller across the interior of the ice-covered Atlantic sector, where it is generally less than 0.3 GJ/m^2. In the Ross Sea and along East Antarctica, TB* broadly varies between 0.1–0.7 GJ/m^2. In the former region, there is a distinct meridional contrast, with pycnocline heat content being relatively high just north of the continental shelf. The regional pattern of TB* largely mirrors that of pycnocline thickness L_p, which varies from less than 25 m in the Atlantic sector to greater than 100 m in the eastern Pacific sector (Figure 2.7c). This symmetry does not hold along the Antarctic coastal margin, where TB* is very low despite L_p being relatively large.

The regional pattern of total pycnocline heat availability, quantified by $\gamma_p = TB^*/SD^*$, is similar to that of TB* (Figure 2.7d). By this metric, pycnocline heat is most accessible in the eastern Pacific Sector, across the Bellingshausen and Amundsen Seas. If an additional amount of winter ice growth equivalent to SD* was to occur in this region, heat would be ventilated at a mean rate of 3–4 $\times$ 10^6 J/m^2 per centimeter (cm) of ice growth. These values are 2–3 times lower in the Atlantic sector and northern Ross Sea. As discussed earlier, the mean ventilation efficiency given by γ_p would only be realized if the entire pycnocline is entrained into the mixed layer. In reality, most of the heat stored within the pycnocline is not accessible via sea-ice-driven entrainment. This is especially the case in regions like the Bellingshausen Sea, where full pycnocline erosion would require an unrealistic amount of winter ice growth. Thus, γ_p gives a distorted view of the true wintertime ventilation efficiency.

A better measure of heat accessibility is given by γ (equation 2.8), which quantifies the efficiency with which sea ice growth may ventilate heat down to an arbitrary depth. As the mixed layer entrains the thermocline, each unit of ice growth will liberate an increasingly larger amount of heat. Therefore, γ is expected to have a strong depth dependence. This depth dependence is examined for four representative offshore regions: Mawson Sea,

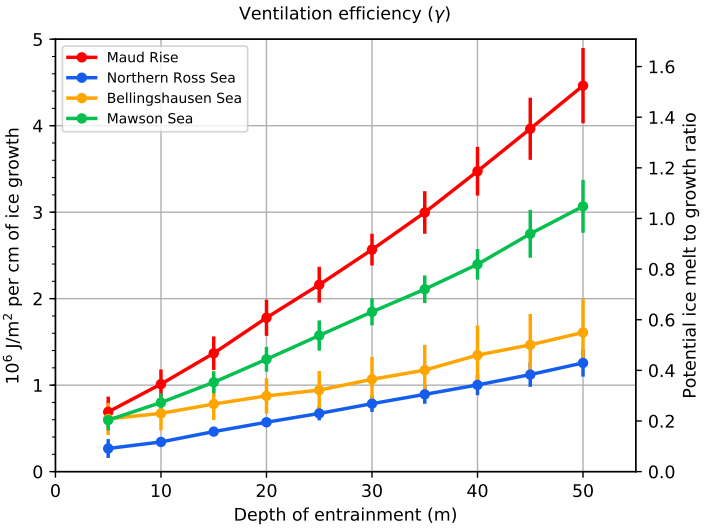

Figure 2.8: Winter mean ventilation efficiency over 50 m of entrainment for the northern Ross Sea, Bellingshausen Sea, Mawson Sea, and the Maud Rise region (see Fig. 2.1 for region boundaries). Errors bars represent one standard deviation.

Bellingshausen Sea, northern Ross Sea, and Maud Rise (Figure 2.8). Among these regions, Maud Rise has the highest wintertime ventilation efficiency. Here, 10 m of sea-ice-driven entrainment would liberate heat at an average rate of 1 MJ/m^2 (10^6 joules per meter squared) per cm of ice growth. Equivalently, this amount of sea-ice-driven entrainment would release enough heat to melt roughly 35% of the initial ice growth. Ventilation efficiency is slightly lower in the Mawson Sea, and significantly lower in the Bellingshausen and northern Ross Sea. In the latter region, a similar amount of entrainment would liberate heat at an average rate of 0.35 MJ/m^2 per cm of ice growth. These regional efficiency rates increase for larger amounts of entrainment. With 30 m of sea-ice-driven entrainment, the expected ventilation efficiency over Maud Rise is 2.5 MJ/m^2 per cm of ice growth. In this scenario, enough heat would be ventilated to melt close to 90% of the initial ice growth.

From these results, we conclude that the Maud Rise region has an exceptionally strong negative feedback, or resistance, to winter sea ice growth. The strength of this feedback is

expected to increase throughout the winter until ice growth is suppressed completely. This negative feedback is also relatively high in some regions along East Antarctica, but is notably lower in the Pacific sector. These results are consistent with the regional pattern obtained by comparing the strength of the thermocline to the strength of the corresponding halocline (Figure 2.6d).

2.6 Summary and discussion

In this chapter, an analysis of the thermodynamic coupling between winter sea ice growth and upper ocean stratification in the Southern Ocean is presented. Part of this effort involved quantifying the upper ocean's susceptibility to deep convection and the accessibility of heat below the mixed layer. To this end, modified versions of the bulk stability metrics introduced by Martinson (1990) and Martinson and Iannuzzi (1998) were developed. These metrics were evaluated for the entire winter sea ice zone using observed under-ice CTD profiles, mainly from Argo floats and instrumented seals. This analysis reveals a contrasting pattern of upper ocean stability across the Atlantic and Pacific Ocean sectors. In the latter region, specifically the offshore regions of the Bellingshausen and Amundsen Sea, the additional winter sea ice growth that is needed to fully erode the pycnocline, as quantified by SD^*, is several times larger than the sea ice growth that normally occurs in a single winter season. This indicates that offshore wintertime deep convection is extremely unlikely to occur in these areas. In the Atlantic sector, in particular near the Maud Rise seamount, SD^* is comparable to the total amount of ice growth that occurs in a winter season. Given that the computation of SD^* neglects multiple non-ice-related processes that may erode the pycnocline, such as wind-driven mixing, these observations suggest that large swaths of the Weddell region are somewhat vulnerable to wintertime deep convection. However, the weak pycnocline in these regions also support a relatively sharp thermocline. This combination of weak stratification and large sub-mixed-layer temperature gradient favors a high rate of wintertime heat ventilation and a strong negative feedback to ice growth. More generally, the off-shelf regions across the southern Atlantic sector and along the East Antarctic shelf

break are characterized by relatively high ventilation efficiency. Thus, a given amount of winter sea ice growth in these regions will ventilate more heat compared to elsewhere in the sea ice zone.

A key takeaway from this analysis is that the Weddell Sea is exceptional in its ability to ventilate deep ocean and modulate winter ice growth. Therefore, we need exercise caution when generalizing the nature of wintertime ice-ocean coupling in the Antarctic sea ice zone. Furthermore, the unique thermohaline structure of the Weddell Sea will shape how the region responds to future changes in surface conditions. For example, based on our results, changes in surface freshwater fluxes are expected to have a large impact on ice growth and heat ventilation in the Weddell Sea compared to other regions in the sea ice zone. Similarly, changes in winds stress curl and wintertime storminess are expected to illicit a relatively strong response in the Weddell Sea. Thus, accurate projections of the climate in Antarctic region will require a nuanced understanding and representation of these regional upper ocean properties.

Chapter 3

SIMULATIONS OF WINTERTIME SEA ICE-OCEAN FEEDBACKS

(Contents of this chapter have been previously published in Wilson, E. A., S. C. Riser, A. Wong and E. C. Campbell (2019), Winter upper ocean stability and ice-ocean feedbacks in the sea ice-covered Southern Ocean, Journal of Physical Oceanography, 49, 1099–1117, doi: 10.1175/JPO-D-18-0184.1.)

3.1 Introduction

The observational analysis presented in Chapter 2 demonstrates that the availability of thermocline heat varies greatly within the winter sea ice zone. The rate at which this subsurface heat is ventilated will also depend on the atmospheric forcing. In principle, if the surface fluxes of buoyancy and momentum are known, one could accurately predict the ventilation rate for a given region. However, our ability to do so is greatly limited by large uncertainties in the surface forcing, specifically the freshwater flux from sea ice. Here, this issue is sidestepped by addressing the related, but more tractable, question of how a given slab of sea ice will evolve in different ocean regions under identical atmospheric forcing. This is done using an idealized, 1D sea ice-ocean model. The purpose of this exercise is not to accurately reproduce observations. Rather, our intent is to isolate and diagnose the thermodynamic coupling between winter ice growth and ocean ventilation across the sea ice zone. In doing so, we aim to build intuition for how the ice-ocean system will respond to changes in ocean stratification and surface forcing on various timescales.

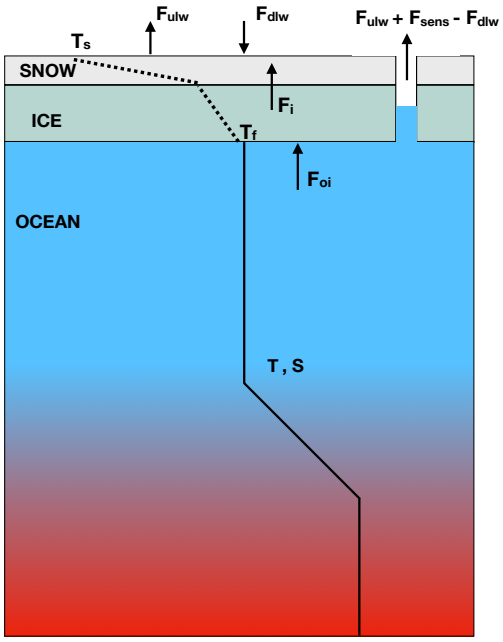

Figure 3.1: Schematic showing the key processes represented in the idealized 1D thermodynamic ice-ocean model. The snow and ice layers are modeled following Semtner (1976). These layers are treated as single slabs with linear temperature profiles. Mixing within the ocean layer is simulated using the Price-Weller-Pinkel upper ocean model (Price et al., 1986). T_s and T_f represent the temperatures of the snow surface and ice base, respectively. F_{ulw}, F_{dlw}, F_i, F_{oi}, and F_{sens} are the heat fluxes due to upward longwave radiation, downward longwave radiation, conductive heat transfer through ice and snow, and sensible heat transfer, respectively. Key model parameters are listed in Table 3.1. Further details are provided in the text.

3.2 An idealized 1D ice-ocean model

3.2.1 Upper ocean

To simulate vertical mixing in the upper ocean, we used a modified version of the Price-Weller-Pinkel (PWP) mixed layer model (Price et al., 1986). Several studies have employed this model to simulated upper ocean mixing in sea-ice-covered regions (e.g. Dewey et al., 2017; Biddle et al., 2017). Most notably, Hyatt (2006) used a modified version of the PWP model to simulate wind-driven, under-ice mixing along the western Antarctic Peninsula. In essence,

this model parameterizes the vertical mixing that results from static and shear instabilities. Static instabilities are resolved using a convective adjustment scheme that mixes a statically unstable layer with progressively deeper layers until the entire profile becomes statically stable. Shear instabilities are assessed and resolved using bulk and gradient Richardson number stability criteria. Following other applications of the PWP model (e.g. Toole et al., 2010), a linear drag term is added to the momentum budget to crudely parameterize the momentum loss associated with the radiation of internal waves. This drag term has a decay timescale of 5 days, which is roughly 10 times greater than the local inertial period.

The PWP model is driven by surface fluxes of heat, freshwater, and momentum. The model uses a time interval of 6 hours and a vertical resolution of 0.5 m (see Table 3.1). At each time step, the model applies surface fluxes to the ocean profile, then resolves any static or shear instabilities that are introduced. After the profile is stabilized, surface fluxes from the next time-step are applied and the process is repeated.

3.2.2 Thermodynamic sea ice

To simulate sea ice growth, we use a simplified version of the sea ice model introduced by Semtner (1976). This model treats snow and sea ice as homogenous slabs with linear temperature profiles (Figure 3.1). At the surface, the model is driven by the balance of upward and downward longwave radiation and the diffusion of heat through the snow and sea ice layers. The latter is determined using the thermal conductivities for snow and sea ice employed by Semtner (1976). Given our focus on the winter season, we assume that shortwave radiation and air-ice sensible and latent heat fluxes are negligibly small. Based on values obtained from ERA-Interim atmospheric reanalysis (Dee et al., 2011), we forced the model with a typical wintertime downward longwave heat flux of 200 W m^{-2}.

At the base of the ice, accretion or ablation is governed by

$$\frac{dh_i}{dt} = \frac{1}{L_i \, \rho_i} \left(F_i - F_{oi} \right), \tag{3.1}$$

where h_i is ice thickness, F_i is the upward conductive heat flux through sea ice, and F_{oi} is

Table 3.1: Table summarizing key parameters and constants used in the idealized 1D ice-ocean model.

Symbol	Description	Value
F_{dlw}	Downward longwave radiation	200 W m^{-2}
T_f	Freezing point of seawater	-1.86 °C
κ_i	Thermal conductivity of sea ice	2 W m^{-1} K^{-1}
κ_s	Thermal conductivity of snow	0.31 W m^{-1} K^{-1}
ρ_0	Reference density of seawater	1027 kg m^{-3}
ρ_i	Density of sea ice	920 kg m^{-3}
ρ_a	Density of air	1.2 kg m^{-3}
c_h	Ocean-ice heat transfer coefficient	0.0056
c_w	Specific heat capacity of seawater	4180 J kg^{-1} K^{-1}
c_a	Specific heat capacity of air	1000 J kg^{-1} K^{-1}
L_i	Latent heat of fusion of ice	3.3 $\times 10^5$ J kg^{-1}
S_i	Salinity of sea ice	4 PSU
Δz	Vertical resolution of ocean model	0.5 m

the ocean-ice heat flux. The resulting change in the surface salinity of the ocean, ΔS, is given by

$$\Delta S = \frac{\Delta h_i}{\Delta z}\,(S_{z=0} - S_i), \tag{3.2}$$

where Δz is the thickness of the ocean surface layer, $S_{z=0}$ is surface ocean salinity, and S_i is a reference sea ice salinity.

To maintain focus on the coupling between ice growth and ocean ventilation, we ignore the effects of snow accumulation and the possibility of snow-ice formation. The latter is an alternate mode of ice formation that occurs when the weight of the snow layer depresses the

ice surface below sea level (Eicken et al., 1995). The distinction between basal ice growth and snow-ice formation is of secondary importance to the ice-ocean feedbacks that are of interest in this study. Though the amount of brine may be significantly different, the ocean's response will be fundamentally the same.

3.2.3 Ice-ocean coupling

The sea ice and ocean layers are thermodynamically coupled via an ocean-ice heat flux, F_{oi}. Following McPhee (1992), F_{oi} is parameterized as

$$F_{oi} = c_w \, \rho_w \, c_h \, u^* \, (T_{z=0} \, - \, T_f), \tag{3.3}$$

where c_h is a turbulent heat exchange coefficient and u^* is the friction speed at the ice-ocean interface. Using the results from McPhee et al. (1999), we set c_h to be 0.0056. The friction speed u^* is equivalent to the square root of the kinematic ice-ocean stress, which is given by

$$u^* = (|\tau_{oi}|/\rho_w)^{1/2}. \tag{3.4}$$

The ice-ocean stress τ_{oi} is determined using the "rule-of-thumb" relationship proposed by Martinson and Wamser (1990), whereby τ_{oi} is assumed to be one-third the magnitude of the air-ice stress τ_{ai}, which is given by

$$\tau_{ai} = \rho_a \, C_{ai} \, U_0 \, \mathbf{u}, \tag{3.5}$$

where $C_{ai} = 2.36 \times 10^{-3}$ is the air-ice drag coefficient, ρ_a is the density of air, and U_0 and $\mathbf{u}$ are respectively the wind speed and wind velocity at 10 m above the sea surface. The open-water fraction is set to a constant value of 0.05, which is typical for the winter sea ice zone. Given this assumption of near total winter sea ice cover, we take τ_{oi} as an approximate value for the total stress applied to the ocean surface.

3.2.4 Ocean heat loss through leads

Since the sea ice and snow layers effectively insulate the ocean, a disproportionate amount of ocean heat is lost through leads. For simplicity, we only consider the heat losses that occur via

blackbody longwave radiation and sensible heat fluxes, F_{sens}, which together account for most of the oceanic heat loss to the atmosphere during the winter. The former is partially offset by the prescribed downward longwave heat flux described earlier. The latter is estimated using the simple bulk formula described by Friehe et al. (1976):

$$F_{sens} = (1 - \alpha)\, \rho_a\, c_a\, C_H\, U_0\, \Delta T_a, \tag{3.6}$$

where α is a prescribed sea ice area fraction, c_a is the heat capacity of air, U_0 is the near-surface wind speed, ΔT_a is the air-sea temperature difference, and $C_H = 1 \times 10^{-3}$ is the bulk transfer coefficient for sensible heat. Without an atmospheric model to determine T_a, we simply assume a typical wintertime air-sea temperature difference of 20°C.

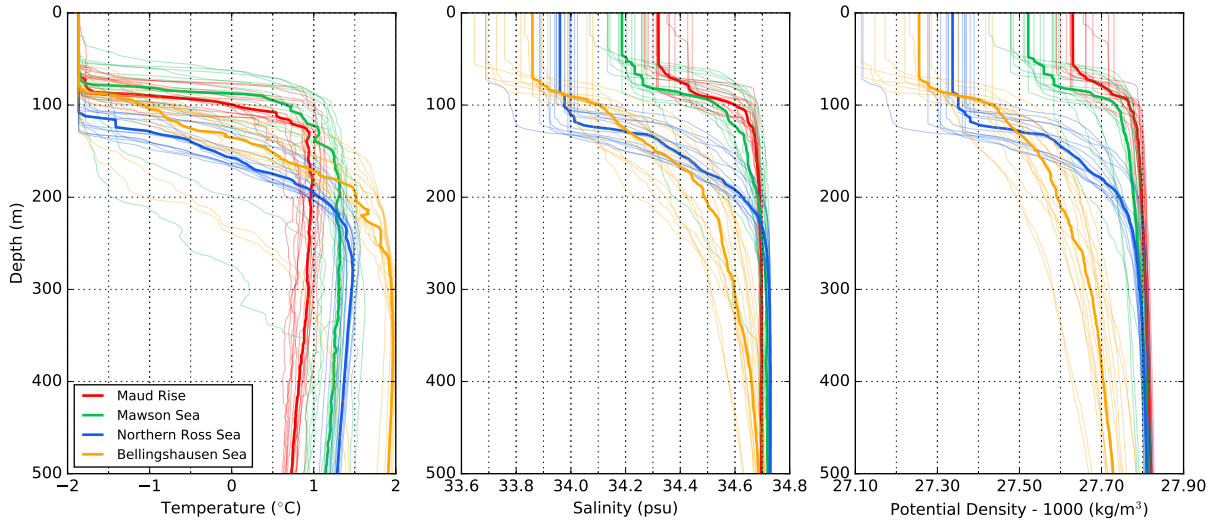

Figure 3.2: Argo float profiles (thin lines) from June that are used to initialize the idealized 1D model simulations, color coded by region (see Fig. 2.1 for region boundaries). As a visual aid, the median profile for each region, represented by thick lines, is shown.

3.2.5 Initial conditions and surface forcing

Model runs were initialized using ensembles of early winter Argo float profiles from the northern Ross Sea, Maud Rise, Bellingshausen Sea, and Mawson Sea (Figure 3.2). These

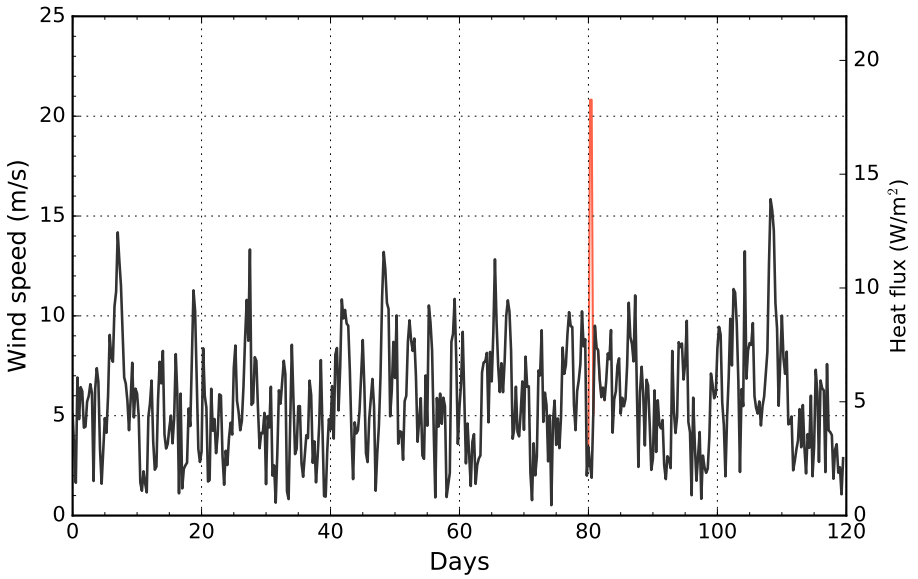

Figure 3.3: The artificially-generated time series of wind speed that is applied to the profiles shown in Figure 3.2. The black line represents the control forcing that replicates moderate winds in the winter sea ice zone. The red line highlights the storm perturbation period. The ocean-air sensible heat flux is given by (3.6) and is scaled by the open water fraction (0.05).

regions were chosen because they span the observed range of upper ocean stratification and heat availability across the offshore regions of the winter sea ice zone (Figure 2.7). From each region, we randomly selected 15 float profiles collected in the month of June, and used each profile to initialize a model simulation. Each initial profile was then forced with identical surface conditions for 120 days, thereby simulating one full winter season. For our control forcing, we constructed an artificial time series of surface winds that replicate moderate winter conditions in the sea ice zone (Figure 3.3). Following Bretherton et al. (1992), each component of the wind vector was generated using the following formula for a red noise sequence $p_r(t)$:

$$p_r(t) = a\, p_r(t-1) + p_w(t)\,(1-a^2)^{1/2}, \tag{3.7}$$

where a is the lag-1 autocorrelation coefficient and $p_w(t)$ is a randomly generated white noise sequence. To obtain $p_r(t)$, we set $p_t(0) = p_w(0)$ and integrate forward in time. Based on

grid-point estimates of 10 m wind velocity for the Weddell Sea region from 6 hourly ERA-Interim atmospheric reanalysis (Dee et al., 2011), we find that the lag-1 autocorrelation for surface winds is approximately 0.9. We therefore set $a = 0.9$ in (3.7). The x- and y-components of the wind velocity were then adjusted and scaled to have zero mean and a standard deviation of 5 m/s. Our experiments were repeated using different sets of wind forcing, which were obtained by seeding (3.7) with different white noise sequences. We find that our main results are not sensitive to the precise nature of our artificially generated red noise. A similar approach could be used to construct an artificial time series for the downward longwave radiation. However, we find that doing so does not fundamentally alter our main results.

Each run is initialized with 30 cm of sea ice and 5 cm of snow, which are typical early winter values for the region (Worby et al., 2008). Sea ice thickness was allowed to evolve, but snow depth and sea ice fraction were kept constant.

3.3 Model Results

3.3.1 Control experiment with moderate winds

Results from the control experiment demonstrate that the thermohaline structure of the upper ocean significantly influences winter sea ice growth in the Southern Ocean (Figure 3.4). Sea ice growth in runs initialized with profiles from the strongly stratified northern Ross Sea was weakly affected by the entrainment of heat into the mixed layer. In these runs, sea ice grew continuously throughout the winter and reached a median thickness that is similar to that produced in the absence of ocean heat fluxes (dashed line). At the other extreme, ice growth was heavily suppressed in the Maud Rise simulations, with the eventual net ice growth being 50% less than the case without ocean heat fluxes. The Maud Rise runs also featured the highest rates of ocean heat loss (Figure 3.4b). After day 40 when sea ice thickness in the Maud Rise simulations began to plateau, the corresponding ocean heat flux mostly varied between 20–50 W m^{-2}. Despite the idealized nature of these experiments, this

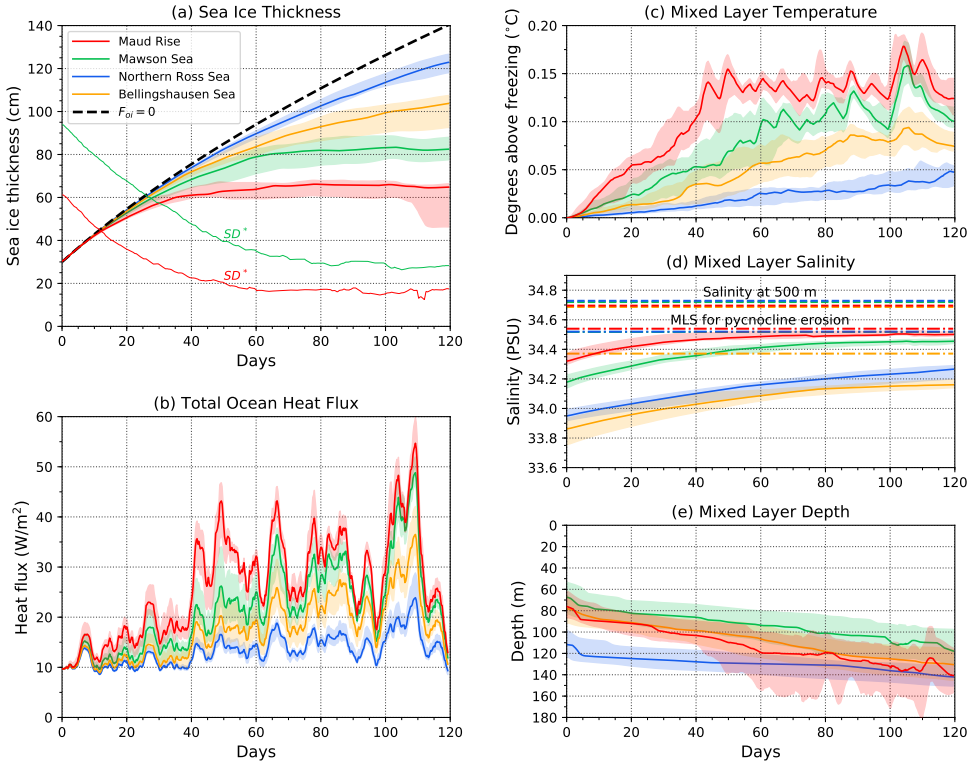

Figure 3.4: The simulations of sea ice thickness and upper ocean properties using the control forcing: (a) sea ice thickness, (b) ocean heat loss, (c) MLT, (d) MLS, and (e) MLD. The solid lines and shading represent the median value and interquartile range (25% – 75% percentile) for each regional ensemble, respectively. In (a), the dashed black line represents the evolution of sea ice in the absence of ocean heat fluxes and the thin lines show the pycnocline salt deficit (SD*). SD* for the Bellingshausen Sea and northern Ross Sea exceeds the range of sea ice thickness shown in (a). In (d), the dashed lines represent salinity at 500 m, while the dash-dot lines represent the MLS required for full pycnocline erosion. Each time series has been smoothed with a 2-day running mean filter.

range of winter ocean heat loss agrees well with observations (e.g. McPhee et al., 1999). In contrast, the ocean heat flux for the northern Ross Sea simulations varied between 10–20 W m^{-2}.

The evolution of MLS mirrors that of sea ice thickness (Figure 3.4d). For the latter half of the Maud Rise simulations, less than 20 cm of additional sea ice growth would have

guaranteed full erosion of the pycnocline (Figure 3.4a). However, this amount of sea ice growth was never realized, as the entrainment heat flux eventually grew to balance the heat loss at the surface. In general, MLD steadily increased throughout each simulation (Figure 3.4e). However, in a few of the Maud Rise ensemble members, fluctuations in the ocean heat flux led to brief periods of ice melt and mixed layer shoaling (not shown).

These idealized experiments were repeated using different values for initial sea ice and snow layer thicknesses ranging from 25–75 cm and 5–15 cm, respectively. Results from those experiments are qualitatively similar to the case presented here. These results are also not sensitive to modest changes to the open-water fraction and surface air temperature. However, we do note that the results for the Maud Rise simulations are somewhat sensitive to the vertical resolution of the ocean model. Choosing a vertical resolution coarser than 5 m produces a notable increase in the variability of the ocean-ice heat flux and leads to more frequent episodes of ice melt. This is the case since a coarser vertical resolution causes entrainment to occur in larger steps.

3.3.2 Storm perturbation experiments

When forced with moderate winds, the Maud Rise ice-ocean system evolves to a state in which the ocean-ice heat fluxes approximately balance the conductive heat flux through the ice. To test the sensitivity of this late winter equilibrium, the previous experiment was repeated with the addition of a storm on day 80 (red line in Figure 3.3). During this perturbation period, a maximum wind speed of approximately 21 m/s (∼40 knots) was imposed for 12 hours. This wind event is similar in magnitude to strong winter storms observed in the Weddell (e.g. McPhee et al., 1996).

For the Maud Rise simulations, the introduction of this storm triggered an abrupt increase in MLT (Figure 3.5). This resulted from the enhanced shear-driven entrainment associated with the large input of momentum at the ocean surface. This warming, coupled with the increase in u^*, amplified the ocean-ice heat flux. The magnitude of the ocean heat loss varied greatly among the ensemble members, ranging from 50–200 W m^{-2}. In response, sea

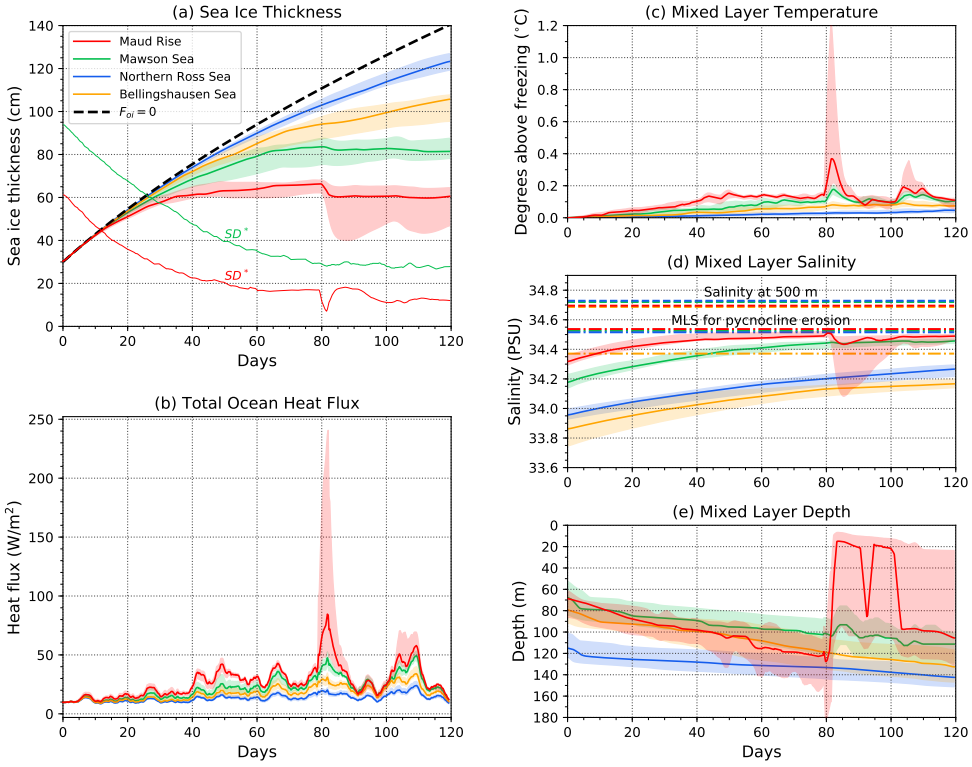

Figure 3.5: As in Figure 3.4, but for the storm perturbation forcing as shown in Figure 3.3.

ice thinned by 5–20 cm and created a shallow melt water layer that persisted for several days. In the other regional simulations, the impact of the storm ranged from weak to negligible. Introducing the storm at a different time, in the latter half of the simulation, produces results that are qualitatively similar to those described here. However, we note that the amplitude of the ocean response in the Maud Rise simulations is somewhat sensitive to the timing of the storm.

From these results, we can infer circumstances that may lead to greater melt or even the complete elimination of the winter ice layer. First, it is evident that a weaker pycnocline promotes thinner sea ice and a stronger response to wind events. Additionally, since the impact of wind-driven mixing diminishes with depth, a shoaling of the thermocline would also favor higher ventilation rates. Lastly, a simple increase in the frequency of winter storms would

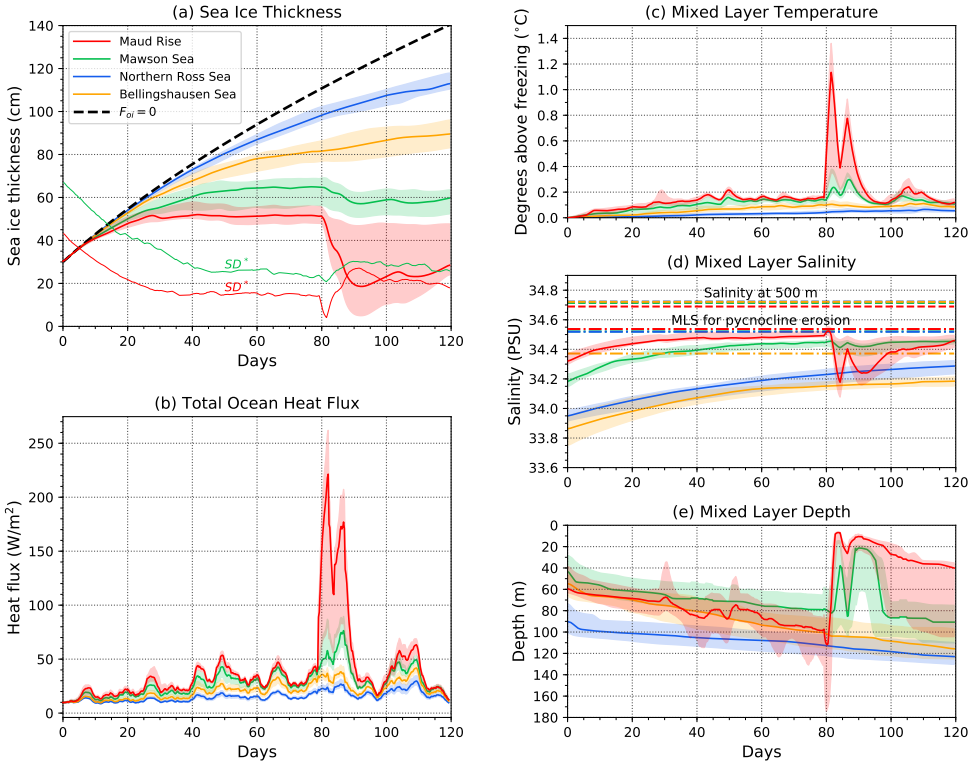

Figure 3.6: As in Figure 3.5, but with the initial profiles shifted upward by 25 m and a second identical storm added on day 85.

also increase the likelihood of major wintertime melt events. To demonstrate the compounding effects of these processes, the previous experiment was repeated with two modifications. First, the initial profiles were shifted upward by 25 m. This was done by truncating the mixed layer. For comparison, Gordon and Huber (1990) estimates an upwelling rate of 45 m per year across the Weddell region. Additionally, a second storm, identical to the first, was added on day 85. The shoaling of the thermocline led to stronger suppression of ice growth (Figure 3.6). For the Maud Rise and Mawson Sea simulations, this is evident in the days leading up to the storm events. In the Maud Rise runs, the storm events triggered an extended period of exceptionally high ocean heat loss and a dramatic change in sea ice thickness, which declined to 10-50 cm across simulations following the storm events. As before,

the magnitude of this response varied greatly among the regional ensemble members. This extreme perturbation produced a similar but more muted response in the Mawson Sea simulations. However, the ice-ocean system in the other regional simulations remained largely unaffected.

3.4 Summary and discussion

The observational assessment presented in Chapter 2 are further supported by results from idealized experiments with a 1D sea ice-ocean model. In our control simulations, which featured moderate wind conditions, simulations initialized with profiles from the Maud Rise region evolved to a state in which ocean-ice heat fluxes approximately balanced the atmospheric cooling imposed at the sea ice surface. This balance was maintained over the latter half of winter, during which sea ice thickness was approximately constant. At the other extreme, sea ice growth in simulations initialized with profiles from the northern Ross Sea was largely unaffected by the comparatively small entrainment of heat into the mixed layer. From the latter result, we speculate that ice growth in similarly strongly stratified regions near the winter sea ice edge are also weakly affected by the entrainment of heat from the thermocline.

The Maud Rise simulations provide a clear example of the winter ice-ocean feedback mechanism envisioned by Martinson (1990). Even though the Maud Rise water column is seemingly susceptible to deep convection, the heat entrained into the mixed layer is able to suppress ice growth and limit further erosion of the pycnocline. Additional model experiments show that the surface stress imparted by a typical one day storm event can disrupt this balance and cause substantial ice melt. The magnitude of the ocean response is critically dependent on the stratification of the water column at the moment the storm is applied. For the Maud Rise simulations, the ensuing rate of ocean heat loss was 2–3 times higher than the case with moderate winds. This response can be greatly amplified by strong upwelling, which exposes the thermocline to more intense wind-driven mixing. In the other regional simulations, which featured stronger stratification, the storm had a weak effect on ventilation

rates. These results suggest that the cumulative wintertime ventilation of the deep ocean heat in weakly stratified regions is dominated by short-lived storm events. Examples of such events were documented during the ANZFLUX survey of the Maud Rise region during the winter of 1994 (McPhee et al., 1996, 1999). In one case, the passing of a powerful storm, which featured gusts up to 25 m/s, produced ocean heat fluxes that exceeded 100 W m^{-2}. This was several times larger than the mean heat flux measured over the six-week survey.

Given our results, we hypothesize that a series of exceptionally strong storms, acting on a shoaled pycnocline that is sufficiently weak, could release enough heat to completely melt the winter ice cover. This assertion is consistent with the tendency for transient winter polynyas to appear along the flanks of Maud Rise, where the stratification is weak and thermocline is consistently shallow (Comiso and Gordon, 1987; Lindsay et al., 2004; de Steur et al., 2007). This conjecture also agrees with past studies that have linked the appearance of winter polynyas to enhanced upwelling across the Weddell Gyre (e.g. Lemke, 1987; Hirabara et al., 2012; Cheon et al., 2015; Kurtakoti et al., 2018). Given that these oceanic preconditions are important, we emphasize a storm's unique capacity to rapidly ventilate large amounts of heat. Without such an abrupt perturbation, heat fluxes from the thermocline will tend to maintain a thin sea ice cover that undergoes cycles of partial melt and regrowth throughout the winter. This proposed mechanism also complements existing theories that describe how topography-flow interactions over Maud Rise elevate isopycnals along the flanks of the seamount and produce low sea ice concentration in specific areas (e.g. Holland, 2000). The dynamics that arise from these topographical interactions will modulate the evolution of a polynya after it is formed. Though not explored in this study, we speculate that strong surface divergence would further amplify the impact of a storm by advecting ice and meltwater away from the affected region. This mechanism would undermine the restratification of the upper ocean and intensify the surface cooling that drives thermal convection.

With these insights, we acknowledge the idealized nature of our model simulations. One important process that is neglected here is the accumulation of snow, which reduces basal ice growth over the course of winter. This process may play a more important role in limiting

ice growth in regions where the wintertime entrainment heat flux is low. Additionally, our analysis does not account for many 3D processes that can modulate local ocean stratification, ice thickness, and ice areal fraction. Nevertheless, our results can serve as a basis for future work that explores these additional processes in more detail.

Our results indicate that changes to upper ocean salinity will have far reaching impacts on the regional ice-ocean system. Recent studies have linked the freshening of the Southern Ocean to a build-up of deep ocean heat within the sea ice zone (Goosse and Zunz, 2014; Lecomte et al., 2017). Our findings support this relationship, with the added caveat that regions with large sub-mixed-layer heat availability or high rates of sea ice growth will have greater sensitivity to changes in surface salinity. Other studies have suggested that this freshening trend will lead to fewer winter polynyas (e.g. Gordon et al., 2007; de Lavergne et al., 2014). Our results also support this projection, but we caution that changes in the wind forcing, which may lead to stronger upwelling or more frequent winter storms, could counter the effect of this freshening (Campbell et al., 2019). Lastly, this study endorses recent efforts to highlight the coupling between winter sea ice growth and mixed layer entrainment as an important feedback in the Southern Ocean climate system (e.g. Goosse et al., 2018). That stated, our results demonstrate that spatiotemporal variations in stratification exert strong control on the strength of this feedback. More observations and detailed modeling will be needed to properly characterize the variability of this feedback and its susceptibility to future change.

Chapter 4

DRIVERS OF RECENT SEA ICE AND SEA SURFACE TEMPERATURE CHANGE IN THE SOUTHERN OCEAN

4.1 Introduction

In this chapter, attention is shifted to the broader subject of sea ice extent (SIE) and sea surface temperature (SST) variability in the Southern Ocean. Interest in this subject is primarily motivated by the record low seasonal SIE and concurrent record high SST that occurred in late 2016 and early 2017. These anomalies stand in stark contrast to the decades of sea ice expansion and surface cooling that preceded them. This abrupt trend reversal was largely unanticipated and therefore exposes our limited understanding of the Antarctic ice-ocean system. Though several studies have provided valuable insight into the factors that may have led to these anomalies, key aspects of this event are not fully-understood. In particular, it remains unclear whether these abrupt changes were the result of an underlying climatic trend (natural or anthropogenic) or just a serendipitous manifestation of short-term climate variability. Given that sea ice production and surface temperatures are intrinsically linked to the heat and carbon uptake of the Southern Ocean, the answer to this question has profound implications for the global climate.

The next section provides an overview of the 2016–2017 Southern Ocean SIE and SST anomalies as well as the long-term trends leading up to them. This is followed by a statistical analysis that attempts to quantify the role of seasonal, near-surface wind anomalies in initiating the late 2016 sea ice decline. The subsequent section investigates the mechanisms that led to the near record SST anomalies that occurred in early 2017 and presents an updated seasonal mixed layer heat budget for the Southern Ocean. The final section discusses the 2016–2017 SIE and SST anomalies within the context of large-scale climate variability,

focusing on the unusual synchronization of the Southern Annular Mode (SAM), El Niño Southern Oscillation (ENSO), and the Indian Ocean Dipole (IOD).

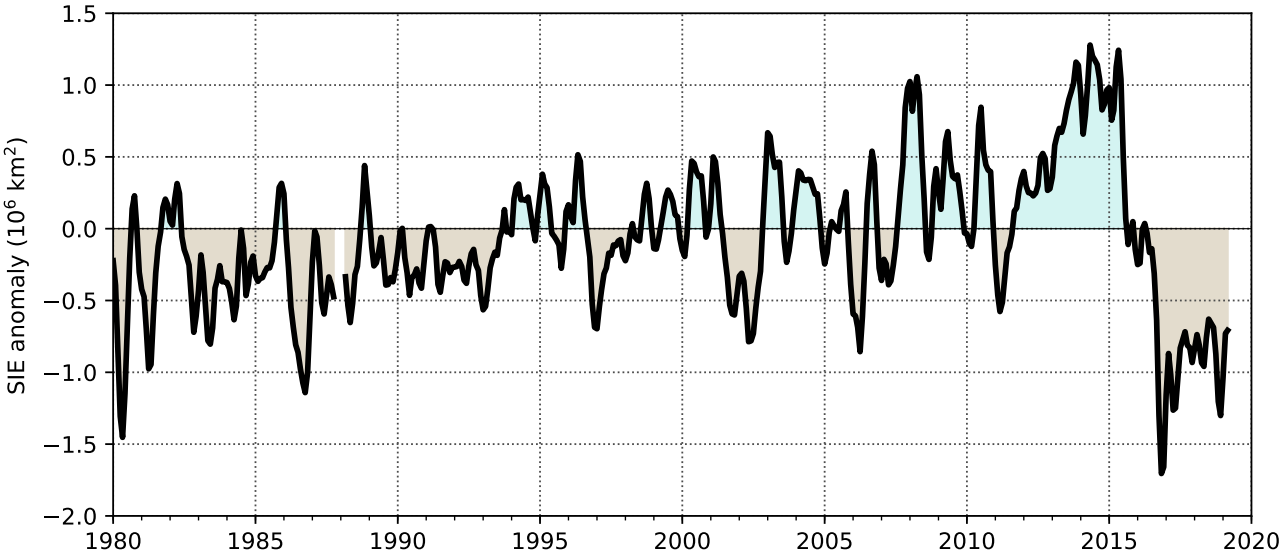

Figure 4.1: Time series showing monthly Antarctic SIE anomalies for 1980–2018 period. Sea ice data were sourced from monthly mean sea ice concentration estimates from version 3 of the CDR (NASA Team Algorithm). Monthly anomalies are computed relative to the climatology for the 1980–2015 period. This time series has been smoothed with a three-month running mean filter.

4.2 Overview of recent SIE and SST trends in the Southern Ocean

Since the late 1970s, there has been a well-documented increase in SIE around Antarctica (Yuan and Martinson, 2000; Cavalieri et al., 2003; Fan et al., 2014). Satellite-based records show that Antarctic SIE has expanded at a mean rate of roughly 1% per decade, with a notable acceleration occurring between 2000–2014 (Figure 4.1; Zwally, 2002; Meehl et al., 2016). This expansion has been near-circumpolar, with the notable exception the Bellingshausen–Amundsen Sea, where the sea ice cover has been declining at a rate of 5% per decade (Figure 4.2; Cavalieri and Parkinson, 2008). Accompanying these sea ice trends are corresponding decreasing trends in SST, with the Southern Ocean surface layer cooling at a mean rate of

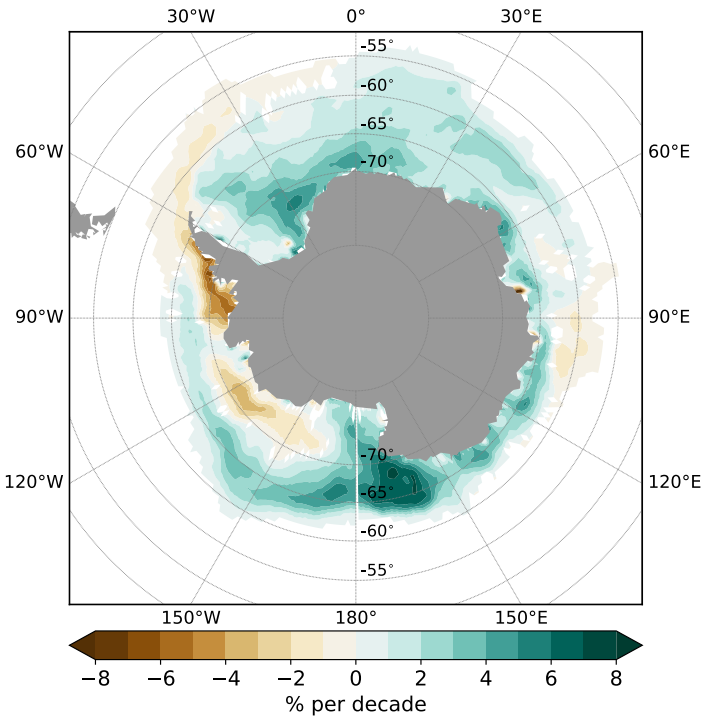

Figure 4.2: Annual mean Antarctic sea ice concentration trend for the 1980–2015 period.

approximately 0.2 °C per decade (Armour et al., 2016, Figure 4.3;). Like the SIE trends, there has been a slight uptick in the rate of surface cooling over the 2000–2015 period. The fact that the pattern of surface cooling extends far beyond the seasonal ice edge (Figure 4.4) suggests that this phenomenon is not a simple consequence of the concurrent sea ice expansion. These sea ice and SST trends exist in stark contrast to the widespread sea ice loss and ocean warming that has occurred in the Arctic over the same period (Zhang, 2005; Stroeve et al., 2007; Parkinson and Cavalieri, 2008).

These decadal trends are the subject of numerous studies. Using modern and historical Southern Ocean observations, Fan et al. (2014) reveal a strong correspondence between variations in Antarctic SIE, Southern Ocean SST, and the strength of the circumpolar westerlies. Based on this evidence, they assert that the recent strengthening of the Southern Ocean westerlies has enhanced equatorward Ekman transport in the upper ocean, effectively

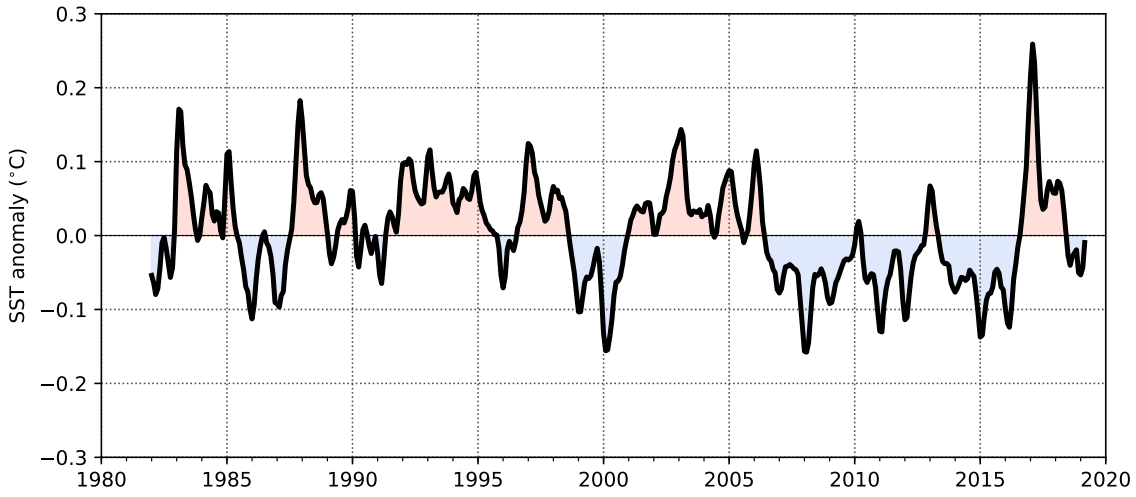

Figure 4.3: Time series showing the seasonal SST anomalies in the Southern Ocean (50°S–65°S) between 1982–2018. SST data were sourced from the NOAA Optimum Interpolation Sea Surface Temperature V2 dataset. Monthly anomalies were computed relative to a 1982–2015 climatology. This time series has been smoothed with a three-month running mean filter.

cooling the surface layers of Southern Ocean while expanding the ice edge. The key importance of surface wind anomalies is further corroborated by Holland and Kwok (2012), who demonstrate that the spatial pattern of sea ice concentration (SIC) trends has strong covariance with wind-driven, ice-drift trends that are derived from satellite data. Other studies have argued that the observed freshening of the Southern Ocean may have contributed to the expansion in Antarctic SIE (Liu and Curry, 2010; Bintanja et al., 2013; Purich et al., 2018). These studies propose that the strengthening of the upper ocean stratification may have reduced the upward flux of heat from the deep ocean, leading to enhanced sea ice growth and surface cooling. Though this mechanism is plausible, its overall contribution to the observed SIE and SST trends is disputed as some modeling studies report a weak correspondence between surface freshening and sea ice expansion (e.g. Swart and Fyfe, 2013; Pauling et al., 2016). Along similar lines, other studies propose that the observed Antarctic sea ice expansion may be due to changes in the thermodynamic coupling between ice growth and ocean

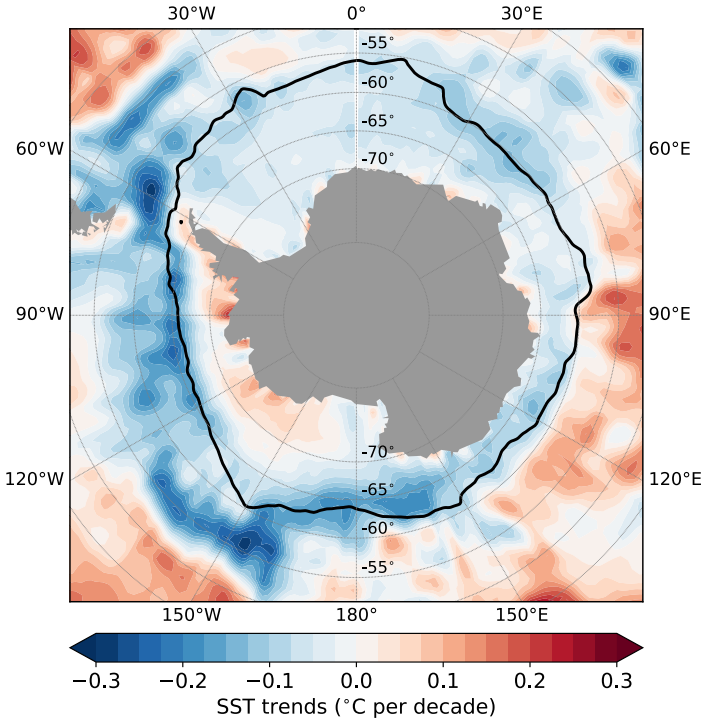

Figure 4.4: Annual mean Southern Ocean SST trend for the 1982–2015 period. Black contour represents the winter sea ice extent

heat ventilation (Zhang, 2007; Goosse and Zunz, 2014; Lecomte et al., 2017; Zhang et al., 2019). Though the precise details of these mechanisms are complex, they ultimately involve some enhancement of upper ocean stratification and a corresponding decrease in ice-ocean heat fluxes. The results from Chapters 2 and 3 support the general idea that an enhancement in upper ocean stratification should lead to an increase in winter ice growth. However, quantifying the contribution of this feedback to the decadal trends in sea ice and SST is hindered by the lack of long-term, under-ice ocean data. In any event, while this feedback mechanism may have contributed to trends within the sea ice zone, it likely cannot account for the surface cooling that has occurred beyond the sea ice edge.

To further complicate matters, most climate models actually simulate surface warming and ice loss across the Southern Ocean over the past few decades (Swart and Fyfe, 2013;

Turner et al., 2013a). The reasons for these discrepancies are not well-understand. Some studies suggest that these differences may be due to biases in the wind forcing used by these models (e.g. Swart and Fyfe, 2012). In particular, climate models tend to underestimate the recent strengthening of the circumpolar westerlies. However, as noted by Armour and Bitz (2015), GCMs that do feature a robust intensification of the Southern Ocean westerlies consistently predict widespread warming and sea ice loss across the region (e.g. Bitz and Polvani, 2012; Sigmond and Fyfe, 2014). This conundrum is perhaps explained by Ferreira et al. (2015), who use results from coupled climate models to demonstrate that the response of the Southern Ocean consists of an immediate sea ice expansion and surface cooling followed by a reversal of these anomalies on longer timescales. The latter warming is linked to the upwelling of relatively warm deep water within the sea ice zone. However, more recent modeling studies have challenged the prediction that such upwelling will be sustained in the long term (Doddridge et al., 2019). In addition to potential biases in the wind forcing, more recent work has suggested that biases in the ocean stratification and heat content may be responsible for the model-data disagreement. Using a high-resolution coupled climate model, Zhang et al. (2019) show that the Antarctic sea ice-ocean system has an internal multi-decadal cycle of sea ice expansion and decline that is linked to the strength of bottom water formation. More importantly, the authors show that simulated SST and SIE trends are highly sensitive to the initial state of the Southern Ocean. Specifically, they find that initializing the model with an ocean that features strong bottom water formation and large offshore polynyas tends to produce SST and SIE trends that are similar to observations. This implies that recent SST and SIE trends may be a direct result of the 1974–1976 Weddell Sea polynyas.

Against this backdrop of multi-decadal surface cooling and SIE expansion in the Southern Ocean, a dramatic reversal of these trends occurred during late 2016 and early 2017 (Figs. 4.1 and 4.3). In November of 2016, the Antarctic sea ice edge retreated at a record rate—almost 20% faster than any season over the past four decades (Turner et al., 2017). This rapid retreat was almost fully circumpolar, with the most prominent ice cover losses occurring

in the Bellingshausen–Amundsen Sea and the northwestern Weddell Sea. Concurrent with this rapid ice edge retreat were anomalously warm SSTs that peaked in early 2017 (Figure 4.3). Stuecker et al. (2017) connected these Southern Ocean anomalies to the exceptionally strong El Niño event that occurred earlier that year, highlighting the tendency of positive ENSO events to induce surface warming in the southeastern Pacific. They also note that the 2015–2016 El Niño event was followed by a strong negative SAM event, a highly unusual sequence of events, and speculate that this rare superposition of internal atmospheric variability may have led to the extreme seasonal sea ice decline. Homing in on the local wind anomalies that occurred in 2016, Schlosser et al. (2018) show that the surface wind anomalies exhibited a distinct zonal wavenumber three pattern, with strong northerly anomalies being coincident with regions that experienced relatively large seasonal ice loss (Figure 4.5). In a subsequent study, Wang et al. (2019) linked these meridional wind patterns to exceptionally intense convective rainfall over the eastern tropical Indian Ocean in September of 2016. They show that these anomalous rainfall events triggered an atmospheric Rossby wave that propagated towards the Southern Ocean and established the surface wind patterns documented by Schlosser et al. (2018). This tropical teleconnection was further corroborated by Meehl et al. (2019), who use simulations from an atmosphere-only GCM to demonstrate that a localized warming anomaly over the tropical Indian Ocean produces atmospheric circulation anomalies over the Southern Ocean that are similar to those observed in late 2016. Additionally, the authors linked the anomalous SSTs to an observed negative trend in wind stress curl across the Southern Ocean that was manifested over the 2000–2015 period. They speculate that subsequent enhancement of warm deep water upwelling preconditioned the region for the dramatic anomalies that occurred in 2016 and 2017.

From these studies, we can conclude with reasonable certainty that anomalous surface winds played an important role in initiating the early Antarctic sea ice retreat observed in late 2016. There is also strong evidence that these wind anomalies were in part triggered by exceptionally strong precipitation over the tropical Indian Ocean. Nevertheless, several aspects of this anomalous event are not well understood. Given that surface wind anomalies

likely triggered the 2016 SIE anomalies, the extent to which the former contributed to the latter remains unquantified. As noted by Wang et al. (2019), even though circumpolar winds were anomalously weak in late 2016, the amplitude of these anomalies were not that far from previous records. Similarly, while the zonal wavenumber 3 pattern highlighted by Schlosser et al. (2018) was clearly anomalous, similar patterns have occurred in the recent past and were not associated with the type of SIE anomalies observed in 2016. Furthermore, the role of the upper ocean in the manifestation of the 2016 anomalies remains unclear. Meehl et al. (2019) argue that this event was the culmination of nearly 15 years of anomalous upwelling across the Southern Ocean. This hypothesis echos the two-timescale response of the Southern Ocean to enhanced westerlies proposed by Ferreira et al. (2015). However, it is not clear how or why this long-term upwelling of warm water manifested itself in such an abrupt fashion. Additionally, even though negative wind stress curl does induce Ekman suction, the amount of upwelling that is realized will be mediated by the overturning caused by mesoscale eddies, which acts in the opposite sense (Marshall and Radko, 2003). This process is poorly constrained by observations and GCMs. In fact some eddy-permitting models even exhibit near perfect *eddy compensation*, whereby Ekman induced changes to isopycnal slopes are almost completely negated by enhanced eddy overturning (Hallberg and Gnanadesikan, 2006; Morrison and Hogg, 2013; Abernathey et al., 2011).

4.3 The 2016–2017 sea ice decline: the role of surface wind anomalies

The goal of this section is to better understand the role of seasonal wind anomalies in initiating the late 2016 SIE anomalies. Here, attention is restricted to local wind anomalies and their impact on the underlying ice field. The cause or origin of these wind anomalies will be discussed in a later section.

4.3.1 Data

This analysis uses observationally based estimates of sea ice concentration (SIC) and surface winds for the Southern Ocean. SIC data were obtained from the National Snow and Ice

Data Center (NSIDC) database. We use version 3 of the NOAA/NSIDC Climate Data Record (CDR) SIC product, which is derived from passive microwave data collected by several polar-orbiting satellites between 1979 and 2018 (Peng et al., 2013; Meier et al., 2017). More specifically, we use the sea ice data derived from the NASA Team algorithm, which provide a continuous record of ice concentration over the modern satellite era. These data are provided on a uniform, 25 km by 25 km, polar stereographic grid. Since this study is primarily concerned with variability on seasonal timescales, we use the version of this product that is provided as monthly averages. To define seasonal anomalies, we use the 1979–2015 period as a baseline and subtract the monthly mean values over that period from each year.

Surface wind estimates were obtained from the ECMWF Interim reanalysis (ERA-Interim) (Dee et al., 2011). ERA-interim is a state-of-the-art global atmospheric reanalysis that blends an expansive suite of observations (primarily from satellites) with a high resolution atmospheric forecast model to produce a dynamically consistent, spatially complete state estimate of the atmosphere. These estimates are available from 1979 to present and are computed in 3-hourly to 6-hourly time steps on a 0.75° by 0.75° spatial grid. As before, we use the monthly averaged version of this dataset and define seasonal anomalies relative to the 1979–2015 climatology.

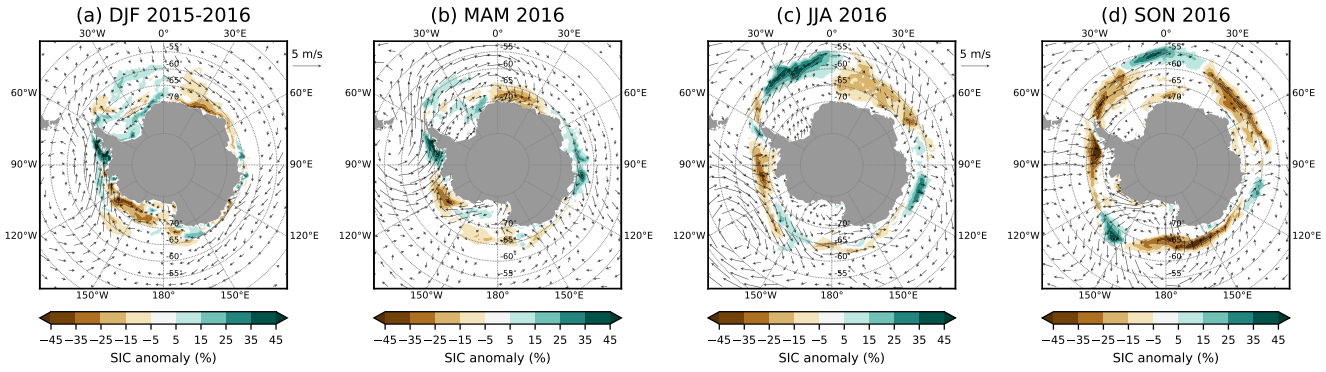

Figure 4.5: Maps showing Antarctic sea ice concentration (shading) and 10 m wind anomalies (arrows) for (a) December 2015–February 2016, (b) March–May 2016, (c) June–August 2016, and (d) September–November 2016. Monthly anomalies are computed relative to a climatology computed from the 1979–2015 period.

4.3.2 The linear relationship between surface wind and SIC anomalies on season timescales

In this section, we seek to quantify the apparent correspondence between surface wind and SIC anomalies in 2016 (Figure 4.5). One approach to doing so would be to construct a seasonal sea ice area budget for the Antarctic region. An example of such a budget is given by

$$\frac{\partial A}{\partial t} + \nabla \cdot (\mathbf{u}A) = f - r, \tag{4.1}$$

where A is sea ice area fraction, $\mathbf{u}$ is the ice drift vector, and f and r are changes in A due to thermodynamic ice melt or growth and mechanical redistribution processes, respectively. Holland and Kwok (2012) used this budget to determine the extent to which trends in ice motion contributed to the aforementioned decadal trends in Antarctic SIC. They quantified the impact of ice advection using satellite-derived ice drift and inferred the contributions of f and r from the residual of the other terms in (4.1). In principle, a similar ice area budget could be constructed to evaluate the processes responsible for the 2016–2017 SIE anomalies. However, such an approach is hindered by limitations in the available sea ice data. First, as noted by Holland and Kwok (2012), the ice-motion tracking algorithm struggles to resolve ice drift when there are rapid (i.e. sub-daily) changes in the ice field. This tends to be the case during summer months, when there is strong surface melt, and along the ice edge, where the relatively thin ice field is strongly modulated the warm currents of the Antarctic Circumpolar Current. Therefore, accurate ice-drift data are only available within the sea ice pack during fall, winter, and possibly during the early weeks of spring. Furthermore, given the sparsity of sea ice thickness data in the Southern Ocean, direct evaluation of the thermodynamic term in (4.1) is not currently possible for sub-seasonal timescales. Thus, current observations do not permit us to accurately evaluate (4.1) in regions that experienced dramatic sea ice loss during the austral spring of 2016. We therefore adopt a different approach.

A key insight from Holland and Kwok (2012) is that surface winds and sea ice motion are strongly correlated in the Southern Ocean. This agrees with the ship-based observations presented by Martinson and Wamser (1990), which reveal that winter sea ice within the

Weddell Sea can be treated as being in a state of "free-drift", meaning that ice motion is weakly affected by internal ice stresses. This result is further supported by Kimura (2004), who use satellite-based ice drift data to show that surface winds in the Antarctic sea ice zone explain between 60%–90% of the variance in ice motion on daily timescales. They also find that turning angle of the ice is generally between 10°–25° to the left of the surface wind vector. From these observations, we hypothesize that this general relationship between wind and ice motion also holds on monthly to seasonal timescales. More specifically, we postulate that poleward surface wind anomalies should lead to anomalously low sea ice cover near the sea ice edge, with the opposite being true for equatorward surface wind anomalies.

To test this hypothesis, we conduct a lagged correlation analysis between local SIC and surface wind anomalies across the Southern Ocean. The goal of this analysis is to (a) quantify the linear relationship between local SIC and surface wind anomalies on seasonal timescales, specifically near the ice edge, and (b) use the derived linear dependence to assess the extent to which local surface wind anomalies contributed to the observed SIC anomalies in late 2016. Here we note that by simply comparing SIC and wind anomalies, we are implicitly assessing both the dynamical and thermodynamical influence of surface winds on the underlying sea ice field. The latter refers to the potential for atmospheric advection to change local air temperature, which in turn can in turn modify thermodynamic sea ice growth. Furthermore, this approach does not directly quantify the impact of other process not directly related to the instantaneous surface wind field (e.g. ice-ocean feedbacks and variations solar radiation). Because of this, we must first quantify the SIC variance that can actually be explained by surface wind anomalies. Lastly, it is important to note that state of the sea ice field in one season can influence SIC in subsequent seasons (Holland, 2014). Though the temporal propagation of SIC anomalies is not directly addressed in our simple linear regression analysis, the potential impact of this process will be discussed throughout this analysis.

In principle, local SIC could depend on both the magnitude and the direction of the wind field. We assess both relationships by regressing local SIC anomalies on the zonal and meridional components of the wind anomalies, which will be referred to as u-wind and v-

wind anomalies, respectively. Additionally, to investigate the temporal dependence of these relationships, the regression analysis is repeated with sea ice anomalies lagged by a different number of months. For example, the lag-1 regression for the austral summer season compares December–February SIC anomalies with November–January wind anomalies. Since we are testing the impact of winds on SIC, we focus our cases where the wind anomalies are either concurrent or leads the SIC anomalies. This analysis is performed at each grid cell, using only data from the 1979–2015 period. Since the CDR sea ice data is on a finer spatial grid than the ERA-interim surface wind data, the former is bin-averaged to be on the same spatial grid as the latter. Visual inspection of the coarsened SIC data reveals that this procedure results in negligible distortion of the sea ice data.

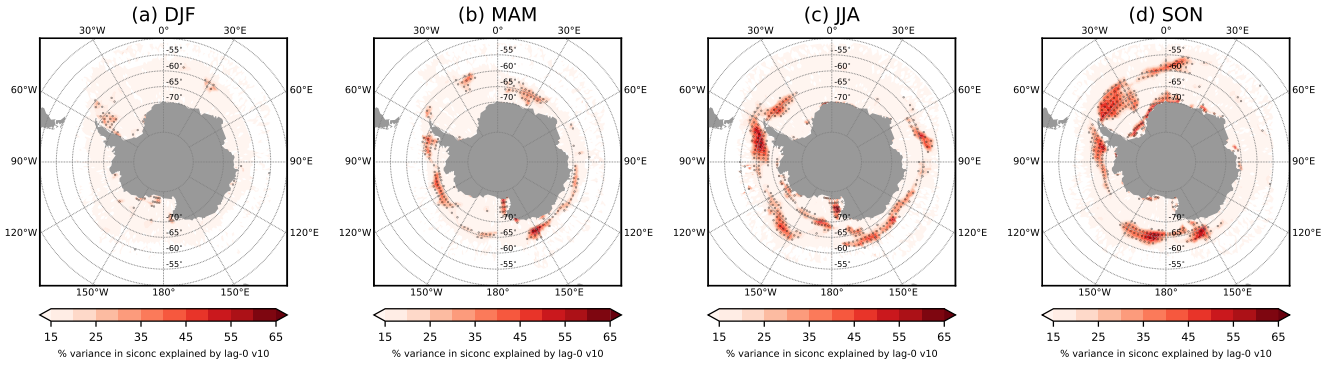

Figure 4.6: Local r-squared values for SIC and concurrent v-wind anomalies. This shows the percent variance in seasonal SIC anomalies that is explained concurrent seasonal v-wind anomalies. Dots indicate areas where the p-value < 0.01, based on a two-tailed test whose null hypothesis is that the slope is zero. This analysis was done using only data from the 1979–2015 period.

To begin, we assess the linear relationship between surface wind and SIC anomalies on monthly timescales. During austral summer, seasonal v-wind anomalies explain almost none of the variance in the concurrent SIC anomaly field (Fig. 4.6a). This is likely the result of there being very little sea ice cover during the summer. Additionally, the impact of surface winds during the summer SIC may be overwhelmed by the effects of solar insolation. The

relationship between v-wind and SIC anomalies is somewhat stronger for March–May, but areas of substantial dependance are limited to small patches scattered across the seasonal ice zone. During austral winter and spring, concurrent v-wind anomalies explain more than 30% (i.e. $r^2 > 0.3$) of the observed variance in SIC anomalies across large swaths of the Pacific and Atlantic sectors. In general, SIC anomalies along East Antarctica, between 30°E and 150°E, has little to no linear dependence on instantaneous v-wind anomalies.

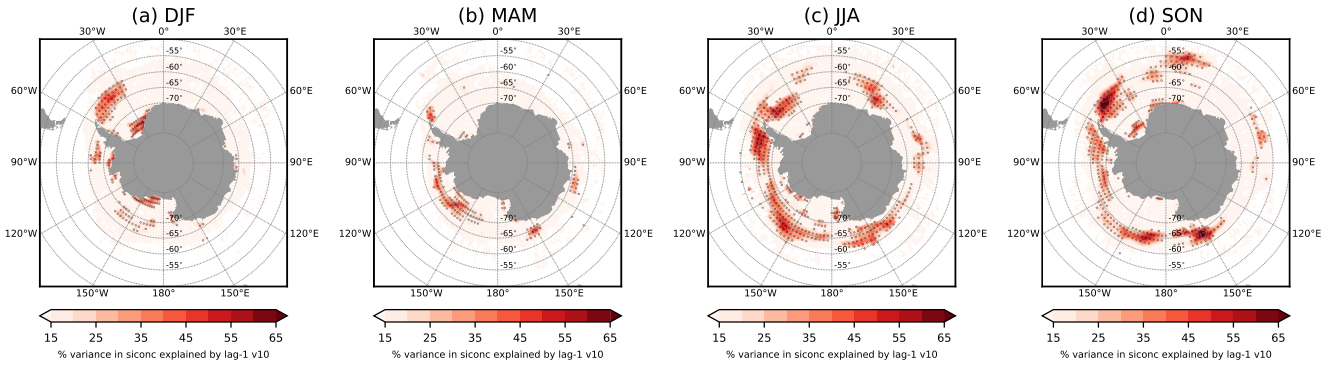

Figure 4.7: Like Figure 4.6 but with v-wind anomalies leading (in time) by 1 month.

Repeating this analysis with SIC anomalies lagged by one month reveals a substantially stronger relationship between SIC and meridional wind anomalies (Fig. 4.7). As before, this relationship is strongest during the winter and fall seasons. In winter, v-wind anomalies over the May–July period explain 30–60% of the SIC anomalies across much of the sea ice zone, especially the Pacific and western Atlantic sectors. A similar relationship is evident in austral spring. This suggests that the impact of surface winds on SIC tends to accumulate over time during the winter and spring seasons. However, repeating this analysis with SIC lagged by two or more months produces a much weaker relationship (not shown). Thus, the effect of surface seasonal v-wind anomalies appears to be primarily limited to several weeks. The reasons for this particular temporal dependence are not immediately clear. The momentum balance of an ice floe in free-drift suggest that an adjustment timescale to time-varying winds that is on the order of a few hours (Martinson and Wamser, 1990). From

this, we might expect that the SIC field to be fully in-sync with overlying winds on monthly timescales. However, as noted by (Holland, 2014), variations in surface winds directly affect the rate of change of sea ice cover (i.e. ice drift velocities) and not the state of the ice cover itself. Moreover, the eventual impact of wind variations on the sea ice cover will also depend on air-sea-ice feedbacks that may amplify or dampen the perturbations induced by the surface winds. For example, when solar insolation is substantial, ice-albedo feedbacks will tend to amplify SIC anomalies. However, when solar insolation is minimal, feedbacks associated with longwave cooling will tend to diminish or even reverse SIC perturbations (i.e. less ice leads to more ocean cooling, which promotes more ice growth). Furthermore, changes in surface winds also disrupts the momentum balance of the upper ocean, which can then feedback onto the ice field via ice-ocean stresses. In short, the physical link between surface winds and SIC is far from straightforward and more work is needed to fully understand the temporal dependence uncovered by this regression analysis.

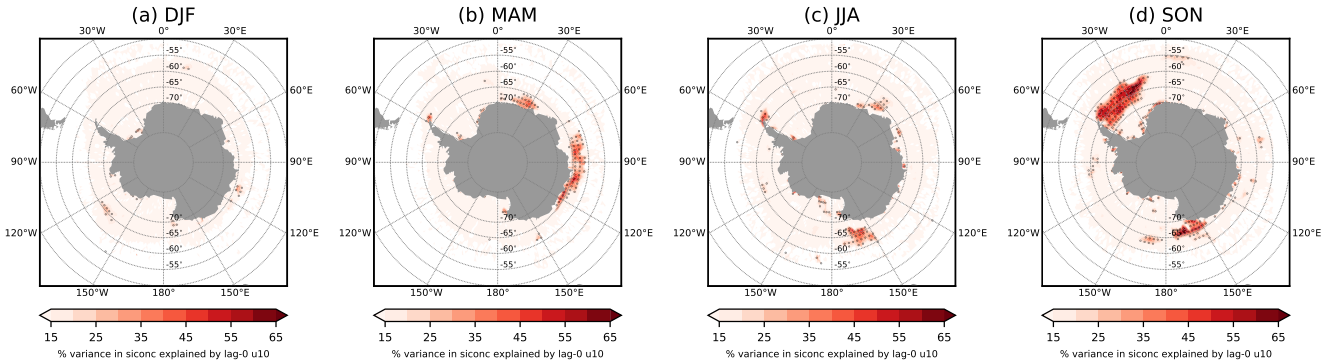

Figure 4.8: Like Figure 4.6 but for lag-0 seasonal u-wind anomalies.

Re-doing the previously described procedure for zonal (i.e. u-wind) anomalies reveals that this component of the surface wind has a much weaker impact on SIC anomalies. The main exception to this generalization is the northwestern Weddell Sea during austral spring (Figure 4.8). In this region, seasonal u-wind anomalies explain more than 50% of the observed variance in the local SIC field. This occurrence is likely due to the presence

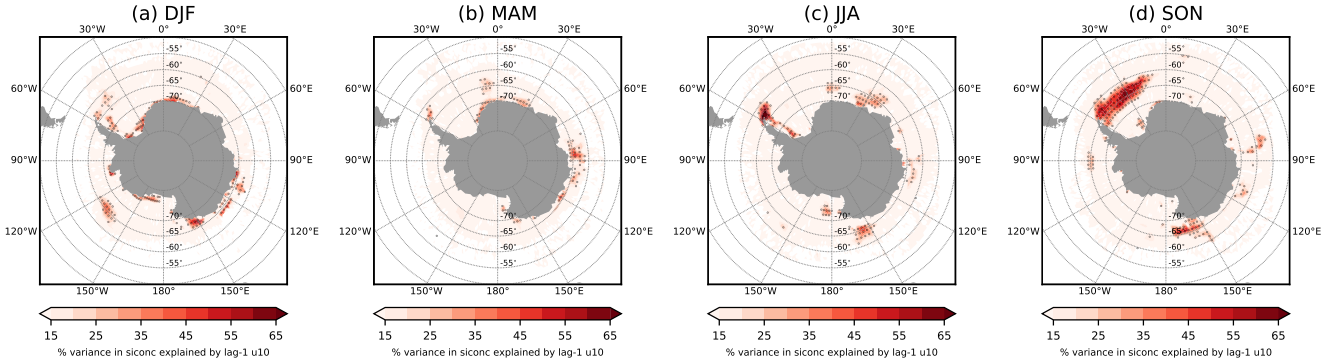

Figure 4.9: Like Figure 4.7 but for seasonal u-wind anomalies leading by one month.

of the Antarctic Peninsula, which inhibits eastward ice flow from the Bellingshausen Sea. Repeating the regression with SIC anomalies lagged by one month produces virtually the same result. As before, lagging SIC anomalies by two or more months produces a noticeably worse relationship than the lag-0 and lag-1 cases (not shown).

In summary, this simple regression analysis reveals that seasonal surface wind anomalies do explain a significant fraction of the observed seasonal SIC anomalies in many regions within the sea ice zone. This relationship is strongest during austral winter and spring in the Pacific sector and in the western Weddell Sea, which importantly coincide with the timing and location of the SIC anomalies that occurred in late 2016. In general, wind anomalies in the meridional direction have a stronger influence on local SIC than wind anomalies in the zonal direction. Additionally, in regions where SIC and wind anomalies are significantly correlated, a stronger relationship is obtained when SIC anomalies are lagged by one month. However, SIC anomalies generally have no clear linear dependence on winds anomalies that occurred two or more months in the past. Based on these results, we restrict our attention to the winter and spring seasons, which feature a strong dependence between the wind and sea ice anomalies. Additionally, since local SIC anomalies appear to have the strongest dependence on wind anomalies that occur one month in the past, we focus on the results obtained by using lagging SIC anomalies by one month.

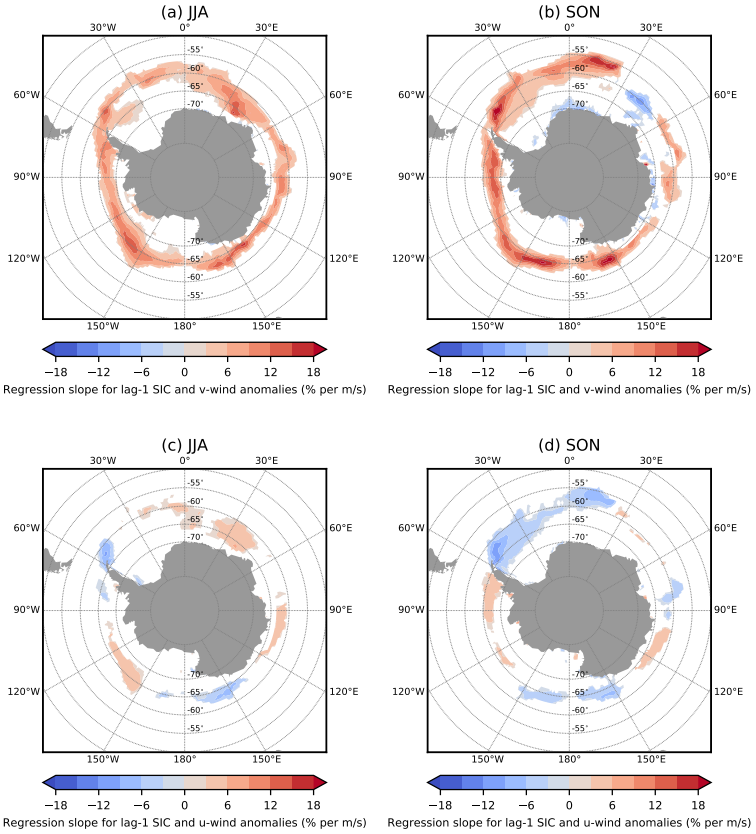

Figure 4.10: Linear dependence of SIC anomalies on local wind anomalies. Top row shows the local regression slope for (a) June–August SIC anomalies and May–July v-wind anomalies and (b) September–November SIC anomalies and August–October v-wind anomalies. Bottom row shows a similar set of relationships but for SIC and u-wind anomalies. As before, this analysis was done using only data from the 1979–2015 period.

Next, we demonstrate the strength of the linear relationship between seasonal SIC and surface wind anomalies, with the latter leading by one month. During winter and spring, v-wind anomalies near the ice edge are associated with the largest seasonal SIC anomalies (Figure 4.10). This is expected since spatial gradients in SIC are largest along the periphery of the ice pack. For June through August, a 1 m/s northward wind anomaly is associated with a 10–15% increase in SIC along the ice-edge. This relationship is circumpolar and includes regions where surface wind anomalies explain a relatively small fraction of the SIC

anomalies. A similar correspondence is observed during September–November. However, for this season, there is a much weaker linear dependence between SIC and v-wind anomalies in the eastern Indian Ocean sector, between 30 °E and 120 °E. As anticipated, SIC has a much weaker linear dependence on u-wind anomalies. This again reflects the fact that spatial gradients in SIC are primarily in the meridional direction. However, consistent with Fig. 4.9, SIC does have a moderate dependence on zonal winds near the ice edge in the western Weddell, downstream of the West Antarctic Peninsula. Here, a 1 m/s eastward wind anomaly is associated with a 5–10% *decrease* in SIC.

4.3.3 The impact of surface wind anomalies in late 2016

Using these local linear relationships, we compute the expected SIC anomalies for 2016 based on the local surface wind anomalies that occurred during that period. As before, we restrict our focus to austral winter and spring, and only present results obtained using SIC anomalies lagged by one month. For the 2016 winter season, we find that the SIC predictions based on May–July wind anomalies reproduce many of the observed features in the June–August SIC anomaly field (Figure 4.11 a–d). In particular, SIC predictions based on v-wind anomalies capture the negative SIC anomalies that occurred in the Bellingshausen–Amundsen Sea (120°W–65°W) and the eastern Weddell and Cosmonauts Seas (0–30°E). These v-wind anomalies also predict the positive SIC anomalies that appeared in the northern regions of the Ross and Weddell Seas. While the u-wind anomalies predict a small fraction of the observed SIC anomalies, they capture the reduction in SIC that occurred near the tip of the Peninsula. Taken together, the sum of the SIC anomalies predicted by u-wind and v-wind anomalies roughly reproduce the observed pattern of SIC anomalies across the Pacific and western Atlantic sectors (Fig. 4.11d). In regions such as the the Bellingshausen–Amundsen Sea and northwestern Weddell Sea, the magnitude of the predicted SIC anomalies agree well with observations. This favorable comparison reaffirms the findings of Schlosser et al. (2018), who linked the anomalous sea ice loss in these regions to poleward wind anomalies. However, in the northern regions of the Ross and Weddell Seas, the predicted SIC

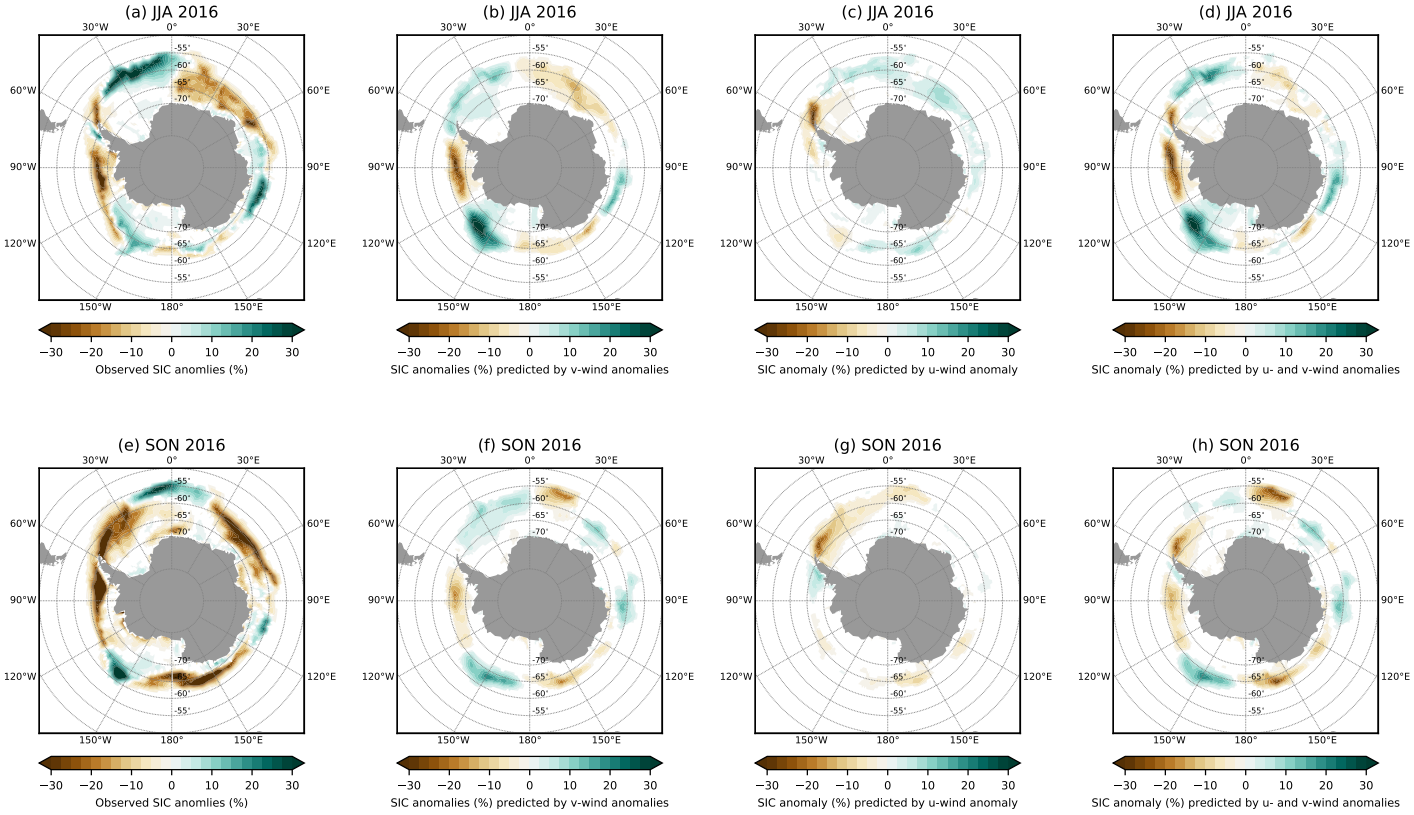

Figure 4.11: 2016 SIC anomalies predicted by surface wind anomalies. Top row: compares the observed SIC anomaly for June–August (a) with that predicted by May–July v-wind, u-wind anomalies and their sum (b, c, and d, respectively). Plot (d) is simply the sum of plots (b) and (c). Bottom row shows a similar set of comparisons for September–November anomalies. The predicted wind anomalies are obtained by multiplying each component of the seasonal wind anomalies with their corresponding regression slopes shown in Fig. 4.10.

anomalies underestimate and overestimate the observed positive SIC anomalies, respectively. Additionally, the sum of the predicted SIC anomalies fails to capture the large swath of reduced sea ice cover in eastern Weddell region. These disagreements are likely the result of physical processes that are not linearly dependent on the strength and direction of near-instantaneous surface wind anomalies.

Repeating the previous analysis for the subsequent spring period reveals a somewhat similar correspondence between predicted and observed SIC anomalies (Figure 4.11 e–f).

First we note that the observed SIC anomaly pattern in September–November bears close resemblance to the anomaly pattern that was apparent during the previous three months. Of note, the reduced winter ice cover in the Bellingshausen–Amundsen Sea persisted into the spring and further intensified. A similar intensification occurred across the eastern Weddell and Cosmonauts Seas. As before, the SIC anomalies predicted by surface wind anomalies largely capture the observed SIC anomaly pattern in the Pacific and western Atlantic sectors. However, the predicted SIC anomalies grossly underestimate the magnitude of the observed sea ice loss in these regions. In particular, the springtime SIC anomalies that occurred in the Bellingshausen–Amundsen Sea and the northwestern Weddell Sea are 2–3 times greater than those predicted by the near-instantaneous surface winds. Similar to the wintertime case, neither component of the surface wind anomalies are able to capture the elongated patch of low SIC that was present in the Indian Ocean sector, between 30°–80°E. Thus, our analysis again suggests that anomalous poleward surface air flow was not the sole factor leading to the extreme ice loss that occurred in late 2016. Furthermore, the broad similarities between the winter and spring SIC anomaly fields suggest that the springtime wind anomalies worked to amplify the SIC anomalies that were already present.

To further examine the relationship between observed SIC anomalies and those predicted by our linear model, we repeat the regression analysis for two test regions: the Bellingshausen–Amundsen Sea (110°W–70°W) and the Cosmonauts Sea (30°E–60°E). These regions are selected as examples because they experienced large SIC anomalies in 2016 and feature varying degrees of covariance between wind and SIC anomalies. Furthermore, by averaging over a wider spatial area, we are able to test the sensitivity of our results to spatial averaging. Consistent with earlier results, we again find that the SIC anomalies predicted by v-wind anomalies closely match the SIC anomalies that occurred in the Bellingshausen–Amundsen Sea during the winter of 2016 (Figure 4.12). The fact that the 2016 case falls almost exactly on the regression line is rather fortuitous considering the moderate covariance between the two variables ($r^2 \approx 0.4$). Further, it is now evident that the meridional wind anomalies that occurred in this region during the 2016 winter were in fact the strongest

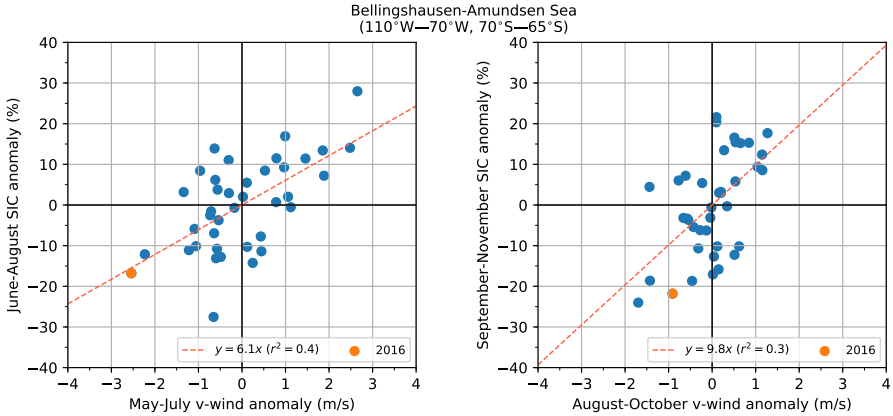

Figure 4.12: SIC anomalies versus v-wind anomalies for the Bellingshausen–Amundsen Sea. The left plot shows winter (June–August) SIC anomalies versus May–June v-wind anomalies. The right plot shows spring (September–November) SIC anomalies versus August–October v-wind anomalies. Dots represent the seasonal SIC and v-wind anomaly for all years between 1980 and 2017—orange dots highlight the year 2016. The dashed red line represents the linear least-squares fit between the SIC and v-wind anomalies.

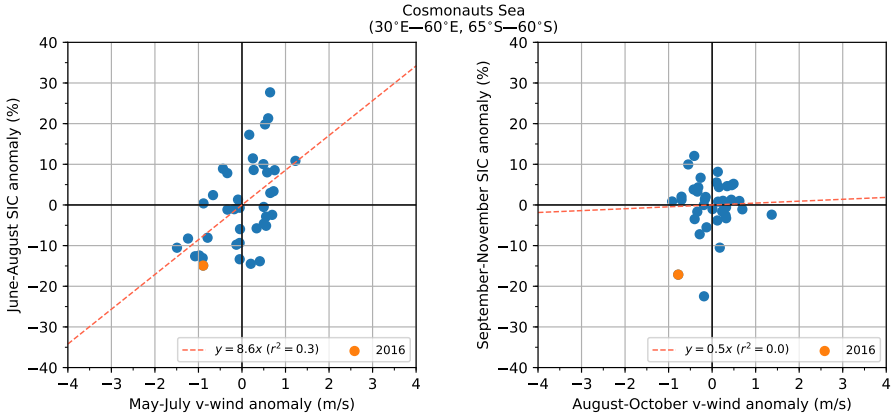

Figure 4.13: Like Figure 4.12 but for the Cosmonauts Sea.

since at least 1980. For the subsequent spring season, we again find that the linear model underestimates the observed SIC anomaly for this season. However, with all years in view, this discrepancy does not seem as egregious. In fact, we see that the deviation from the best fit line is of similar magnitude to the deviations observed for other years. In other words,

the linear model performed as well as one could expect given that v-wind anomalies are not the dominant driver SIC anomalies for this season. Nevertheless, this perspective reinforces the notion that near-instantaneous v-wind anomalies were not the sole or perhaps even the primary cause of the record low SIC that occurred in the spring of 2016. Shifting focus to the Cosmonauts Sea, we again observe that the SIC anomalies that occurred in June–August are largely in line with what one would expect given the v-wind anomalies that were present. However, the SIC anomalies that occurred in the subsequent spring are not all captured by v-wind anomalies. This is expected since this region features no linear correspondence between surface wind anomalies and SIC anomalies during this season.

4.3.4 The reappearance of the Weddell Sea polynyas

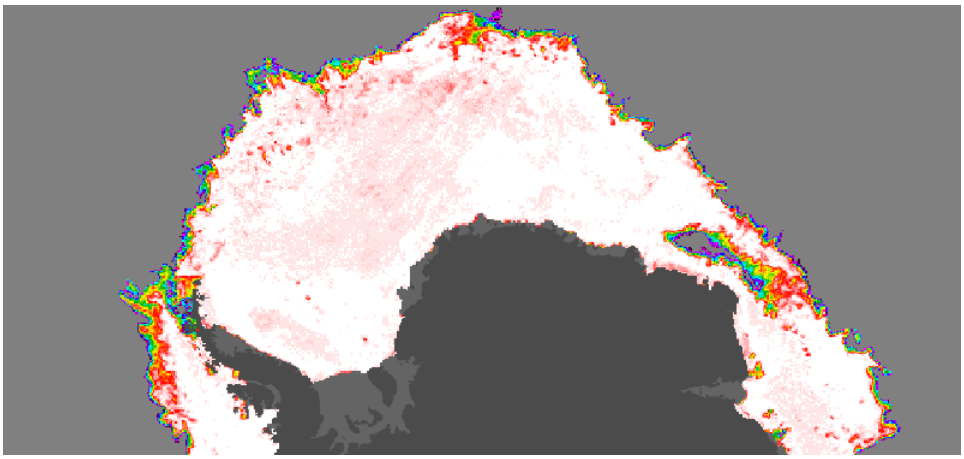

Figure 4.14: Snapshot of SIC on August 17, 2016 showing the 2016 Cosmonauts Sea polynya at its maximum extent. This image was generated by NASA Worldview online data visualization tool (https://worldview.earthdata.nasa.gov) using data collected by the ASMR-E/ASMR2 satellite.

The key takeaway from the previous section is that near-instantaneous poleward wind anomalies were not the sole driver of the record low sea ice extent in late 2016. This is especially the case for the eastern Weddell and Cosmonauts Seas, where our predicted SIC anomalies do not capture any of the observed ice loss. This discrepancy is likely related to

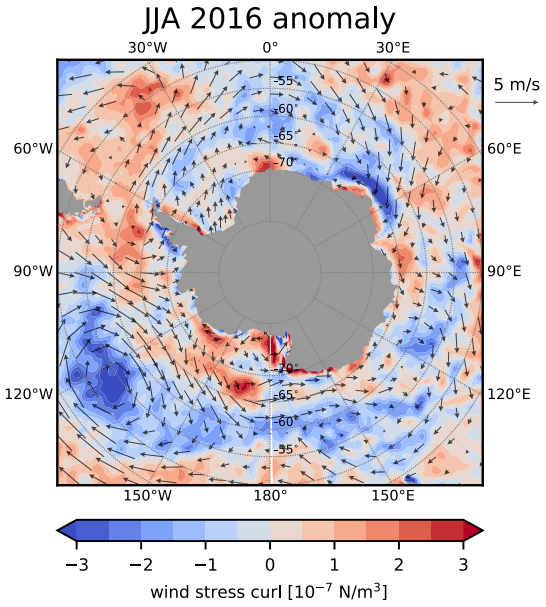

Figure 4.15: Seasonal wind stress curl anomalies (shading) and surface wind anomalies (arrows) for June–August 2016. This is shown to highlight the local wind stress curl anomalous that were present in the lead up to the Cosmonauts Sea polynya event (Figure 4.14). Wind stress curl anomalies were computed from the instantaneous turbulent surface stress obtained from ERA-interim. As before, seasonal anomalies are computed relative to the 1979–2015 base period.

the rare appearance of offshore winter polynyas in those regions. The first of these polynyas opened near Maud Rise in the Weddell Sea in late July and lasted approximately two weeks (Cheon and Gordon, 2019). At its peak extent, this polynya was the largest of its kind since the mid-1970s (Swart et al., 2018). A second and largely undocumented polynya appeared in the Cosmonauts Sea in late August (Figure 4.14). This second event lasted for another two weeks before closing completely in early September. The factors that contributed to this event are still being investigated, but analysis of Argo floats profile data near Maud Rise suggests that anomalous upwelling in early 2016 may have led to the appearance of the Maud Rise polynya (Campbell et al., 2019). Furthermore, analysis of meteorological conditions also reveals that this rare opening of the winter ice pack coincided with the passage of powerful winter storms. Similar conditions may have helped to initiate the Cosmonauts Sea polynya as intense negative wind stress curl anomalies that were also apparent in that location (Figure 4.15). Since these polynyas occurred in late winter, it is possible that the thickness of the overlying ice field did not fully recover prior to the subsequent spring retreat. Hence, we speculate that these late winter offshore polynyas contributed to the springtime

SIE anomalies that occurred in their vicinity. However, it is stressed that these events are directly linked to anomalous meteorological conditions in 2016. The extent to which long-term upwelling contributed to these events remains unclear.

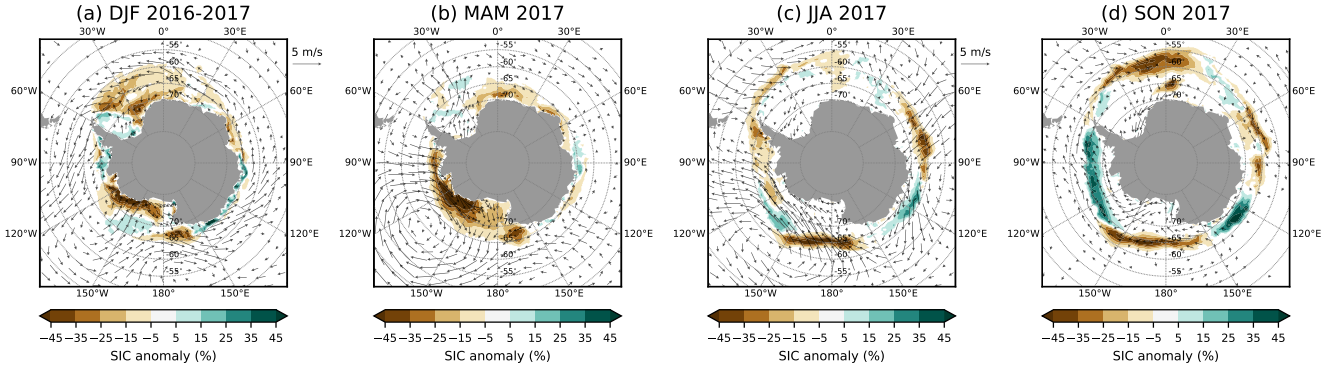

Figure 4.16: Maps showing mean Antarctic sea ice concentration (shading) and 10 m wind anomalies (arrows) for (a) December 2016–February 2017, (b) March–May 2017, (c) June–August 2017, and (d) September–November 2017. Monthly anomalies are computed relative to a climatology computed from the 1979–2015 period.

By the end of 2017, total SIE in the Pacific and Indian Ocean sectors had mostly returned to normal (Figure 4.16 d). However, the deep losses in sea ice area that persisted in the Weddell Sea kept total Antarctic SIE near record low levels. The late 2017 sea ice anomalies coincided with the recurrence of another winter polynya in the Weddell Sea. This polynya appeared in early September and, similar to the 2016 event, was likely initiated by the passage of a powerful storm (Francis et al., 2019; Jena et al., 2019; Campbell et al., 2019). The polynya rapidly grew and eventually superseded the 2016 winter polynya as the largest since 1976. The polynya lasted the entire winter and eventually coalesced with the seasonal ice edge retreat the following spring. Analysis of in situ ocean data reveals that deep convection occurred near Maud Rise during the 2016 winter polynya (Campbell et al., 2019). This resulted in an upward flux of salty deep water that further weakened the local halocline of the entire Maud Rise region. It is therefore hypothesized that the deep mixing that occurred

during this first polynya preconditioned the region for a second winter polynya in 2017.

4.3.5 Summary and discussion

We have found that SIC anomalies have a clear linear dependence on surface wind anomalies on seasonal timescales. This linear dependence is most apparent between SIC and meridonial wind anomalies along the sea ice edge, during winter and spring. The covariance between these two variables improves when surface wind anomalies are lagged by one month, but gets worse for longer time offsets. Using this empirically derived linear dependence, we show that near-instantaneous meridional wind anomalies largely explain the SIC anomalies that occurred in the winter of 2016. However, the same is not true for the subsequent spring season, when total Antarctic SIE reached a record low. For this period, wind anomalies partially explain the pattern of SIC anomalies but fail to account for the amplitude of these anomalies. This discrepancy is largest in the Atlantic and Indian sectors, between 30°–80°E. These results suggest that poleward wind anomalies, though clearly impactful, were not the sole drivers of the record low SIE in late 2016. Furthermore, the similarities between the winter and spring SIC anomalies of that year suggests that the spring wind anomalies acted on on a sea ice field that was already preconditioned for a rapid spring retreat. This conclusion reinforces the initial assessment made by Schlosser et al. (2018), who emphasized the unusual persistence of meridonial wind anomalies in the Pacific and Atlantic sectors throughout 2016.

Our regression analysis also suggests that other factors, besides poleward surface wind anomalies, were responsible for the late 2016 SIC anomalies that appeared in the Weddell and Cosmonaut Seas. Prior to the SIE minimum that occurred in the spring of 2016, these regions featured rare offshore winter polynyas in 2016. Observations suggest that these polynyas were preconditioned by strong upwelling in early 2016 that were then triggered by the passage of powerful storms (Campbell et al., 2019). Once formed, these polynyas were sustained by ocean convection that brought warm, salty deep water to the surface. The appearance of these polynyas in the Weddell Sea are consistent with the observational

and modeling analysis presented in Chapters 1 and 2, which examines the exceptionally strong thermodynamical coupling between winter ice growth and upper ocean ventilation in the Weddell Sea. Thus, it would appear that the sea ice loss that occurred in the eastern Weddell and Cosmonaut Seas was driven by a set of mechanisms that are distinct from those that caused ice loss in the other sectors.

The analysis presented here does not negate the possibility that other factors may have contributed to the rapid ice retreat in late 2016. In particular, our results do not directly contradict the assertion made by Meehl et al. (2019) that the decadal trend in upwelling favorable winds had a substantial impact on this event. Addressing this hypothesis is hindered by the relatively short and sparse record of upper ocean observations in the sea ice zone. That said, it remains unclear how a presumably slow, decadal trend could contribute to such an abrupt event. Further, the assertion that this wind stress curl trend led to strong warm water upwelling has not been clearly demonstrated and would require a thorough analysis of the under-ice ocean data.

Future work should involve deeper exploration of the relationship between surface wind and SIC anomalies on various timescales. Our analysis shows that the coupling between wind and SIC anomalies varies greatly by season and region. A worthwhile exercise would be to characterize this coupling for various time lags and temporal smoothing. Doing so would help to uncover the relative importance of wind-driven SIC variations across the sea ice zone. Still, the ultimate goal is to construct a seasonal sea ice volume budget for the Antarctic region. While doing so is not feasible with current observations, such a budget could be constructed from GCM output. Thus, the observational analysis presented here should be re-examined using suitable simulations of Antarctic sea ice.

4.4 *The 2016–2017 Southern Ocean warming: A mixed layer heat budget analysis*

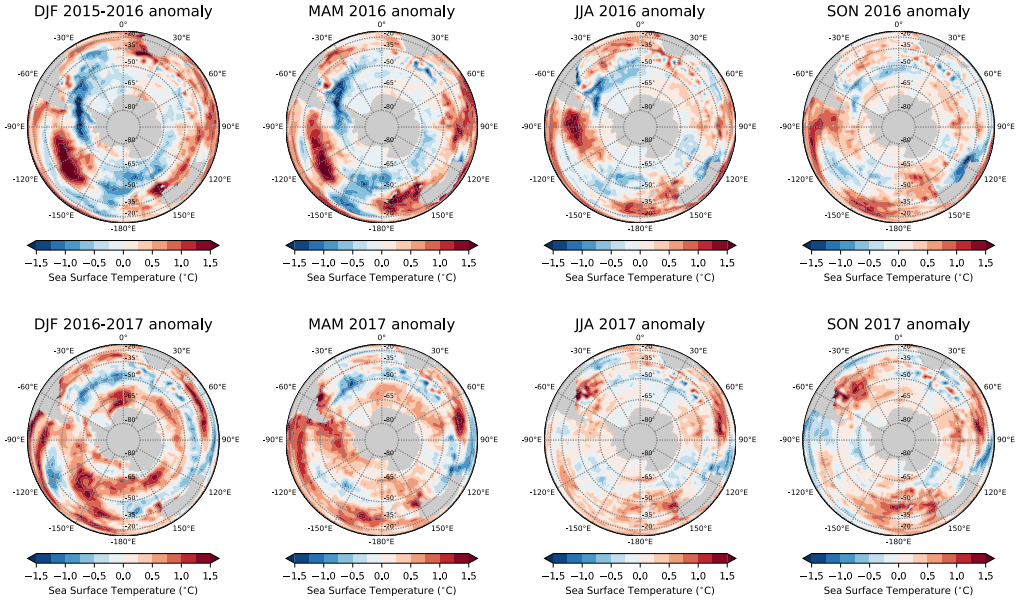

Figure 4.17: Maps showing seasonal SST anomalies across the Southern Ocean in 2016 (top row) and 2017 (bottom row). SST data is sourced from the NOAA Optimum Interpolation SST V2 dataset. Seasonal anomalies were computed relative to a 1982–2015 climatology.

This section focuses on the near-record surface warming that accompanied the record low Antarctic SIE anomalies in 2016. This warming began in early 2016 and culminated in the 2016–2017 austral summer, with near-record high SSTs occurring across all ocean sectors south of 50°S (Figure 4.17). Here, we examine the local factors that led to these SST anomalies. External influences such as that of 2015–2016 El Niño event will be discussed in the following section. As in the previous section, we aim to quantify the processes that led to these anomalies and assess the extent to which these events can be explained by local, contemporaneous mechanisms. To accomplish this, we present a circumpolar-averaged, seasonal mixed layer heat budget for the Southern Ocean. This budget is constructed from in situ and remote observations, with the aid of a 1D mixed layer model. Unlike previous

sections, attention is restricted to the zonally unbounded latitudes of the Southern Ocean, which is largely ice free. To this end, we establish our heat budget for the annular region bounded by 50°S and 65°S, which mostly encapsulates the anomalous warming maximum that occurred in early 2017. In setting the southern boundary at 65°S, we inevitably exclude areas that experienced anomalous sea ice losses in late 2016. However, this is cutoff is motivated by the availability of year-round upper ocean data, which unfortunately is still lacking south of this latitude.

The analysis presented here closely follows the methodology of Dong et al. (2007), who provide the first observationally based seasonal mixed layer heat budget for the Southern Ocean. This was done using Argo float data from the 2002–2006 period. Since then, there has a been a tremendous increase in the availability of ocean data in the Southern Ocean. Thus, the heat budget analysis that is presented here may be viewed as an update to and perhaps a validation of the budget presented by Dong et al. (2007).

4.4.1 Processes that control mixed layer temperature in the Southern Ocean

The temperature of the mixed layer, T_m, is determined by a heat balance that is controlled by air-sea heat fluxes at the ocean surface, lateral advection or mixing, and vertical exchanges across the base of the mixed layer. This heat balance is given by

$$\frac{\partial T_m}{\partial t} = \frac{Q_{net}}{\rho_0 \, c_w \, h_m} - u_m \cdot \nabla T_m - w \, \frac{\partial T}{\partial z}, \tag{4.2}$$

where Q_{net} is the air-sea heat flux into the mixed layer, h_m is the thickness of the mixed layer, u_m is the horizontal velocity of the mixed layer, ∇T_m is the associated horizontal temperature gradient, w is the sum of the vertical velocities associated with entrainment (w_{ent}) and Ekman upwelling (w_{ek}) , and $\partial T/\partial z$ is the vertical temperature gradient at the base of the mixed layer. As in previous chapters, $\rho_0 = 1025$ kg m^{-3} and $c_w = 4180$ J kg^{-1} K^{-1} represent the reference density and specific heat capacity of seawater, respectively. Q_{net} is comprised of contributions from radiative heat fluxes, due to shortwave and longwave radiation, and turbulent heat fluxes associated with sensible and latent heat transfer. Q_{net} also accounts

for the fraction of absorbed shortwave radiation, $Q(-h_m)$, that is transmitted through the mixed layer. Following Dong et al. (2007) the downward transmission of shortwave radiation in the ocean is modeled as an exponential decay through moderately clear water, as defined by Jerlov (1968). The e-folding scale of shortwave decay through perfectly clear water is less than 20 m. Since this depth is much shallower than typical mixed layer depths observed in the Southern Ocean, the shortwave transmission through the mixed layer has a relatively small impact on the variation of T_m.

The second term on the right of (4.2) accounts for the lateral advection of heat, which is comprised of the zonal and meridional components of Ekman and geostrophic transport. Since temperature gradients in the Southern Ocean are primarily meridional, zonal advection results in a relatively small net heating across the Southern Ocean (Dong et al., 2007). Further, since geostrophic currents are dominated by the near-zonal Antarctic Circumpolar Current (ACC), meridional advection is primarily driven by Ekman transport. The meridional component of the Ekman velocity, v_{ek}, is related to surface wind stress by

$$v_{ek} = \frac{\tau_x}{\rho_0 \, f \, h_{ek}}, \tag{4.3}$$

where τ_x is the zonal component of the surface wind stress, f is the Coriolis parameter, and h_{ek} is the Ekman depth. Knowledge of the Ekman depth is limited by the sparse availability of upper ocean velocity measurements in the Southern Ocean. However, recent observational and theoretical work suggests that the Ekman layer (i.e. the depth over which Ekman currents decay by one e-folding scale) ranges between 30–50 m in the Southern Ocean (Lenn and Chereskin, 2009; Elipot and Gille, 2009). This depth layer is generally shallower than the Southern Ocean mixed layer depth (MLD), which ranges from approximately 50 m in the summer to hundreds of meters in the winter (de Boyer Montégut, 2004; Holte and Talley, 2009). Here, our primary concern is the change in T_m that results from the advection caused by Ekman transport. This temperature tendency is modulated by h_m, which will reduce the sensitivity of T_m to surface intensified advection in cases where $h_m > h_{ek}$. More specifically, if the temperature change of the Ekman layer due to Ekman advection is given

by

$$\frac{\partial T_{ek}}{\partial t} = v_{ek}\frac{\partial T_m}{\partial y}, \tag{4.4}$$

the corresponding temperature tendency for the deeper underlying mixed layer is given by

$$\left.\frac{\partial T_m}{\partial t}\right|_{ek} = \frac{h_{ek}}{h_m}\frac{\partial T_{ek}}{\partial t} = \frac{\tau_x}{\rho_0\, f\, h_m}\,\frac{\partial T_m}{\partial y}, \tag{4.5}$$

where the term on the left represents the change in mixed layer temperature due to meridional Ekman transport. The expression on the right of (4.5) can be alternatively obtained by substituting h_{ek} for h_m in (4.3).

The final term in (4.2) gives the mixed layer heat tendency due to vertical mixing or advection across the base of the mixed layer. Entrainment occurs when h_m increases due to wind-driven mixing or convection associated with surface buoyancy loss. Ekman upwelling results when there is net divergence in the near-surface, horizontal Ekman currents and is proportional to the curl of the surface wind stress. During fall and winter, when there is intense surface cooling, the Southern Ocean mixed layer deepens at rates that range from tens of meters to hundreds of meters per month (Dong et al., 2008; Holte and Talley, 2009). On the other hand, upwelling rates are typically on the order of a few meters per month (Carranza and Gille, 2015). Therefore, w_{ent} is generally much greater than w_{ek} during fall and winter. In spring and summer, when the mixed layer is relatively shallow, the intense winds of the Southern Ocean still drive intermittent episodes of rapid entrainment that will overwhelm the heat fluxes associated with large-scale upwelling. For these reasons, we neglect the heat flux associated with Ekman upwelling from our seasonal mixed layer heat budget. This simplification of course does not negate the important role of upwelling on longer timescales, which is a central aspect of the Southern Ocean overturning circulation (Speer et al., 2000; Marshall and Speer, 2012; Armour et al., 2016).

With these approximations our seasonal mixed layer heat budget is reduced to

$$\frac{\partial T_m}{\partial t} \approx \frac{Q_{net}}{\rho_0\, c_w\, h_m} - \frac{\tau_x}{\rho_0\, f\, h_m}\,\frac{\partial T_m}{\partial y} - w_{ent}\,\frac{\partial T}{\partial z}, \tag{4.6}$$

which is further simplified to read

$$dT_m = dT_{ao} + dT_{adv} + dT_{ent}. \tag{4.7}$$

The above heat budget is similar to the one used by Dong et al. (2007). However, we do not account for the horizontal stirring effect of mesoscale eddies, which they quantify as $\kappa \nabla T_m$, where κ is an eddy diffusivity that grossly captures the tendency of mesoscales to smooth horizontal temperature gradients. Dong et al. (2007) found the contribution of this term to be negligibly small in their circumpolar-averaged heat budget. This is expected since the impact of mesoscale eddies is limited to relatively small scales on seasonal timescales. As before, this does not discount the importance of eddies on longer timescales, which play a key role in setting the residual overturning of the Southern Ocean (Marshall and Speer, 2012).

4.4.2 Data and methods

To evaluate (4.6), we use a combination of in situ and remotely-sensed ocean observations. SST variability is derived from the NOAA Optimum Interpolation (OI) SST (V2) dataset, which is a synthesis of satellite-based and in situ SST observations since 1981 (Reynolds et al., 2002). This dataset offers a near-global coverage of SST on a 1° latitude by 1° longitude global grid. Since we are primarily interested in seasonal variability, we use the monthly-averaged version of this dataset. The NOAA OI SST dataset is also used to compute the meridional temperature gradients that are required for determining the Ekman heat flux. Air-sea heat and momentum fluxes are obtained from ERA-interim atmospheric reanalysis (Dee et al., 2011), which is described in the previous section. For the air-sea heat flux calculation, we use monthly mean estimates of net shortwave and longwave radiation, and turbulent sensible and latent heat fluxes. To compute zonal wind stress, we use the monthly mean estimates of instantaneous eastward surface wind stress. As will be discussed further, we also retrieved six-hourly surface momentum, freshwater, and heat fluxes to simulate the effect of entrainment on sub-monthly timescales.

A key insight from Dong et al. (2007) is that the Southern Ocean seasonal mixed layer

heat budget is critically dependent on accurate estimates of h_m. The quantity h_m appears in the denominators of the air-sea and advective heat flux terms in (4.6) and is implicitly included in the entrainment term, where w_e is derived from the time rate of change of MLD. Though it is tempting to compute h_m from a gridded upper ocean temperature and salinity product (e.g. Roemmich and Gilson, 2009), doing so would result in significant errors due to the spatial averaging that is often employed to create these datasets. In particular, spatial averaging will tend to smooth the vertical gradients just below the base of the mixed layer. This tendency is especially high in the Southern Ocean, where there are features sharp horizontal gradients in near-surface properties. We therefore estimate h_m from individually observed ocean profiles *before* applying any spatial averaging or interpolation. This is done using upper ocean temperature and salinity measurements from Argo profiling floats.

Argo floats collect profiles of temperature and salinity for the upper 2000 m of the ocean, on approximately 10 day intervals, with accuracies of 0.001 °C and 0.01 psu, respectively (Roemmich et al., 2004; Riser et al., 2016). Float profile data were acquired from the February 2019 snapshot of the Argo Global Data Assembly Centre (GDAC) database (Argo, 2019). We use the "adjusted" CTD profiles, which have been modified to eliminate known biases, and retain profiles that contain measurements flagged as data of "good" or "acceptable" quality (QC flags 1, 2, 5, and 8). These include profiles collected by floats that sample under sea ice. Since these floats generally do not surface in the winter, we approximate their trajectories via linear interpolation. Given that we are primarily concerned with basin-scale warming patterns, the spatial errors associated by this linear approximation has negligible impact on our analysis. Each selected profile is linearly interpolated to a common vertical coordinate that has a vertical spacing of 0.5 m.

Following Dong et al. (2007), we define the mixed layer as the layer over which potential density increases by 0.03 kg/m^3 relative to that at the surface. Since the shallowest measurement of each profile can vary between 2–10 m, we use the density at 10 m as our "surface" reference point for consistency. In addition to computing the MLD, we also calculated the mixed layer temperature (MLT) and the sub-mixed-layer gradient for each profile. The latter

was determined from the temperature difference between the mixed layer and 10 m below the mixed layer. These mixed layer properties were then averaged within 2° longitude by 1° latitude bins for each month.

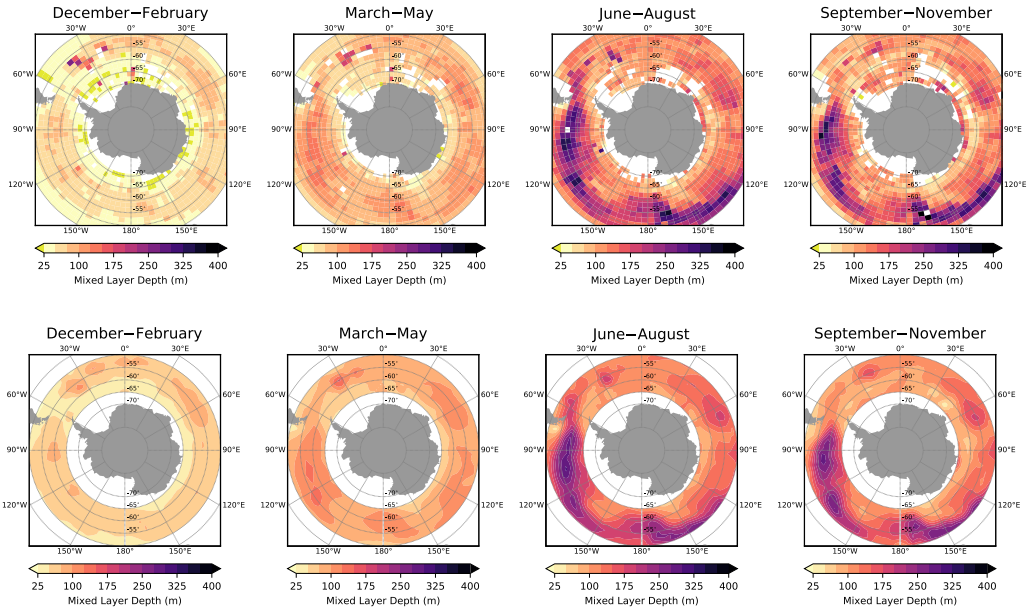

Figure 4.18: Seasonal mean MLD computed from individual Argo profiles. The top row shows the seasonal MLD depth, averaged over the 2006–2018, obtained from simple bin averaging. The bottom row shows the same data spatially interpolated using the loess method.

These monthly, bin-averaged MLD estimates were then spatially interpolated to the same grid as the surface flux data from ERA-interim. This was done using a locally weighted regression, otherwise known as a loess filter (Cleveland and Devlin, 1988), which has been previously used to spatially interpolate mixed layer properties in the Southern Ocean (e.g. Sallée et al., 2010). The result of this spatial interpolation is demonstrated in Figure 4.18, which shows the seasonal variation in MLD compares bin-averaged MLD estimates with the spatially-interpolated version obtained using the loess method.

Though the above procedure provides accurate estimates of the Southern Ocean MLD on monthly timescales, these estimates are not sufficient for determining the vertical velocity

needed to compute the entrainment heat flux. This is because mixed layer entrainment is driven by processes that occur on much shorter timescales. Of particular importance in the Southern Ocean is the mixing generated by storms, which can drive intense episodes of entrainment on sub-daily timescales (Carranza and Gille, 2015). Since Argo floats typically profile the upper ocean every 10 days, an individual float is unable to resolve this high frequency variability. Moreover, these floats do not have the spatial density to capture such variations over any given area. Therefore, vertical entrainment needs to be inferred from some other method. Dong et al. (2007) tackled this problem by using a modified version of the 1D Kraus-Turner model, which predicts MLD from a turbulent kinetic energy balance. These simulations were initialized with observed profiles and forced with six-hourly surface buoyancy and momentum fluxes from an atmospheric reanalysis. We adopt a similar approach but use the modified version of the Price-Weller-Pinkel (PWP) mixed layer model (Price et al., 1986), which is described in Chapter 3.

Given that there are tens of thousands of float profiles and running the PWP model is somewhat computationally intensive, we adopt an approach that uses a subset of the Argo but still manages to capture the large-scale variation in mixed layer entrainment across the Southern Ocean. First, Southern Ocean profiles were subdivided into relatively coarse 15° longitude by 5° latitude bins. Within each spatial bin, a maximum of 5 profiles were randomly chosen to initialize a simulation. Next, using only profiles collected between December 15 and January 15, each simulation was configured to run for a whole calendar year. This was done using 6-hourly surface heat, freshwater, and momentum fluxes from ERA-interim reanalysis. These forcing data were extracted from the grid point closest to each profile's location. Finally, the mean entrainment heat flux for each month was computed for each spatial bin. This entrainment heat flux was determined during each simulation using the difference in MLT before and after the vertical mixing schemes were employed. For years where five float profiles were found for each 15° longitude by 5° latitude spatial bin, a total of 360 individual simulations were conducted. However, in many cases, fewer than 5 floats were found to initialize the model within each spatial bin.

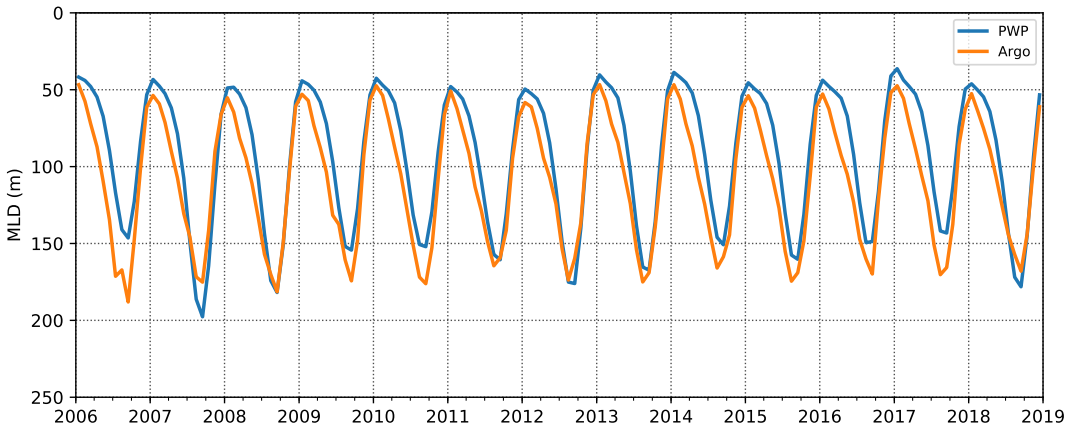

Figure 4.19: Comparison of zonally averaged MLD from direct observations with the MLD simulated by the PWP model. Model runs were reinitialized at the start of each year using float profiles collected between December 15 and January 15. More details are provided in the text.

Despite being initialized by only summertime observations, the PWP model produced seasonal variations in MLD that compare favorably to direct observations Figure 4.19. To first order, the model captures the timing and magnitude of the seasonal deepening and shoaling of the Southern Ocean mixed layer. However, the simulated MLDs do have slight discrepancies with the observations. In particular, the simulated mixed layer deepening during the late summer and fall period generally lags the observed deepening by 1–2 months. This systematic bias suggests that these 1D simulations are missing a key physical process. As will be discussed further, this missing process is likely the surface cooling associated with meridional advection. Nevertheless, the overall good correspondence between the simulated and observed MLDs gives us confidence that these simulations provide realistic estimates of high frequency entrainment. Climatological maps of the simulated entrainment heat fluxes are shown in Figure 4.20. These estimates are in good agreement with those computed by Dong et al. (2007) for the 2002–2006 period.

Lastly, to construct a meaningful mixed layer heat budget for the Southern Ocean, it is essential to have an even distribution of data across all sectors. By 2004, Argo floats were

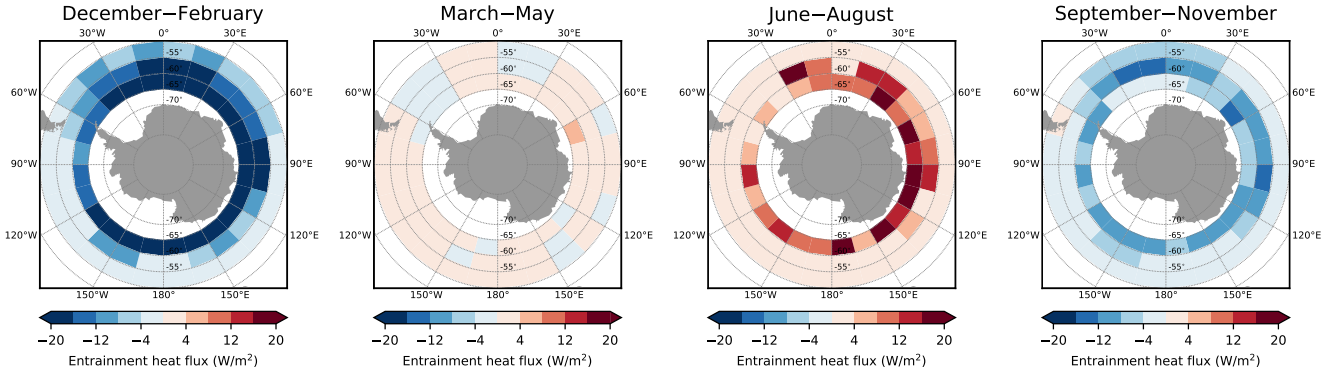

Figure 4.20: Seasonal entrainment heat flux estimated from 6-hourly, year-long runs using the PWP mixed layer model. Positive values represent a warming of the mixed layer. This seasonal mean was computed using estimates generated for 2006–2018.

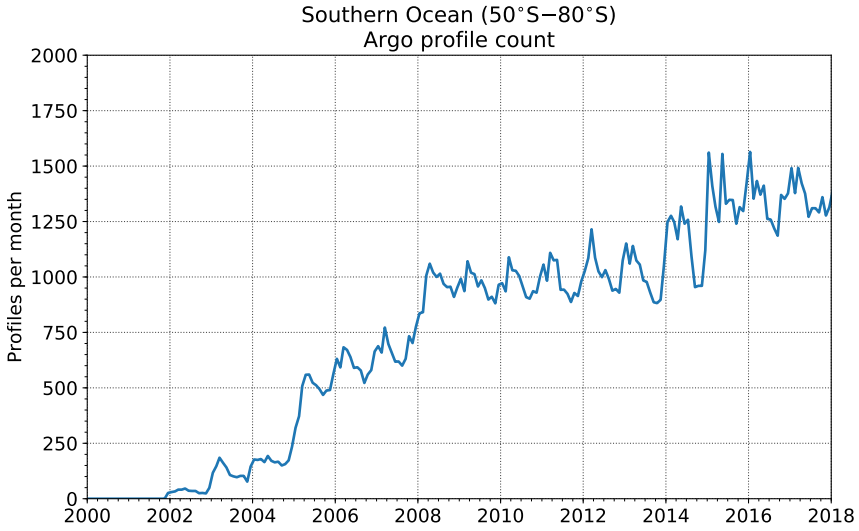

Figure 4.21: Number of Argo profiles collected in the Southern Ocean (50°S–80°S) each month since 2000.

collectively reporting 150–200 upper ocean profiles per month in the Southern Ocean (Figure 4.21). Since then, this sampling frequency has mostly varied between 600–1000 profiles per month since 2008. However, closer inspection of the profile distribution reveals that uniform sampling of the region on monthly timescales was arguably not achieved until 2006 (Figure

4.22). Thus, to minimize biases due to uneven spatial sampling we limit our budget analysis to the 2006–2018 period.

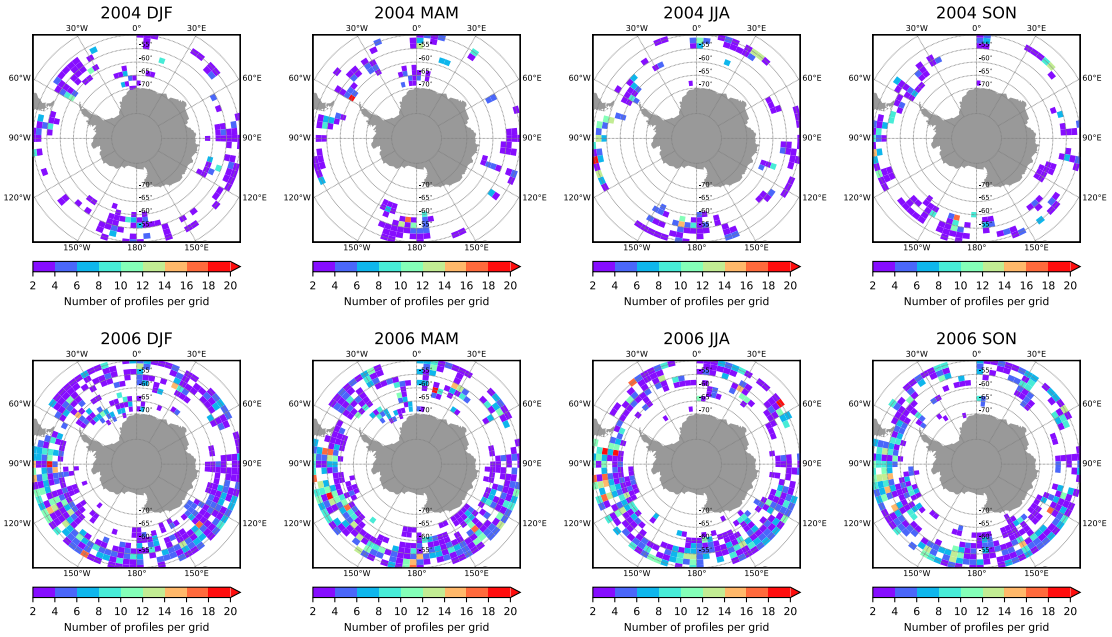

Figure 4.22: Comparison of the seasonal sampling distribution by Argo floats in 2004 (top row) with that of 2006 (bottom row). Each map shows the number of Argo profiles per 2° longitude by 1° latitude bin. To minimize biases due to uneven spatial sampling, we limit our heat budget analysis to the 2006–2018 period.

4.4.3 A seasonal mixed layer budget for the Southern Ocean

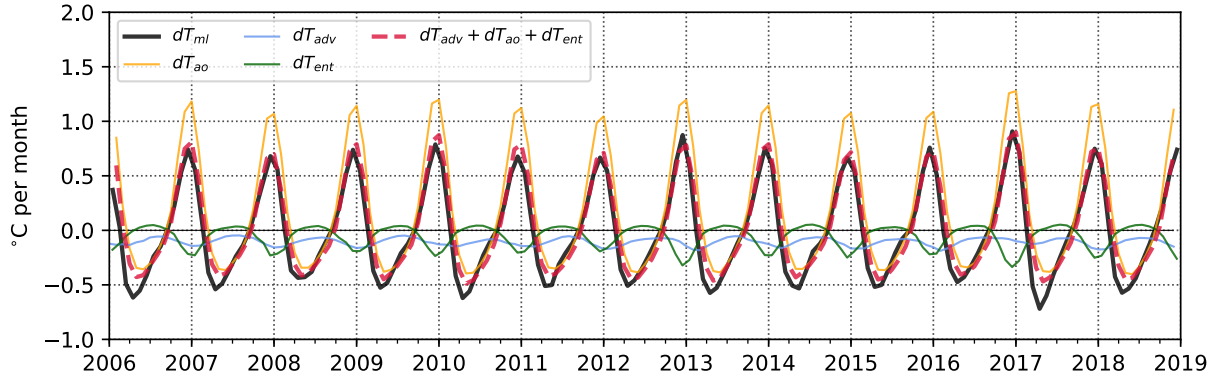

Figure 4.23: Time series of the mixed layer heating terms in (4.7) for 2006–2018. This budget describes the evolution of SST (i.e. dT_m) for the entire Southern Ocean, which is defined as the annular region bounded 50°S and 65°S. The close agreement between dT_m (black line) and the sum of the independently derived heat flux terms (red dashed line) demonstrates that our heat budget is approximately closed on seasonal timescales. All time series have been smoothed with a 3 month running mean.

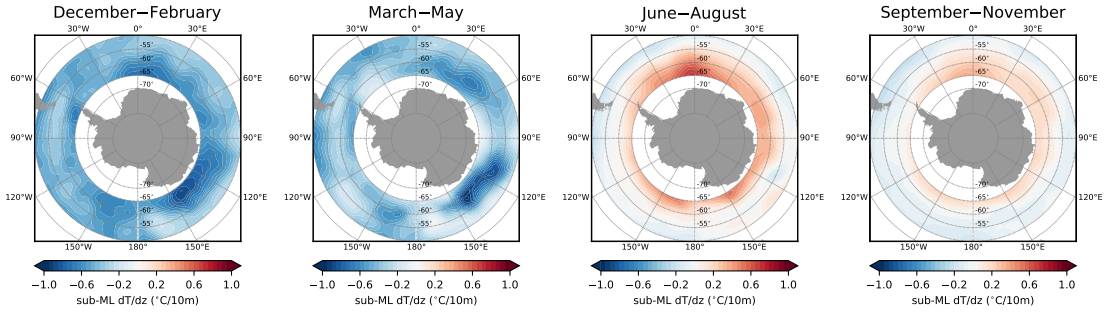

Figure 4.24: Climatology of sub-mixed-layer temperature gradients in the Southern Ocean. Positive values indicate instances where temperature increases with depth. These estimates were obtained from individual Argo float profiles, using the temperature gradient 10 m below the mixed layer. As illustrated in Figure 4.18, values from individual profiles were bin-averaged then smoothed using a loess filter.

Before examining the 2016–2017 SST anomalies, we examine the extent to which our

heat budget closes on seasonal timescales. We find that the sum of the heating terms in (4.7) broadly captures the seasonal cycle of SST variations in the Southern Ocean (Figure 4.23). As expected, air-sea heating is the primary driver of SST variability in the Southern Ocean. Peak atmospheric warming occurs in late December, causing a mixed layer warming of approximately 1°C per month. This is mainly due to the intense solar insolation that occurs during these months (not shown). The summertime atmospheric warming is partially offset by cooling associated with entrainment and meridional advection. These fluxes combine to produce a peak summer time warming of approximately 0.75°C per month. Between December and April, the atmospheric warming flux transitions to a cooling flux. Maximum cooling occurs between April and June, with typical amplitudes reaching −0.5°C per month. This peak cooling tends to be slightly underestimated by the sum of the heat flux terms, with the largest discrepancy occurring in early 2017. As will be discussed further, this discrepancy is likely tied to the MLD biases shown in Figure 4.19. Net cooling generally persists through winter until the beginning of austral spring in November, after which solar insolation rapidly increases to its summer maximum. In the annual mean, the atmosphere provides a net warming to the Southern Ocean mixed layer that is balanced by cooling due to entrainment and meridional advection. Despite the slight discrepancies during late summer and early fall, the seasonal heat budget is approximately closed over most of the year.

These results are in good agreement with the 2002–2006 heat budget analysis presented by Dong et al. (2007). However, we find that entrainment provides a slight warming during the winter, whereas they find a net-zero contribution for this period. This discrepancy is likely due to the limited availability of wintertime data during the 2002–2006. With our more complete data coverage, we observe that the temperature below the mixed layer is generally warmer during the winter (Figure 4.24). This is most apparent within the sea ice zone—a region that was poorly sampled prior to 2004 (Figure 4.22).

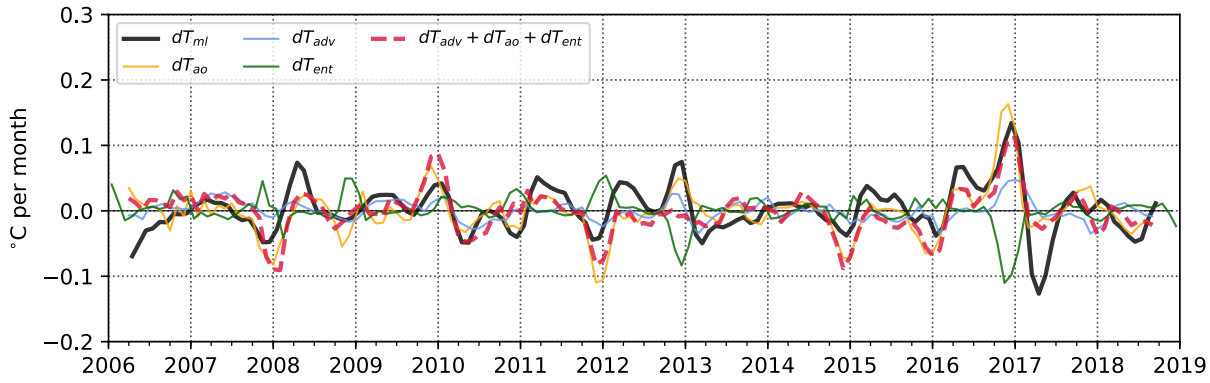

Figure 4.25: Like Fig. 4.23 but showing seasonal heating anomalies, relative to the 2006–2018 climatological mean.

4.4.4 Drivers of the 2016–2017 surface warming event

From Fig. 4.23, it is evident the heat flux terms in (4.6) are able to explain the 2016–2017 heating anomaly. To examine this event in more detail, we compute the seasonal anomalies for each term in our heat budget, relative to their corresponding climatology for the 2006–2018 period. Compared to the full seasonal heat budget, the heat budget for seasonal heating anomalies shows weaker correspondence between variations in SST and the sum of the flux terms (Figure 4.25). This reflects the fact that deviations from the climatological mean are relatively small and likely comparable to the uncertainties in our budget analysis. Nevertheless, anomalies in mixed layer heating are often associated with similar deviations in the heating terms (e.g. the warming event in early 2010 and the cooling event in late 2011). Most notably, the 2016–2017 surface warming is well-captured by corresponding anomalies in the heat flux terms. We observe that the late 2016 warming event was primarily due to anomalous atmospheric heating with secondary warming contributions from anomalous Ekman transport. The additional warming from these sources was partially offset by enhanced cooling due to entrainment. For the remainder of this section, we focus on the months leading up to the warming maximum in late 2016 and early 2017.

Closer examination of the anomalous air-sea heat flux reveals persistent patterns of sur-

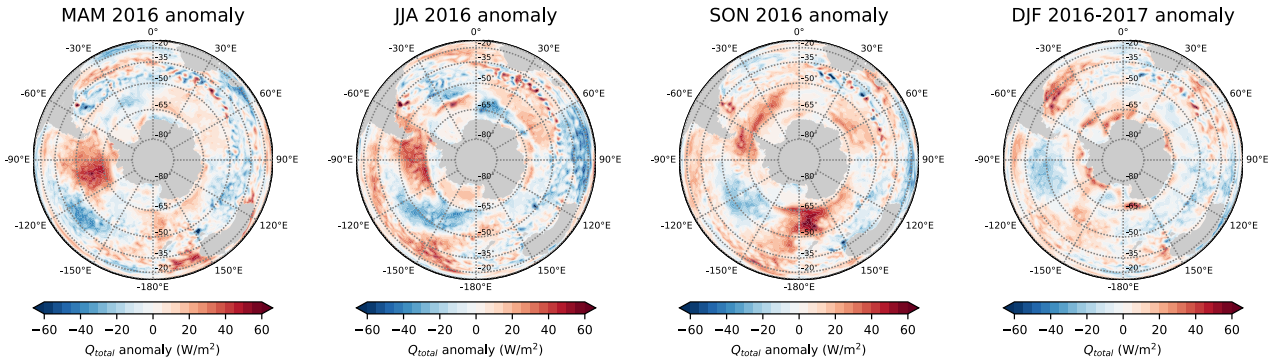

Figure 4.26: Seasonal air-sea heat flux anomalies during March 2016 – February 2017. From left to right: total air-sea heat flux anomaly during March–May 2016, June–August 2016, September–November 2016, and December–February 2017. Positive values represent anomalous heat flux into the ocean. Heat flux estimates are computed from ERA-interim reanalysis.

face warming in 2016 and early 2017 (Figure 4.26). For much of 2016, the southeastern Pacific Ocean experienced a positive air-sea heat flux anomaly (i.e. directed into the ocean) that ranged between 20–50 W/m^2. This heating anomaly was due to anomalies in longwave cooling and turbulent heat loss (Figures 4.27 and 4.28). Therefore, positive anomalies in these terms reflect reductions in ocean heat loss to the atmosphere. The heat flux anomaly in the southeastern Pacific persisted through the winter season before giving way to warming anomalies of similar magnitude in the southwestern Atlantic and southeastern Pacific Oceans in the following spring. These heat flux anomalies were mostly abated by the end of 2016, but substantial positive air-sea heat flux anomalies lingered in the sea ice zone through that subsequent summer. Within the sea ice zone, anomalies in net shortwave radiation were responsible for most of the local warming. This was likely a direct result of the early sea ice retreat that occurred during the spring of 2016.

In addition to the anomalous air-sea heating, there was weaker than normal northward Ekman transport during much of 2016 (Figure 4.29). During the fall and winter of 2016, anomalous meridional Ekman transport contributed 10–20 W/m^2 of ocean heating in the

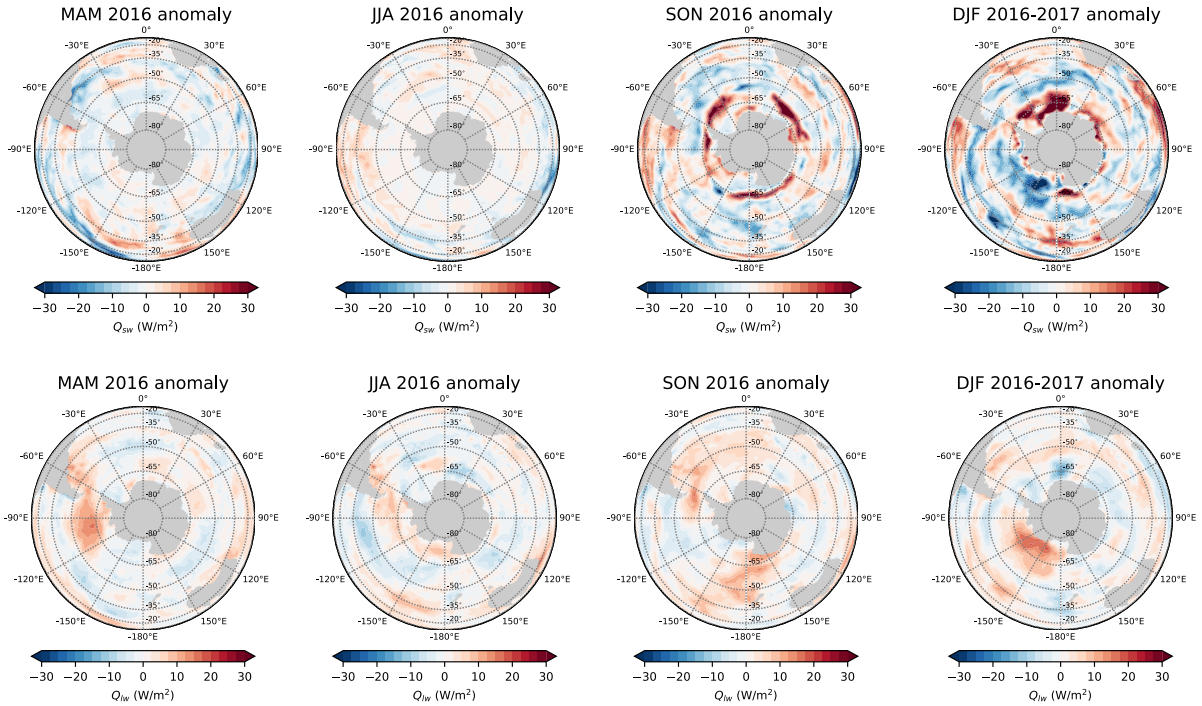

Figure 4.27: As for Figure 4.26 but showing contributions from anomalous shortwave radiation (top row) and longwave radiation (bottom row).

Pacific sector. These anomalies intensified in the spring then expanded across all basins of the Southern Ocean in the subsequent summer. Concurrent with these advective heating anomalies were negative zonal wind anomalies, which represent a weakening of the Southern Ocean westerlies. These zonal wind anomalies were most dramatic during the summer of 2016–2017, when circumpolar westerlies were 2–3 m/s (equivalent 1–1.5 standard deviations) weaker than normal.

The heating anomalies associated with air-sea heat fluxes and Ekman transport were further amplified by shallower than normal MLDs (Figure 4.30). Most notably, the anomalous wintertime air-sea heat fluxes in the southeastern Pacific Ocean (Fig. 4.26) were accompanied by anomalous MLD shoaling in excess of 100 m. This localized shoaling persisted into the spring and was augmented by similar anomalies in the southwestern Pacific. The shoaling anomalies were much smaller during the 2016–2017 summer season, ranging between 5–15 m

in the Pacific and Indian Ocean basins. However, despite being of much smaller amplitudes, these summertime anomalies are significant when compared to the shallower MLDs typical of this season (Fig. 4.18).

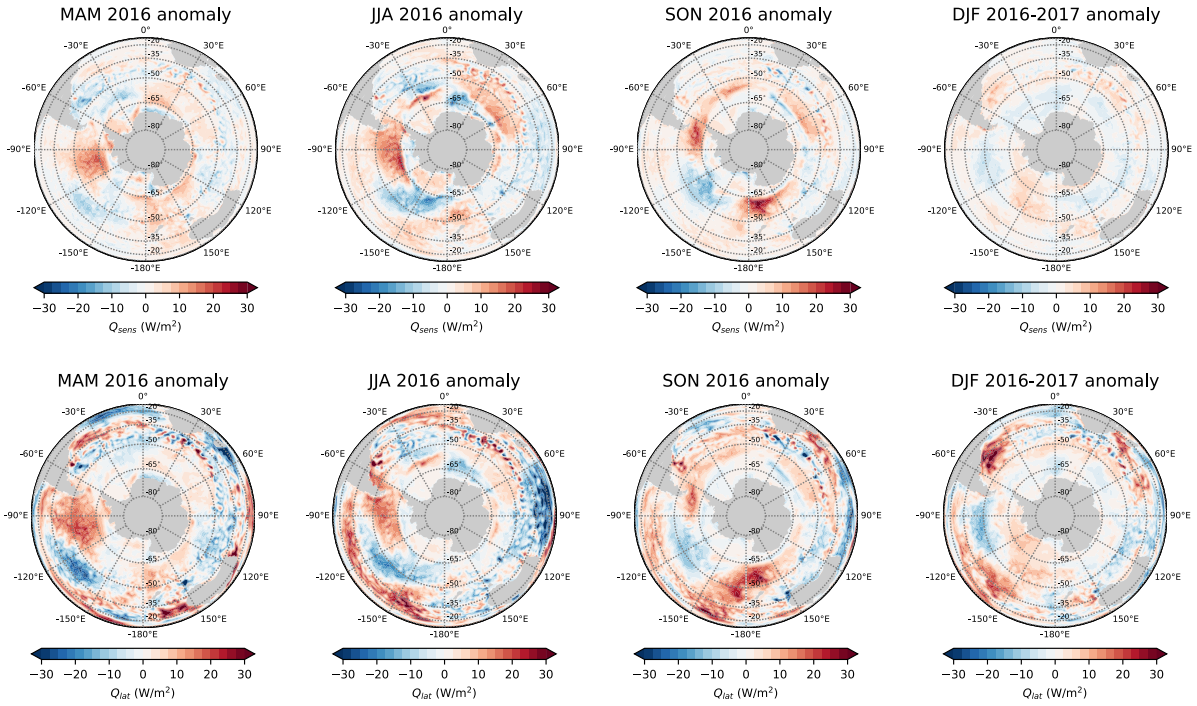

Figure 4.28: As for Figure 4.26 but showing contributions from anomalous sensible heat fluxes (top row) and latent heat fluxes (bottom row).

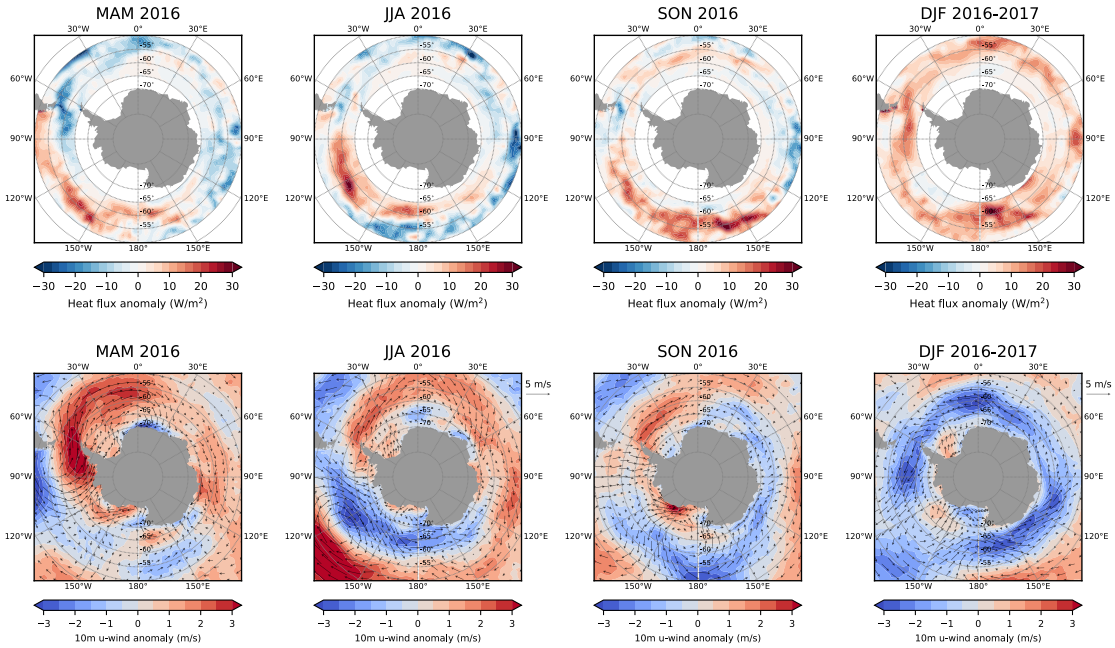

Figure 4.29: Seasonal meridonial heat flux anomalies (top row) and surface wind anomalies (bottom row) during March 2016 – February 2017. The bottom row shows both the surface wind anomaly vectors (arrows) and the amplitude of the zonal wind anomalies (shading).

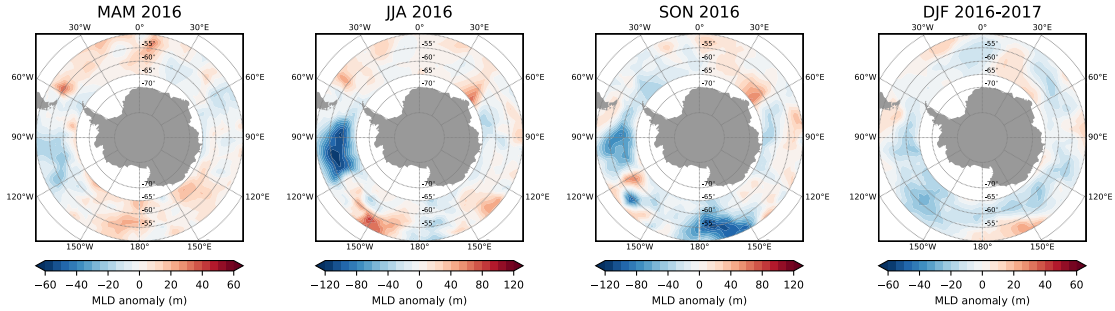

Figure 4.30: Seasonal MLD anomalies during March 2016 – February 2017. These estimates are derived from individual Argo float profiles. Note the different color scales for winter and spring versus summer and fall.

4.4.5 Summary and discussion

In the preceding sections, we present a seasonal mixed layer heat budget for the Southern Ocean using in situ ocean observations and atmospheric reanalysis for the 2006–2018 period. This analysis is a direct extension of the heat budget analysis presented by Dong et al. (2007) for 2002–2006. Like this previous work, we are able to explain most of the observed monthly variations in SST using estimates of the heat fluxes associated with air-sea heat transfer, meridional advection, and vertical entrainment. However, in contrast to the results from Dong et al. (2007), we find that vertical entrainment provides a small positive heating to the Southern Ocean mixed layer during the winter. This discrepancy likely stems from the lack of data near the sea ice zone during the 2002–2006. However, in agreement with Dong et al. (2007), we find that in the annual mean that the atmosphere provides a net surface warming that is balanced by cooling due to northward Ekman transport and vertical entrainment.

One shortcoming of this heat budget analysis is the quantification of entrainment heat fluxes across the Southern Ocean. This process is notoriously difficult to observe and simulate since it is driven by high frequency atmospheric variability and occurs on relatively small scales. Here, an attempt was made to estimate the impact of this process by conducting year-long simulations with the PWP mixed layer model. These simulations were initialized with early summer profiles from Argo floats and forced with 6-hourly buoyancy and momentum fluxes from ERA-interim reanalysis. In general, the simulated MLDs compare favorably with observations. However, the model tended to initiate the late summer–early fall mixed layer deepening 1–2 months later than observed. The timing of this bias coincides with the timing of the largest discrepancies in our seasonal heat budget—most notably in early 2017 following the near-record warming. We speculate that this stems from the fact that these 1D simulations do not account for the cooling caused by northward Ekman transport, which has its largest impact during the summer. By not accounting for this source of cooling, the simulated mixed layer is not able to cool fast enough to initiate the rapid deepening that typically occurs in early fall. One way to address this issue would be to introduce this

advective heat flux as an extra cooling term in the surface forcing. Another possible solution would be to conduct monthly simulations, whereby each run is initialized with observed profiles from the preceding month. These alternative approaches will be explored in future work.

These limitations notwithstanding, our heat budget is able to accurately explain SST variations in the Southern Ocean during winter, spring, and summer. Using this heat budget, we demonstrate that the 2016–2017 warming event was driven by anomalies in air-sea heat transfer and meridional advection that occurred during that period. During late fall and early winter of 2016, the surface ocean heating was mostly caused by a reduction in latent and sensible heat loss to the atmosphere in the Pacific sector. During the subsequent spring and summer months, these heating anomalies were augmented by a reduced northward Ekman transport that was the direct result of a weakening of the Southern Ocean westerlies. Additionally, the lower surface albedo caused by the early sea ice retreat led to enhanced absorption of incoming solar radiation. The warming anomalies were further amplified by an anomalous shoaling of the mixed layer, which persisted in the Pacific sector during most of 2016. The combined impact of anomalous atmospheric heating, reduced northward advection, and shallower than normal MLDs culminated in late 2016 to produce the observed near-record SST in the Southern Ocean.

A key takeaway from this work is that the 2016–2017 Southern Ocean surface warming event can be largely explained by contemporaneous atmospheric anomalies. This suggests that the SST anomalies that occurred during this period were due to transient atmospheric conditions rather than the culmination of a long-term climatic trend. In particular, we find no clear evidence to suggest that decadal trends in upwelling favorable winds were a significant contributor to the abrupt surface warming that occurred during this period. This is evidenced by the fact that the warming anomaly had mostly subsided by the end of 2017 (Figs. 4.3 and 4.17). Furthermore, we note that though this warming was extreme it was not unprecedented. A warming of similar magnitude occurred during the summer of 1982–1983 (Fig. 4.3).

4.5 Conclusion: The unusual synchronization of ENSO, SAM, and IOD

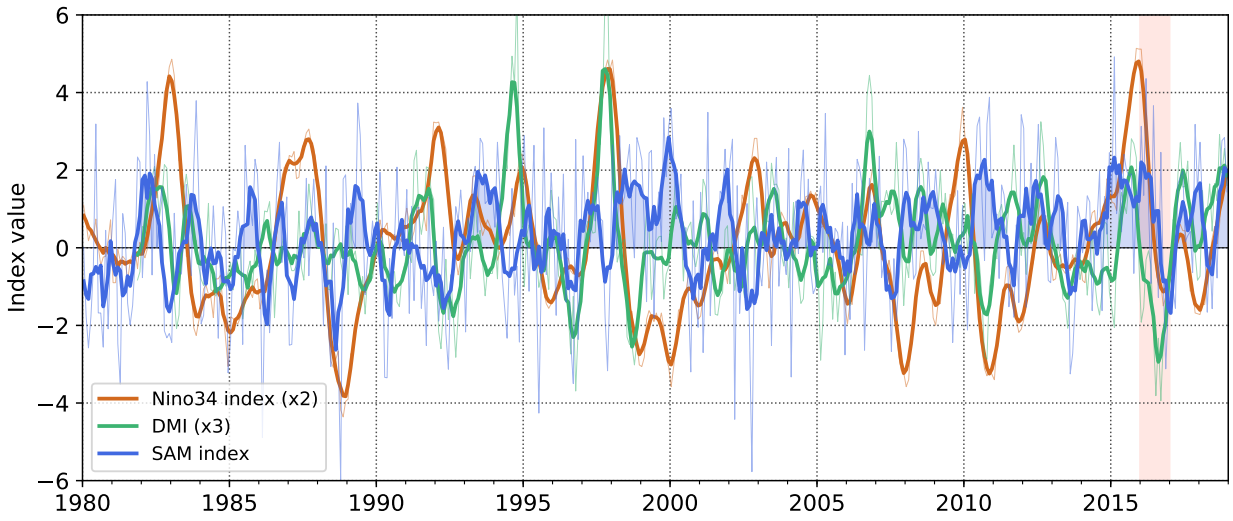

Figure 4.31: Time series of the El Niño Southern Oscillation (ENSO), Southern Annular Mode (SAM), and Indian Ocean Dipole (IOD) since 1980. The SAM index measures the meridional sea surface pressure gradient across the Southern Ocean. Positive SAM signifies a relatively large meridional surface pressure gradient, which corresponds to a strengthening and poleward shift of the circumpolar westerlies. The Dipole Mode Index (DMI) measures the zonal SST gradient across the equatorial Indian Ocean and is used to assess the IOD; negative IOD values signify a strengthening of the climatological eastward SST gradient across. The Nino34 index is based on SST anomalies in the central equatorial Pacific and is used to evaluate the state of ENSO. All thick lines have been smoothed with a 3-month running mean. The Nino34 and DMI values are scaled by factors of 2 and 3, respectively. The year 2016 is highlighted as a visual aid.

In the previous sections, we demonstrate that the 2016–2017 Southern Ocean sea ice loss and surface warming events can largely be explained by concurrent changes in local atmospheric conditions. These atmospheric anomalies are both notable for their amplitudes and persistence. In this section, we briefly discuss these anomalies within the context of large-scale climate variability. The year 2016 began with one of the strongest positive El Niño Southern Oscillation (ENSO) events on record (Figure 4.31). During this time, the southeastern Pacific Ocean experienced a strong surface warming that persisted until the middle of the

winter season. This anomalous surface heating is similar to the warming that has occurred during other El Niño events and was likely facilitated by the formation an "atmospheric bridge" that allows ENSO events to influence extratropical regions (e.g. Li, 2000; Ciasto and England, 2011; Stuecker et al., 2017). During this strong El Niño event, there was a major positive Southern Annular Mode (SAM) event in the Southern Ocean. Positive SAM events are associated with a strengthening and poleward shift of the Southern Ocean westerlies (Marshall, 2003). By the same process, positive SAM is also associated with the deepening of the Amundsen Sea low, which results in the anomalous poleward advection of warm air towards the Antarctic Peninsula and a corresponding enhancement of equatorward surface air flow in the Ross Sea (Stammerjohn et al., 2008; Clem and Fogt, 2013; Turner et al., 2013b). In a recent study, it was found that this positive SAM event also coincided with a deepening of the Weddell Sea low, which favored stronger Ekman pumping (Campbell et al., 2019). This study further proposed that anomalous upwelling weakened the upper ocean stratification in the Weddell Sea and preconditioned the region for the rare offshore winter polynyas that appeared that year. The relationship between these SAM and ENSO events remain unclear. However, we note that this was the first concurrence of positive ENSO and positive SAM since at least 1981 (Figure 4.31).

During the first half of 2016, both ENSO and SAM gradually returned to their neutral states. During this time, the Indian Ocean Dipole (IOD) shifted to a strongly negative state (Fig. 4.31). The IOD describes the state of the zonal SST temperature gradient across the tropical Indian Ocean. Much like ENSO in the tropical Pacific Ocean, variations in zonal SST gradient in the Indian Ocean are associated with the large scale changes in atmospheric circulation (Saji et al., 1999; Ashok et al., 2001; Saji and Yamagata, 2003). In particular, the negative phase of the IOD is associated with enhanced surface warming and precipitation in the eastern Indian Ocean near Sumatra (Webster et al., 1999; Shinoda and Han, 2005; Wilson et al., 2013). The anomalous precipitation associated with the 2016 negative IOD event triggered an atmospheric Rossby wave train that emanated into the Southern Ocean and established anomalous poleward air flow across the Antarctic sea ice

zone during austral spring (Wang et al., 2019; Meehl et al., 2019). As was demonstrated previously, these springtime surface wind anomalies augmented the poleward surface wind anomalies that were already present during the winter. Similar to the ENSO event that preceded it, this negative IOD event was one of the strongest on record.

The year 2016 ended with SAM shifting to a strongly negative state and coincided with a uniform weakening of the circumpolar westerlies (Fig. 4.29). This transition to negative SAM began during austral spring of 2016, as the previous IOD event abated, and peaked in the following summer. Wang et al. (2019) proposed that this negative SAM event was initiated by an anomalous weakening of the polar stratospheric vortex over Antarctica. However, the mechanism that initiated this stratospheric change is unclear. More importantly, El Niño events in austral summer are typically followed by positive SAM events during the subsequent austral spring (Stuecker et al., 2017). Since positive SAM events are associated with enhanced northward Ekman transport (L'Heureux and Thompson, 2006; Stammerjohn et al., 2008), the appearance of negative SAM in late 2016 delayed the surface cooling in the Southern Ocean that typically follows positive ENSO events. Furthermore, the surface heating that occurred during the preceding El Niño and negative IOD events coincided with an anomalous shoaling of the Southern Ocean mixed layer (Fig 4.30). As discussed previously, these shallower than normal MLDs and weak northward Ekman transport combined to produce the near-record Southern Ocean warming that occurred in early 2017.

By mid 2017, Southern Ocean SSTs had returned to normal conditions and SAM, IOD, and ENSO were all in relatively neutral states (Figs 4.31). However, Antarctic SIE remained anomalously low for much of 2017, with large negative anomalies persisting through the winter and spring of that year. The 2017 sea ice anomalies coincided with the rare appearance of a large offshore winter polynya in the Weddell Sea (Fig. 4.16). This polynya occurred in the same location as the 2016 Maud Rise polynya, but eventually grew to nearly twice the size of the 2016 event. As discussed previously, the recurrence of the Maud Rise polynya in 2017 was in part preconditioned by the deep mixing that occurred during the previous winter polynya. Thus, the 2017 winter polynya event is indirectly linked to the strong upwelling that

occurred during the early 2016 positive SAM event. Furthermore, Campbell et al. (2019) found that similar sequences of Weddell Sea polynya events have followed other positive SAM events in the past.

In conclusion, the 2016–2017 Southern Ocean SIE and SST anomalies are directly linked to well-known sources of climate variability. From this correspondence, one could conclude that these events were due to a serendipitous synchronization of natural variability. However, we cannot rule out the possibility that anthropogenic changes may have contributed to the observed deviations in SAM, IOD, and ENSO. Furthermore, with limited ocean data in the Antarctic sea ice zone, it is difficult to quantify the impact of the underlying trends associated with the climatological strengthening of circumpolar westerlies in the Southern Ocean. In either case, these events underscore the tremendous challenge we face in making accurate long-term climate projections for the Southern Ocean. In particular, the 2016–2017 events illustrate that future changes in the Antarctic region will not just depend on local processes but also remote variability and trends in regions like the tropical Indian and Pacific Oceans. Since SAM, IOD, and ENSO exhibit variability on interannual to decadal timescales, it is likely that the full extent of their interactions has not been captured by our relatively short observational record. Thus, even though anthropogenic warming is expected to fully manifest itself in the Southern Ocean over the next century, natural variability may remain the dominant driver of Southern Ocean climate variability for years and possibly decades to come.

Chapter 5
CONCLUSIONS

In this dissertation, different aspects of the Southern Ocean ice-ocean system are explored in detail. Chapters 2 and 3 focus on the thermodynamic coupling between winter sea ice growth and vertical ocean heat fluxes. Chapter 4 examines recent drivers of SST and sea ice cover variability across the Southern Ocean. Each chapter relied heavily on publicly available observations, specifically those made available through the Argo program and Marine mammals Exploring the Ocean Pole-to-pole consortium. Without these observations, this dissertation would not have been possible.

The primary insight from Chapters 2 and 3 is that wintertime ice-ocean feedbacks have important geographic variability across the Southern Ocean. This regionality features a tight coupling between winter ice growth and thermocline ventilation in the Atlantic sector, specifically the Weddell Sea, and a comparatively weak coupling in the Pacific sector. These variations stem from differences in stratification across these basins, with the Atlantic sector having higher surface salinity and much weaker stratification. These regional differences will dictate the response of the entire Antarctic ice-ocean system to future climate change. In particular, our results demonstrate that sea ice growth and deep ocean ventilation in the Weddell Sea have high sensitivity to changes in upper ocean stratification. Thus, accurate projections of the Antarctic ice-ocean system will require faithful representation of these regional ice-ocean interactions.

The key takeaway from Chapter 4 is that the record surface warming and sea ice loss that across the Southern Ocean in 2016 and 2017 were initiated by highly unusual atmospheric and oceanic conditions. These conditions coincided with extreme deviations in tropical and extratropical modes of climate variability—namely, the Southern Annular Mode (SAM), El

Niño Southern Oscillation (ENSO), and Indian Ocean Dipole (IOD). Thus, it would appear that this particular event was caused by a rare combination of surface processes acting on seasonal timescales. Nevertheless, we cannot rule out the possibility that long-term climate change (natural or anthropogenic) also had an influence. Of note is the well-documented decadal trend towards positive SAM-like conditions in the Southern Ocean, which is linked to the recent strengthening and poleward shift of the circumpolar westerlies (Marshall, 2003). While the underlying cause of this trend is unclear, it is likely associated with the recent decline in Antarctic ozone and the global increase in greenhouses gases (Shindell and Schmidt, 2004; Thompson et al., 2011; Polvani et al., 2011). More importantly, model simulations suggest that such forcing should lead to an initial surface cooling followed by a slow long-term warming across the Southern Ocean (Ferreira et al., 2015; Seviour et al., 2019). Thus, it is possible that the 2016–2017 event was the start of a longer timescale transition to reduced sea ice cover and warmer SSTs in the Southern Ocean.

A natural follow-up to the climatological analysis of wintertime ice-ocean feedbacks presented in Chapters 2 and 3 would be a corresponding analysis of their interannual variability. Assuming our under-ice data array continues to grow at its current rate, we will soon be able to identify long-term trends in wintertime stratification and upper ocean heat content across the sea ice zone, and potentially link them to changes in Antarctic sea ice extent. It will be particularly interesting to compare the covariance of these variables across each ocean basin. Better understanding of ice-ocean feedbacks on longer timescales may also provide additional insight into factors that caused the abrupt SST and sea ice extent trend reversals discussed in Chapter 4. As discussed earlier, the reappearance of the Weddell Sea polynya was an important contributor to the sharp decline in Antarctic sea ice extent. Recent work has also linked the recurrence of these polynyas to variations in SAM (Campbell et al., 2019). Thus, future work should examine the potential links between ice-ocean feedbacks, SAM, and other modes of internal climate variability in more detail.

BIBLIOGRAPHY

Abernathey, R., J. Marshall, and D. Ferreira, 2011: The Dependence of Southern Ocean Meridional Overturning on Wind Stress. *J. Phys. Oceanogr.*, **41 (12)**, 2261–2278, doi: 10.1175/JPO-D-11-023.1.

Akitomo, K., 1999: Open-ocean deep convection due to thermobaricity: 1. Scaling argument. *J. Geophys. Res. Ocean.*, **104 (C3)**, 5225–5234, doi:10.1029/1998JC900058.

Argo, 2018: Argo float data and metadata from Global Data Assembly Centre (Argo GDAC) - Snapshot of Argo GDAC of March 8, 2018. SEANOE. SEANOE, doi: 10.17882/4218255429.

Argo, 2019: Argo float data and metadata from Global Data Assembly Centre (Argo GDAC) - Snapshot of Argo GDAC as of February 8, 2019. SEANOE, doi:10.17882/42182.

Armour, K. C., and C. M. Bitz, 2015: Observed and projected trends in Antarctic sea ice. *US Clivar Var.*, **13**, 12–19.

Armour, K. C., J. Marshall, J. R. Scott, A. Donohoe, and E. R. Newsom, 2016: Southern Ocean warming delayed by circumpolar upwelling and equatorward transport. *Nat. Geosci.*, **9 (7)**, 549–554, doi:10.1038/ngeo2731.

Ashok, K., Z. Guan, and T. Yamagata, 2001: Impact of the Indian Ocean dipole on the relationship between the Indian monsoon rainfall and ENSO. *Geophys. Res. Lett.*, **28 (23)**, 4499–4502, doi:10.1029/2001GL013294.

Biddle, L. C., K. J. Heywood, J. Kaiser, and A. Jenkins, 2017: Glacial meltwater identification in the Amundsen Sea. *J. Phys. Oceanogr.*, JPO–D–16–0221.1, doi:10.1175/JPO-D-16-0221.1.

Bintanja, R., G. J. van Oldenborgh, S. S. Drijfhout, B. Wouters, and C. A. Katsman, 2013: Important role for ocean warming and increased ice-shelf melt in Antarctic sea-ice expansion. *Nat. Geosci.*, **6 (5)**, 376–379, doi:10.1038/ngeo1767.

Bitz, C. M., and L. M. Polvani, 2012: Antarctic climate response to stratospheric ozone depletion in a fine resolution ocean climate model. *Geophys. Res. Lett.*, **39 (20)**, doi:10.1029/2012GL053393.

Boehme, L., P. Lovell, M. Biuw, F. Roquet, J. Nicholson, S. E. Thorpe, M. P. Meredith, and M. Fedak, 2009: Technical note: Animal-borne CTD-Satellite Relay Data Loggers for real-time oceanographic data collection. *Ocean Sci.*, **5 (4)**, 685–695, doi:10.5194/os-5-685-2009.

Bretherton, C. S., C. Smith, and J. M. Wallace, 1992: An Intercomparison of Methods for Finding Coupled Patterns in Climate Data. *J. Clim.*, **5 (6)**, 541–560, doi:10.1175/1520-0442(1992)005¡0541:AIOMFF¿2.0.CO;2.

Campbell, E. C., E. Wilson, G. W. K. Moore, S. Riser, C. E. Brayton, M. Mazloff, and L. D. Talley, 2019: Antarctic offshore polynyas linked to Southern Hemisphere climate anomalies. *Nature*, **in press**, doi:10.1038/s41586-019-1294-0.

Carranza, M. M., and S. T. Gille, 2015: Southern Ocean wind-driven entrainment enhances satellite chlorophyll-a through the summer. *J. Geophys. Res. Ocean.*, **120 (1)**, 304–323, doi:10.1002/2014JC010203.

Cavalieri, D. J., and C. L. Parkinson, 2008: Antarctic sea ice variability and trends, 19792006. *J. Geophys. Res.*, **113 (C7)**, C07 004, doi:10.1029/2007JC004564.

Cavalieri, D. J., C. L. Parkinson, and K. Y. Vinnikov, 2003: 30-Year satellite record reveals contrasting Arctic and Antarctic decadal sea ice variability. *Geophys. Res. Lett.*, **30 (18)**, doi:10.1029/2003GL018031.

Charrassin, J.-B., and Coauthors, 2008: Southern Ocean frontal structure and sea-ice formation rates revealed by elephant seals. *Proc. Natl. Acad. Sci.*, **105 (33)**, 11 634–11 639, doi:10.1073/pnas.0800790105.

Cheon, W. G., and A. L. Gordon, 2019: Open-ocean polynyas and deep convection in the Southern Ocean. *Sci. Rep.*, **9 (1)**, 6935, doi:10.1038/s41598-019-43466-2.

Cheon, W. G., S. K. Lee, A. L. Gordon, Y. Liu, C. B. Cho, and J. J. Park, 2015: Replicating the 1970s' Weddell Polynya using a coupled ocean-sea ice model with reanalysis surface flux fields. *Geophys. Res. Lett.*, **42 (13)**, 5411–5418, doi:10.1002/2015GL064364.

Ciasto, L. M., and M. H. England, 2011: Observed ENSO teleconnections to Southern Ocean SST anomalies diagnosed from a surface mixed layer heat budget. *Geophys. Res. Lett.*, doi:10.1029/2011GL046895.

Clem, K. R., and R. L. Fogt, 2013: Varying roles of ENSO and SAM on the Antarctic Peninsula climate in austral spring. *J. Geophys. Res. Atmos.*, **118 (20)**, 11,481–11,492, doi:10.1002/jgrd.50860.

Cleveland, W. S., and S. J. Devlin, 1988: Locally weighted regression: An approach to regression analysis by local fitting. *J. Am. Stat. Assoc.*, **83 (403)**, 596–610, doi:10.1080/01621459.1988.10478639.

Comiso, J. C., and A. L. Gordon, 1987: Recurring polynyas over the Cosmonaut Sea and the Maud Rise. *J. Geophys. Res. Ocean.*, **92 (C3)**, 2819–2833, doi:10.1029/JC092iC03p02819.

de Boyer Montégut, C., 2004: Mixed layer depth over the global ocean: An examination of profile data and a profile-based climatology. *J. Geophys. Res.*, **109 (C12)**, C12 003, doi:10.1029/2004JC002378.

de Lavergne, C., J. B. Palter, E. D. Galbraith, R. Bernardello, and I. Marinov, 2014: Cessation of deep convection in the open Southern Ocean under anthropogenic climate change. *Nat. Clim. Chang.*, **4 (4)**, 278–282, doi:10.1038/nclimate2132.

de Steur, L., D. M. Holland, R. D. Muench, and M. G. McPhee, 2007: The warm-water "Halo" around Maud Rise: Properties, dynamics and Impact. *Deep. Res. Part I Oceanogr. Res. Pap.*, **54 (6)**, 871–896, doi:10.1016/j.dsr.2007.03.009.

Dee, D. P., and Coauthors, 2011: The ERA-Interim reanalysis: Configuration and performance of the data assimilation system. *Q. J. R. Meteorol. Soc.*, **137 (656)**, 553–597, doi:10.1002/qj.828.

Dewey, S. R., J. H. Morison, and J. Zhang, 2017: An Edge-Referenced Surface Fresh Layer in the Beaufort Sea Seasonal Ice Zone. *J. Phys. Oceanogr.*, **47 (5)**, 1125–1144, doi:10.1175/JPO-D-16-0158.1.

Doddridge, E. W., J. Marshall, H. Song, J. Campin, M. Kelley, and L. Nazarenko, 2019: Eddy compensation dampens Southern Ocean sea surface temperature response to westerly wind trends. *Geophys. Res. Lett.*, 2019GL082758, doi:10.1029/2019GL082758.

Dong, S., S. T. Gille, and J. Sprintall, 2007: An assessment of the Southern Ocean mixed layer heat budget. *J. Clim.*, doi:10.1175/JCLI4259.1.

Dong, S., J. Sprintall, S. T. Gille, and L. Talley, 2008: Southern ocean mixed-layer depth from Argo float profiles. *J. Geophys. Res. Ocean.*, doi:10.1029/2006JC004051.

Drucker, R., S. Martin, and R. Kwok, 2011: Sea ice production and export from coastal polynyas in the Weddell and Ross Seas. *Geophys. Res. Lett.*, **38 (17)**, n/a–n/a, doi:10.1029/2011GL048668.

Eicken, H., H. Fischer, and P. Lemke, 1995: Effects of the snow cover on Antarctic sea ice and potential modulation of its response to climate change. *Ann. Glaciol.*, **21**, 369–376, doi:10.1017/S0260305500016086.

Elipot, S., and S. T. Gille, 2009: Ekman layers in the Southern Ocean: spectral models and observations, vertical viscosity and boundary layer depth. *Ocean Sci. Discuss.*, **6 (1)**, 277–341, doi:10.5194/osd-6-277-2009.

Fahrbach, E., G. Rohardt, M. Schröder, and V. Strass, 1994: Transport and structure of the weddell gyre. *Ann. Geophys.*, **12 (9)**, 840–855, doi:10.1007/s00585-994-0840-7.

Fan, T., C. Deser, and D. P. Schneider, 2014: Recent Antarctic sea ice trends in the context of Southern Ocean surface climate variations since 1950. *Geophys. Res. Lett.*, **41 (7)**, 2419–2426, doi:10.1002/2014GL059239.

Ferreira, D., J. Marshall, C. M. Bitz, S. Solomon, and A. Plumb, 2015: Antarctic Ocean and Sea Ice Response to Ozone Depletion: A Two-Time-Scale Problem. *J. Clim.*, **28 (3)**, 1206–1226, doi:10.1175/JCLI-D-14-00313.1.

Foster, T. D., and E. C. Carmack, 1976: Temperature and Salinity Structure in the Weddell Sea. *J. Phys. Oceanogr.*, **6 (1)**, 36–44, doi:10.1175/1520-0485(1976)006¡0036:TASSIT¿2.0.CO;2.

Francis, D., C. Eayrs, J. Cuesta, and D. Holland, 2019: Polar Cyclones at the Origin of the Reoccurrence of the Maud Rise Polynya in Austral Winter 2017. *J. Geophys. Res. Atmos.*, 2019JD030618, doi:10.1029/2019JD030618.

Friehe, C. A., K. F. Schmitt, C. A. Friehe, and K. F. Schmitt, 1976: Parameterization of Air-Sea Interface Fluxes of Sensible Heat and Moisture by the Bulk Aerodynamic Formulas. *J. Phys. Oceanogr.*, **6 (6)**, 801–809, doi:10.1175/1520-0485(1976)006¡0801:POASIF¿2.0.CO;2.

Gill, A. E., 1973: Circulation and bottom water production in the Weddell Sea. *Deep. Res. Oceanogr. Abstr.*, **20 (2)**, 111–140, doi:10.1016/0011-7471(73)90048-X.

Goosse, H., and V. Zunz, 2014: Decadal trends in the Antarctic sea ice extent ultimately controlled by ice-ocean feedback. *Cryosphere*, **8 (2)**, 453–470, doi:10.5194/tc-8-453-2014.

Goosse, H., and Coauthors, 2018: Quantifying climate feedbacks in polar regions. *Nat. Commun.*, **9 (1)**, 1919, doi:10.1038/s41467-018-04173-0.

Gordon, A. L., 1978: Deep Antarctic Convection West of Maud Rise. *J. Phys. Oceanogr.*, **8 (4)**, 600–612, doi:10.1175/1520-0485(1978)008¡0600:DACWOM¿2.0.CO;2.

Gordon, A. L., C. T. Chen, and W. G. Metcalf, 1984: Winter Mixed Layer Entrainment of Weddell Deep Water. *J. Geophys. Res.*, **89 (C1)**, 637–640, doi:10.1029/JC089iC01p00637.

Gordon, A. L., and B. A. Huber, 1984: Thermohaline Stratification Below the Southern Ocean Sea Ice. *J. Geophys. Res.*, **89 (C1)**, 641–648, doi:10.1029/JC089iC01p00641.

Gordon, A. L., and B. A. Huber, 1990: Southern Ocean winter mixed layer. *J. Geophys. Res.*, **95 (C7)**, 11 655, doi:10.1029/JC095iC07p11655.

Gordon, A. L., M. Visbeck, and J. C. Comiso, 2007: A possible link between the Weddell Polynya and the southern annular mode. *J. Clim.*, **20 (11)**, 2558–2571, doi: 10.1175/JCLI4046.1.

Hallberg, R., and A. Gnanadesikan, 2006: The Role of Eddies in Determining the Structure and Response of the Wind-Driven Southern Hemisphere Overturning: Results from the Modeling Eddies in the Southern Ocean (MESO) Project. *J. Phys. Oceanogr.*, **36 (12)**, 2232–2252, doi:10.1175/JPO2980.1.

Haumann, F. A., N. Gruber, M. Münnich, I. Frenger, and S. Kern, 2016: Sea-ice transport driving Southern Ocean salinity and its recent trends. *Nature*, **537 (7618)**, 89–92, doi: 10.1038/nature19101.

Hirabara, M., H. Tsujino, H. Nakano, and G. Yamanaka, 2012: Formation mechanism of the Weddell Sea Polynya and the impact on the global abyssal ocean. *J. Oceanogr.*, **68 (5)**, 771–796, doi:10.1007/s10872-012-0139-3.

Holland, D. M., 2000: Transient sea-ice polynya forced by oceanic flow variability. *Prog. Oceanogr.*, **48 (4)**, 403–460, doi:10.1016/S0079-6611(01)00010-6.

Holland, P. R., 2014: The seasonality of Antarctic sea ice trends. *Geophys. Res. Lett.*, **41 (12)**, 4230–4237, doi:10.1002/2014GL060172.

Holland, P. R., and R. Kwok, 2012: Wind-driven trends in Antarctic sea-ice drift. *Nat. Geosci.*, **5 (12)**, 872–875, doi:10.1038/ngeo1627.

Holte, J., and L. Talley, 2009: A New Algorithm for Finding Mixed Layer Depths with Applications to Argo Data and Subantarctic Mode Water Formation*. *J. Atmos. Ocean. Technol.*, **26 (9)**, 1920–1939, doi:10.1175/2009JTECHO543.1.

Hyatt, J., 2006: Wind, Sea Ice, Inertial Oscillations and Upper Ocean Mixing in Marguerite Bay, Western Antarctic Peninsula: Observations and Modeling. Ph.D. thesis, MIT/WHOI Joint Program, 168 pp., doi:10.1575/1912/1238.

Jacobs, S. S., R. G. Fairbanks, and Y. G. Horibe, 1985: Origin and evolution of water masses near the Antarctic continental margin: Evidence from H218O/H216O ratios in seawater. *Antarct. Res. Ser.*, S. S. Jacobs, Ed., American Geophysical Union, chap. Oceanology, 59–85, doi:10.1029/AR043p0059.

Jena, B., M. Ravichandran, and J. Turner, 2019: Recent reoccurrence of large open-ocean polynya on the Maud Rise seamount. *Geophys. Res. Lett.*, 2018GL081482, doi:10.1029/2018GL081482.

Jerlov, N. G., 1968: Optical oceanography. Elsevier Oceanography Series 5.

Johnson, G. C., 2008: Quantifying Antarctic Bottom Water and North Atlantic Deep Water volumes. *J. Geophys. Res.*, **113 (5)**, C05 027, doi:10.1029/2007JC004477.

Kimura, N., 2004: Sea Ice Motion in Response to Surface Wind and Ocean Current in the Southern Ocean. *J. Meteorol. Soc. Japan*, **82 (4)**, 1223–1231, doi:10.2151/jmsj.2004.1223.

Klatt, O., O. Boebel, and E. Fahrbach, 2007: A profiling float's sense of ice. *J. Atmos. Ocean. Technol.*, **24 (7)**, 1301–1308, doi:10.1175/JTECH2026.1.

Kurtakoti, P., M. Veneziani, A. Stössel, and W. Weijer, 2018: Preconditioning and Formation of Maud Rise Polynyas in a High-Resolution Earth System Model. *J. Clim.*, **31 (23)**, 9659–9678, doi:10.1175/JCLI-D-18-0392.1.

Kurtz, N. T., and T. Markus, 2012: Satellite observations of Antarctic sea ice thickness and volume. *J. Geophys. Res. Ocean.*, **117 (8)**, doi:10.1029/2012JC008141.

Lecomte, O., H. Goosse, T. Fichefet, C. De Lavergne, A. Barthélemy, and V. Zunz, 2017: Vertical ocean heat redistribution sustaining sea-ice concentration trends in the Ross Sea. *Nat. Commun.*, **8 (1)**, 258, doi:10.1038/s41467-017-00347-4.

Lemke, P., 1987: A coupled one-dimensional sea ice-ocean model. *J. Geophys. Res.*, **92 (C12)**, 13 164, doi:10.1029/JC092iC12p13164.

Lenn, Y.-D., and T. K. Chereskin, 2009: Observations of Ekman Currents in the Southern Ocean. *J. Phys. Oceanogr.*, **39 (3)**, 768–779, doi:10.1175/2008JPO3943.1.

L'Heureux, M. L., and D. W. J. Thompson, 2006: Observed Relationships between the El NiñoSouthern Oscillation and the Extratropical Zonal-Mean Circulation. *J. Clim.*, **19 (2)**, 276–287, doi:10.1175/JCLI3617.1.

Li, Z. X., 2000: Influence of tropical Pacific El Niño on the SST of the Southern Ocean Through Atmospheric Bridge. *Geophys. Res. Lett.*, **27 (21)**, 3505–3508, doi: 10.1029/1999GL011182.

Lindsay, R. W., D. M. Holland, and R. A. Woodgate, 2004: Halo of low ice concentration observed over the Maud Rise seamount. *Geophys. Res. Lett.*, **31 (13)**, n/a–n/a, doi: 10.1029/2004GL019831.

Liu, J., and J. A. Curry, 2010: Accelerated warming of the Southern Ocean and its impacts on the hydrological cycle and sea ice. *Proc. Natl. Acad. Sci.*, **107 (34)**, 14 987–14 992, doi:10.1073/pnas.1003336107.

Marshall, G. J., 2003: Trends in the Southern Annular Mode from Observations and Reanalyses. *J. Clim.*, **16 (24)**, 4134–4143, doi:10.1175/1520-0442(2003)016¡4134:TITSAM¿2.0.CO;2.

Marshall, J., and T. Radko, 2003: Residual-Mean Solutions for the Antarctic Circumpolar Current and Its Associated Overturning Circulation. *J. Phys. Oceanogr.*, **33 (11)**, 2341–2354, doi:10.1175/1520-0485(2003)033¡2341:RSFTAC¿2.0.CO;2.

Marshall, J., and K. Speer, 2012: Closure of the meridional overturning circulation through Southern Ocean upwelling. *Nat. Geosci.*, **5 (3)**, 171–180, doi:10.1038/ngeo1391.

Martinson, D. G., 1990: Evolution of the southern ocean winter mixed layer and sea ice: Open ocean deepwater formation and ventilation. *J. Geophys. Res.*, **95 (C7)**, 11 641, doi:10.1029/JC095iC07p11641.

Martinson, D. G., and R. A. Iannuzzi, 1998: Antarctic ocean-ice interaction: Implications from ocean bulk property distributions in the Weddell gyre. *Antarct. Sea Ice Phys. Process. Interact. Var.*, M.O. Jeffries, Ed., Vol. 74, American Geophysical Union, Washington, DC, 243–271, doi:10.1029/AR074p0243.

Martinson, D. G., and C. Wamser, 1990: Ice drift and momentum exchange in winter Antarctic pack ice. *J. Geophys. Res.*, **95 (C2)**, 1741, doi:10.1029/JC095iC02p01741.

McDougall, T. J., and P. Barker, 2011: Getting started with TEOS-10 and the Gibbs Seawater (GSW) Oceanographic Toolbox. *Scor/Iapso Wg127*, 28, doi:SCOR/IAPSO WG127.

McPhee, M. G., 1992: Turbulent heat flux in the upper ocean under sea ice. *J. Geophys. Res.*, **97 (C4)**, 5365, doi:10.1029/92JC00239.

McPhee, M. G., C. Kottmeier, and J. H. Morison, 1999: Ocean Heat Flux in the Central Weddell Sea during Winter. *J. Phys. Oceanogr.*, **29 (6)**, 1166–1179, doi:10.1175/1520-0485(1999)029¡1166:OHFITC¿2.0.CO;2.

McPhee, M. G., and D. G. Martinson, 1994: Turbulent mixing under drifting pack ice in the Weddell Sea. *Science (80-.).*, **263 (5144)**, 218–221, doi:10.1126/science.263.5144.218.

McPhee, M. G., and Coauthors, 1996: The Antarctic Zone Flux Experiment. *Bull. Am. Meteorol. Soc.*, **77 (6)**, 1221–1232, doi:10.1175/1520-0477(1996)077¡1221:TAZFE¿2.0.CO;2.

Meehl, G. A., J. M. Arblaster, C. M. Bitz, C. T. Y. Chung, and H. Teng, 2016: Antarctic sea-ice expansion between 2000 and 2014 driven by tropical Pacific decadal climate variability. *Nat. Geosci.*, **9 (8)**, 590–595, doi:10.1038/ngeo2751.

Meehl, G. A., J. M. Arblaster, C. T. Chung, M. M. Holland, A. DuVivier, L. A. Thompson, D. Yang, and C. M. Bitz, 2019: Sustained ocean changes contributed to sudden Antarctic sea ice retreat in late 2016. *Nat. Commun.*, doi:10.1038/s41467-018-07865-9.

Meier, W., F. Fetterer, M. Savoie, S. Mallory, R. Duerr, and J. Stroeve, 2017: NOAA/NSIDC Climate Data Record of Passive Microwave Sea Ice Concentration, Version 3. NSIDC: National Snow and Ice Data Center, Boulder, Colorado USA., doi:10.7265/N59P2ZTG.

Morrison, A. K., and A. M. Hogg, 2013: On the Relationship between Southern Ocean Overturning and ACC Transport. *J. Phys. Oceanogr.*, **43 (1)**, 140–148, doi:10.1175/JPO-D-12-057.1.

Muench, R. D., H. J. S. Fernando, and G. R. Stegen, 1990: Temperature and salinity staircases in the northwestern Weddell Sea. *J. Phys. Oceanogr.*, **20 (2)**, 295–306, doi:10.1175/1520-0485(1990)020¡0295:TASSIT¿2.0.CO;2.

Parkinson, C. L., and D. J. Cavalieri, 2008: Arctic sea ice variability and trends, 19792006. *J. Geophys. Res.*, **113 (C7)**, C07 003, doi:10.1029/2007JC004558.

Pauling, A. G., C. M. Bitz, I. J. Smith, and P. J. Langhorne, 2016: The Response of the Southern Ocean and Antarctic Sea Ice to Freshwater from Ice Shelves in an Earth System Model. *J. Clim.*, **29 (5)**, 1655–1672, doi:10.1175/JCLI-D-15-0501.1.

Pellichero, V., J. B. Sallée, S. Schmidtko, F. Roquet, and J. B. Charrassin, 2017: The ocean mixed layer under Southern Ocean sea-ice: Seasonal cycle and forcing. *J. Geophys. Res. Ocean.*, **122 (2)**, 1608–1633, doi:10.1002/2016JC011970.

Peng, G., W. N. Meier, D. J. Scott, and M. H. Savoie, 2013: A long-term and reproducible passive microwave sea ice concentration data record for climate studies and monitoring. *Earth Syst. Sci. Data*, **5 (2)**, 311–318, doi:10.5194/essd-5-311-2013.

Polvani, L. M., D. W. Waugh, G. J. P. Correa, and S.-W. Son, 2011: Stratospheric Ozone Depletion: The Main Driver of Twentieth-Century Atmospheric Circulation Changes in the Southern Hemisphere. *J. Clim.*, **24 (3)**, 795–812, doi:10.1175/2010JCLI3772.1.

Price, J. F., R. A. Weller, and R. Pinkel, 1986: Diurnal cycling: Observations and models of the upper ocean response to diurnal heating, cooling, and wind mixing. *J. Geophys. Res.*, **91 (C7)**, 8411, doi:10.1029/JC091iC07p08411.

Pritchard, H. D., S. R. Ligtenberg, H. A. Fricker, D. G. Vaughan, M. R. Van Den Broeke, and L. Padman, 2012: Antarctic ice-sheet loss driven by basal melting of ice shelves. *Nature*, **484 (7395)**, 502–505, doi:10.1038/nature10968.

Purich, A., M. H. England, W. Cai, A. Sullivan, and P. J. Durack, 2018: Impacts of Broad-Scale Surface Freshening of the Southern Ocean in a Coupled Climate Model. *J. Clim.*, **31 (7)**, 2613–2632, doi:10.1175/JCLI-D-17-0092.1.

Reeve, K. A., O. Boebel, T. Kanzow, V. Strass, G. Rohardt, and E. Fahrbach, 2015: Objective mapping of Argo data in the Weddell Gyre: a gridded dataset of upper ocean water properties. *Earth Syst. Sci. Data Discuss.*, **8 (1)**, 509–566, doi:10.5194/essdd-8-509-2015.

Reynolds, R. W., N. A. Rayner, T. M. Smith, D. C. Stokes, and W. Wang, 2002: An Improved In Situ and Satellite SST Analysis for Climate. *J. Clim.*, **15 (13)**, 1609–1625, doi:10.1175/1520-0442(2002)015¡1609:AIISAS¿2.0.CO;2.

Rintoul, S. R., C. W. Hughes, and D. Olbers, 2001: Chapter 4.6 The antarctic circumpolar current system. *Int. Geophys.*, **77 (C)**, doi:10.1016/S0074-6142(01)80124-8.

Riser, S. C., and Coauthors, 2016: Fifteen years of ocean observations with the global Argo array. *Nat. Clim. Chang.*, **6 (2)**, 145–153, doi:10.1038/nclimate2872.

Robertson, R., L. Padman, and M. D. Levine, 1995: Fine structure, microstructure, and vertical mixing processes in the upper ocean in the western Weddell Sea. *J. Geophys. Res.*, **100 (95)**, 18 517, doi:10.1029/95JC01742.

Roemmich, D., and J. Gilson, 2009: The 20042008 mean and annual cycle of temperature, salinity, and steric height in the global ocean from the Argo Program. *Prog. Oceanogr.*, **82 (2)**, 81–100, doi:10.1016/j.pocean.2009.03.004.

Roemmich, D., S. Riser, R. Davis, and Y. Desaubies, 2004: Autonomous Profiling Floats: Workhorse for Broad-scale Ocean Observations. *Mar. Technol. Soc. J.*, **38 (2)**, 21–29, doi:10.4031/002533204787522802.

Roquet, F., and Coauthors, 2013: Estimates of the Southern Ocean general circulation improved by animal-borne instruments. *Geophys. Res. Lett.*, **40 (23)**, 6176–6180, doi: 10.1002/2013GL058304.

Roquet, F., and Coauthors, 2014: A Southern Indian Ocean database of hydrographic profiles obtained with instrumented elephant seals. *Sci. Data*, **1**, 140 028, doi: 10.1038/sdata.2014.28.

Roquet, F., and Coauthors, 2017: MEOP-CTD in-situ data collection: a Southern ocean Marine-mammals calibrated sea water temperatures and salinities observations - 2017-11 release. SEANOE, doi:10.17882/45461.

Saji, N., and T. Yamagata, 2003: Possible impacts of Indian Ocean Dipole mode events on global climate. *Clim. Res.*, **25**, 151–169, doi:10.3354/cr025151.

Saji, N. H., B. N. Goswami, P. N. Vinayachandran, and T. Yamagata, 1999: A dipole mode in the tropical Indian Ocean. *Nature*, **401 (6751)**, 360–363, doi:10.1038/43854.

Sallée, J. B., K. G. Speer, and S. R. Rintoul, 2010: Zonally asymmetric response of the Southern Ocean mixed-layer depth to the Southern Annular Mode. *Nat. Geosci.*, **3 (4)**, 273–279, doi:10.1038/ngeo812.

Schlosser, E., F. Alexander Haumann, and M. N. Raphael, 2018: Atmospheric influences on the anomalous 2016 Antarctic sea ice decay. *Cryosphere*, doi:10.5194/tc-12-1103-2018.

Semtner, A. J., 1976: A Model for the Thermodynamic Growth of Sea Ice in Numerical Investigations of Climate. *J. Phys. Oceanogr.*, **6**, 379–389, doi:10.1175/1520-0485(1976)006¡0379:AMFTTG¿2.0.CO;2.

Seviour, W. J. M., and Coauthors, 2019: The Southern Ocean sea surface temperature response to ozone depletion: A multi-model comparison. *J. Clim.*, JCLI–D–19–0109.1, doi:10.1175/JCLI-D-19-0109.1.

Shindell, D. T., and G. A. Schmidt, 2004: Southern Hemisphere climate response to ozone changes and greenhouse gas increases. *Geophys. Res. Lett.*, **31 (18)**, L18 209, doi:10.1029/2004GL020724.

Shinoda, T., and W. Han, 2005: Influence of the Indian Ocean Dipole on Atmospheric Subseasonal Variability. *J. Clim.*, **18 (18)**, 3891–3909, doi:10.1175/JCLI3510.1.

Sigmond, M., and J. C. Fyfe, 2014: The Antarctic Sea Ice Response to the Ozone Hole in Climate Models. *J. Clim.*, **27 (3)**, 1336–1342, doi:10.1175/JCLI-D-13-00590.1.

Speer, K., S. R. Rintoul, and B. Sloyan, 2000: The Diabatic Deacon Cell*. *J. Phys. Oceanogr.*, **30 (12)**, 3212–3222, doi:10.1175/1520-0485(2000)030¡3212:TDDC¿2.0.CO;2.

Stammerjohn, S. E., D. G. Martinson, R. C. Smith, X. Yuan, and D. Rind, 2008: Trends in Antarctic annual sea ice retreat and advance and their relation to El NiñoSouthern

Oscillation and Southern Annular Mode variability. *J. Geophys. Res.*, **113 (C3)**, C03S90, doi:10.1029/2007JC004269.

Stroeve, J., M. M. Holland, W. Meier, T. Scambos, and M. Serreze, 2007: Arctic sea ice decline: Faster than forecast. *Geophys. Res. Lett.*, **34 (9)**, doi:10.1029/2007GL029703.

Stuecker, M. F., C. M. Bitz, and K. C. Armour, 2017: Conditions leading to the unprecedented low Antarctic sea ice extent during the 2016 austral spring season. *Geophys. Res. Lett.*, **44 (17)**, 9008–9019, doi:10.1002/2017GL074691.

Swart, N. C., and J. C. Fyfe, 2012: Observed and simulated changes in the Southern Hemisphere surface westerly wind-stress. *Geophys. Res. Lett.*, **39 (16)**, n/a–n/a, doi:10.1029/2012GL052810.

Swart, N. C., and J. C. Fyfe, 2013: The influence of recent Antarctic ice sheet retreat on simulated sea ice area trends. *Geophys. Res. Lett.*, **40 (16)**, 4328–4332, doi:10.1002/grl.50820.

Swart, S., and Coauthors, 2018: Return of the Maud Rise Polynya: climate litmus or sea ice anomaly? [in State of the Climate in 2017]. *Bull. Am. Meteorol. Soc.*, **99 (8)**, S188–S310, doi:10.1175/2018BAMSStateoftheClimate.1.

Thompson, D. W. J., S. Solomon, P. J. Kushner, M. H. England, K. M. Grise, and D. J. Karoly, 2011: Signatures of the Antarctic ozone hole in Southern Hemisphere surface climate change. *Nat. Geosci.*, **4 (11)**, 741–749, doi:10.1038/ngeo1296.

Toole, J. M., M. L. Timmermans, D. K. Perovich, R. A. Krishfield, A. Proshutinsky, and J. A. Richter-Menge, 2010: Influences of the ocean surface mixed layer and thermohaline stratification on Arctic Sea ice in the central Canada Basin. *J. Geophys. Res. Ocean.*, **115 (10)**, C10 018, doi:10.1029/2009JC005660.

Turner, J., T. J. Bracegirdle, T. Phillips, G. J. Marshall, and J. S. Hosking, 2013a: An Initial Assessment of Antarctic Sea Ice Extent in the CMIP5 Models. *J. Clim.*, **26 (5)**, 1473–1484, doi:10.1175/JCLI-D-12-00068.1.

Turner, J., T. Phillips, J. S. Hosking, G. J. Marshall, and A. Orr, 2013b: The Amundsen Sea low. *Int. J. Climatol.*, **33 (7)**, 1818–1829, doi:10.1002/joc.3558.

Turner, J., T. Phillips, G. J. Marshall, J. S. Hosking, J. O. Pope, T. J. Bracegirdle, and P. Deb, 2017: Unprecedented springtime retreat of Antarctic sea ice in 2016. *Geophys. Res. Lett.*, doi:10.1002/2017GL073656.

Wang, G., H. H. Hendon, J. M. Arblaster, E.-P. Lim, S. Abhik, and P. van Rensch, 2019: Compounding tropical and stratospheric forcing of the record low Antarctic sea-ice in 2016. *Nat. Commun.*, **10 (1)**, 13, doi:10.1038/s41467-018-07689-7.

Webster, P. J., A. M. Moore, J. P. Loschnigg, and R. R. Leben, 1999: Coupled oceanatmosphere dynamics in the Indian Ocean during 199798. *Nature*, **401 (6751)**, 356–360, doi:10.1038/43848.

Wilson, E. A., A. L. Gordon, and D. Kim, 2013: Observations of the Madden Julian Oscillation during Indian Ocean Dipole events. *J. Geophys. Res. Atmos.*, **118 (6)**, 2588–2599, doi:10.1002/jgrd.50241.

Wong, A. P. S., and S. C. Riser, 2011: Profiling Float Observations of the Upper Ocean under Sea Ice off the Wilkes Land Coast of Antarctica. *J. Phys. Oceanogr.*, **41 (6)**, 1102–1115, doi:10.1175/2011JPO4516.1.

Worby, A. P., C. A. Geiger, M. J. Paget, M. L. Van Woert, S. F. Ackley, and T. L. DeLiberty, 2008: Thickness distribution of Antarctic sea ice. *J. Geophys. Res. Ocean.*, **113 (5)**, C05S92, doi:10.1029/2007JC004254.

Yuan, X., and D. G. Martinson, 2000: Antarctic Sea Ice Extent Variability and Its Global Connectivity*. *J. Clim.*, **13 (10)**, 1697–1717, doi:10.1175/1520-0442(2000)013¡1697:ASIEVA¿2.0.CO;2.

Zhang, J., 2005: Warming of the arctic ice-ocean system is faster than the global average since the 1960s. *Geophys. Res. Lett.*, **32 (19)**, n/a–n/a, doi:10.1029/2005GL024216.

Zhang, J., 2007: Increasing Antarctic Sea Ice under Warming Atmospheric and Oceanic Conditions. *J. Clim.*, **20 (11)**, 2515–2529, doi:10.1175/JCLI4136.1.

Zhang, L., T. L. Delworth, W. Cooke, and X. Yang, 2019: Natural variability of Southern Ocean convection as a driver of observed climate trends. *Nat. Clim. Chang.*, **9 (1)**, 59–65, doi:10.1038/s41558-018-0350-3.

Zwally, H. J., 2002: Variability of Antarctic sea ice 19791998. *J. Geophys. Res.*, **107 (C5)**, 3041, doi:10.1029/2000JC000733.

VITA

Earle Wilson grew up in Montego Bay, Jamaica. Upon finishing high school in Jamaica, he started college at Morehouse College before transferring to Columbia University, where he earned a bachelor of science degree in Applied Physics. After a one year stint as a research assistant at the Lamont Doherty Earth Observatory, he moved to Seattle to attend graduate school at the University of Washington. When not thinking about research, Earle likes to cook, play ultimate Frisbee, and go on long walks in the forest.